The structure and kinematics of the Milky Way Galaxy and the formation of its massive stars as seen by maser VLBI

Ross Alexander Burns
Graduate School of Science & Engineering
Kagoshima University

A thesis submitted for the degree of
PhilosophiæDoctor (PhD)
March 2016

1. Reviewer: Handa Toshihiro

2. Reviewer: Hiroko Shinnaga

3. Reviewer: Nakanishi Hiroyuki

Day of the defence:

Signature from head of PhD committee:

Abstract

In this thesis I discuss two main topics; massive star formation, and the structure and kinematics of the Milky Way Galaxy. These topics are closely tied since massive stars are born and die in the great spiral arms which twist around our Galaxy. Measuring the distribution of massive stars therefore allows us to trace out the 3D shape of the Galaxy.

In addition to these science topics I aim to provide basic background on maser emission and the observing techniques and reduction of maser VLBI data. We will see that VLBI maser astrometry provides artisan scrutiny of star formation in real-time 3D, in addition to telling us about the shape and rotation of our Galaxy.

Acknowledgements

Over the past 4 years I have learned more about the world and its people than any other time in my life. This experience brought me to a life far richer in depth and dimensions, all of which had lain beyond the limits of my previous world. I have all the acquaintances and friendships - some brushing and some steadfast - to thank, some for moulding me and some for preserving me in my efforts. Travel and culture, along with history, have taught me of the ever-changing nature of the world. This property brought about the myriad ways of thinking and contrasting opinions; the ideas of proper conduct, even 'good and bad', are not universal constants, but vary from place to place and time to time. To live in acceptance and consideration of these things is to truly be 'international'. With this frame of mind every experience becomes a lesson, life is good, collaborations cross borders and research and creativity can flourish. In that state of mind even sad or bitter encounters tell us something about the state or the world and the work that needs doing. Being brought to that realisation is what I wish to acknowledge most (so my thanks are to, essentially, everyone).

Kagoshima is a subtropical peninsula at the southernmost tip of Kyushyu island of mainland Japan. The small city, edged by sea and backed by mountains, looks out at Sakurajima to the East - a volcano that erupted daily for much of my time here (its erupting right now, I can see if from the lab). The climate, warm and welcoming, is reflected in its people - who are known throughout Japan for their kindness and love of good food and drink. I thank the city of Kagoshima for providing me a place to live and work. Leaving here will break my heart.

With regards to astronomy research I can thank my PhD supervisor Professor Handa Toshihiro for giving me free reigns in my choice of topics, while also providing his considerable sway and influence in the astronomical community whenever we needed to propose/request anything - this more than made up for my lack of experience and status. In addition, I owe much to everyone at the department of science at Kagoshima university who helped me not just in research related things but also any assistance that I needed in my life in Kagoshima - from finding a house to ordering my PhD graduation gown.

Im also grateful for the financial stability provided by the ministry of education, culture, sports, science and technology (MEXT) Japan as part of the Monbukagakusho scholarship. Having MEXT taking care of things meant that in addition to money, administrative paper work involved in immigration, enrolment and basic living were never an issue distracting me from progress.

This thesis does not change the world - I can hardly say it even benefits anyone - but doing a PhD was an incredibly stimulating and enjoyable experience which has sculpted my worldview and will certainly contribute to any good that I go on to do in my life.

Contents

List of Figures

LIST OF FIGURES

List of Tables

LIST OF TABLES

1

Introduction

1.1 Structures made of stars

We are all familiar with the beautiful images of spiral and barred spiral galaxies captured by optical telescopes such as the Hubble Space Telescope. Such galaxies show beautiful long spiral arm structures made entirely of stars, gas and dust, and one may even infer some sense of rotation from the whirlpool appearance of these giant stellar systems.

Spiral arms stand out brightly, with very little light in the inter-arm regions of the disk, perhaps leading one to the interpretation that stars only exist in the spiral arms. However, this is not the case. Infact, the whole disk is populated roughly evenly with stars - what makes the spiral arms so distinct is that they contain massive stars, which are many times brighter than ordinary stars. As such, the massive stars dominate the optical light output of a galaxy, illuminating the spiral structure.

Massive stars are born in the spiral arms and burn up quickly, dying young and never migrating into the inter-arm regions. This leads to the sharp, defined appearance of the spiral arms and highlights the practicality of using massive stars for tracing the structure and motion of a galaxy.

1.2 The Milky Way Galaxy

From an outside perspective the Milky Way Galaxy would also appear as a disk with a bright spiral structure. However from our perspective; an embedded, edge-on viewpoint looking thought the plane of the disk, the entire content of the Galaxy appears as a narrow band of stars and dust lanes - stretched 360 degrees across the sky.

In order to get some idea of the morphology of the Milky Way Galaxy; its size and the shape of its spiral arms, we make use of the massive stars as arm tracers. By measuring their distance in all directions we can draw a heliocentric map of the Galaxy, as though we are feeling our way around the Galaxy. Infact, rather than using the actual massive stars themselves, radio astronomers map the Galactic distribution of massive star forming regions (MSFRs) which are bright radio emitters. This is advantageous for the task at hand since radio emission is not diminished by the gas and dust in the Galactic disk, which prevents optical astronomers from seeing much further than the Solar neighbourhood. In this effort, radio astronomers make use of masers (Section 2) which are bright in radio emission and are often found at sites of massive star formation.

1.3 A dynamic Galaxy

Galaxies are dynamic systems, rotating and constantly evolving as material in the disk flows in and out of the spiral arms. Astronomers devised the 'Galactic constants' which are a set of parameters that quantify the size and rotation nature of the Milky Way Galaxy (Oort, 1927; Kerr & Lynden-Bell, 1986). The most fundamental of the Galactic constants are the Galactocentric distance to the Sun, R_0, the Galactic circular rotation velocity evaluated at the position of the Sun, Θ_0, and finally the angular velocity of Galactic rotation of the local standard of rest, Ω_0 which is evaluated as $\Omega_0 = \Theta_0/R_0$. These parameters define the rotation curve of the Galaxy (it's rotation velocity as a function of Galactocentric radius) which reveals the total distribution of mass (both baryonic and dark) in the Milky Way Galaxy.

The International Astronomical Union issues recommended values for the Galactic constants, currently fixed at $R_0 = 8.5$ kpc, and $\Theta_0 = 220$ km s, leading to $\Omega_0 = 25.9$ km s^{-1} kpc^{-1}, based on a compilation of independently measured values summarised in Kerr & Lynden-Bell (1986). However, more recent observations point to the need to revise the Galactic constants (Reid et al., 2014; Burns et al., 2014b).

1.4 Massive star formation

The very fact that massive stars trace the spiral arms is interesting in itself, raising questions about whether the conditions required for forming massive stars are different to those for low mass stars. Indeed, the formation mechanisms of massive stars continue to elude astronomers who debate amongst various competing theories.

The main issues encountered by theorists hoping to understand the formation of massive stars are those of radiation pressure and angular momentum. The former, radiation pressure, should limit accretion to a maximum final stellar mass of $8M_\odot$ (Palla & Stahler, 1993), while the latter, angular momentum, must be removed from the rotating central region in order for accretion to take place at all. Treatment of these issues must be conceived theoretically and tested observationally in order to approach a deeper understanding of massive star formation. However, relative to their low mass counterparts, massive young stellar objects (MYSOs) - which are the progenitors of high-mass main-sequence stars - are far fewer in number, more distant, and more deeply embedded in denser molecular environments, making them significantly harder to study observationally.

1.5 The power of maser VLBI

Very long baseline interferometry (VLBI) is a technique which combines a group of distantly separated radio antenna to create a 'synthesised' telescope with very fine angular resolution. Such arrays are sensitive to bright point-like emission such as masers, and can peer into the central regions of MYSOs which are invisible to optical telescopes.

Masers arise in special conditions and require a source of excitation - as such they are often found near the sites of forming stars; in outflows, jets, bow shocks and expanding shells (Bartkiewicz & van Langevelde, 2012). Observing the astrometry of masers in

multiple epochs with VLBI enables detailed 3D analysis of the internal motions in regions of star formation. Knowledge of the size and motions of structures involved in star formation reveals how stars form, which, as eluded to previously, is of particular interest.

Maser VLBI observations provide highly accurate astrometric sky-plane positions. If such observations are repeated over the duration of a year it is possible to observe the motion of the maser source (the motion of the star forming region) as it travels through the Galaxy. Included in this motion is a sinusoidal osscilation arising from annual parallax; the perceived oscillation of object caused by the Earth's orbit about the Sun. Using trigonometry, annual parallax gives the distance to the maser source, and its systemic astrometry gives its space motion. Since star formation traces the Galactic spiral arms, maser VLBI also therefore enables study of the structure and kinematics of the Galaxy, allowing estimation of the Galactic constants.

1.6 The issues addressed in this thesis

In this thesis I demonstrate the use of multi-epoch maser VLBI observations to study both the structure and kinematics of the Galaxy, and the formation mechanisms of massive stars. The thesis will run as follows:

- All science discussed within the above topics was made possible by using maser VLBI. As such I begin with basic explanation of maser emission (Section 2).
- I outline the fundamentals of maser VLBI observation, data reduction and fitting of astrometric results to obtain the source annual parallax and proper motion (Section 3).
- Using the results of recent observations I track the internal 3D motions of masers to investigate the formation of massive stars with special attention to issues relating to accretion and angular momentum removal from the central region (Section 4).
- Finally, I discuss the annual parallax and 3D space motions of Galactic star forming regions (SFRs) and use them to estimate the Galactic constants (Section 5).

2

Masers

All science discussed within the topics of massive star formation and the Galactic constants was made possible by using masers. Therefore I will explain what is a maser; what conditions and environments produce maser emission. Aditionally I will discuss how masers amplify exponentially with respect to the path length of the emitting gas this gives rise to maser burst events. I will discuss maser burst theory and evidence from my observations of a maser burst in S235AB-MIR.

2.1 Maser emission

A maser is a cloud of gas which has special properties that make it emit very bright radiation in a very narrow frequency range. Masers are found in various astronomical environments including comets, planetary atmospheres, the proximities of very young stars and the proximities of very old stars. Masers are so bright that they have been seen even in external galaxies (Mega-masers) though most well studied maser sources are in our own Galaxy.

What makes a maser so bright is its state of population inversion, which, in short, simply means that the masing molecule has a higher population in one of its higher energy, E_2, excitation levels in comparison with one of its lower ones, E_1. If an incoming photon has an energy corresponding to $E_2 - E_1$ then it will cause stimulated emission resulting in the production of another photon, coherent to the first (Figure 2.1. These two photons go on to stimulate emission of another two photons - thus we see that the original incident photon is amplified exponentially as it travels through the medium, i.e. gain relates exponentially to the path length of the medium.

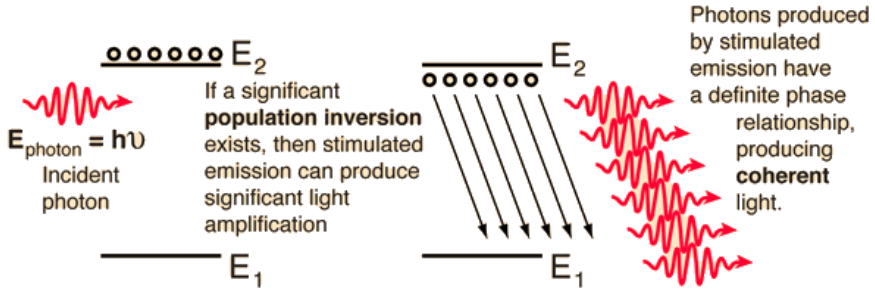

Figure 2.1: Emission process in a maser http://hyperphysics.phy-astr.gsu.edu/hbase/imgmod/qpro3.gif

For a maser to achieve population inversion it must have some mechanism of exciting molecules up to level E_2 quicker than they leave it via spontaneous emission. This is called 'pumping'. The only molecular transitions that exhibit masers are those which can be pumped to achieve population inversion. The most commonly used astronomical masers are H_2O, CH_3CO, OH and SiO which have maser transitions at radio frequencies.

Pumping essentially requires force-feeding a molecule with energy at the right frequency, this can be done collisionally *or* radiatively - for example 22 GHz H_2O masers and *class I* CH_3OH masers are pumped collisionally whereas *class II* CH_3OH masers are pumped radiatively, meaning that collisionally excited masers are often found in regions of shocked gas, such as the bow shocks of jets and outflows, whereas the radiatively excited masers are found near to their host stars, where radiation is stong. Consequently, the presence of different maser species tells us something about the physical conditions at the source.

Pumping rate, both collisional and radiative, relies on the energy available in the environment and the number of molecules able to be pumped (the gas density). If the rate of stimulated emission becomes fast enough it can drain the upper population such that it is no longer inverted. This limits the amplification of the maser and the maser is said to be 'saturated'.

2.1.1 Identifying masers (as opposed to thermal emission)

Maser emission is non-thermal, therefore maser emission can be recognised by its deviation from the observed behaviour of thermal emission. When a molecule is in thermal equilibrium the population of each of its quantum-mechanically allowed energy levels follows a Boltzman distribution which follows the equation

$$N_i = g_i / e^{E_i/kT} \tag{2.1}$$

where N_i is the number of molecules in the i state, g_i is the statistical weight of the transition and E_i is its energy level. The distribution is illustrated in Figure 2.2.

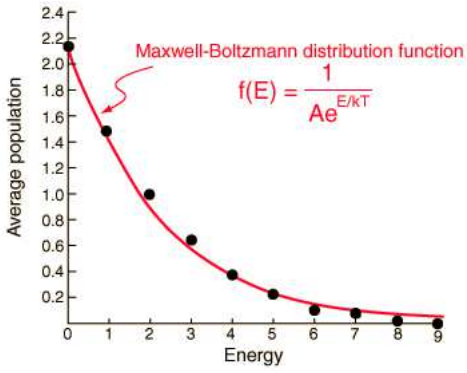

Figure 2.2: The Boltzmann distribution of energy states in a thermal gas http://hyperphysics.phy-astr.gsu.edu/hbase/quantum/imgqua/bolex.gif

Astronomers observing molecular gas often evaluate its 'column density' which is the number of emitting molecules seen in the observing beam of the telescope. As such this quantity directly relates to molecular population states - which as we see from Equation 2.1 depends on the temperature of the gas. This means that, for gas in thermal equilibrium, an astronomer who has measured the column density of several transitions of a molecule can estimate its temperature. Obtaining a temperature this way makes use of the "rotation diagram" method, also known as the "population diagram" which is well outlined in Goldsmith & Langer (1999). By observing several transitions of a molecular species in this way it is possible to identify maser emission by its deviation from the trend exhibited by thermally emitting transitions. An example of such a case is shown in Figure 2.3.

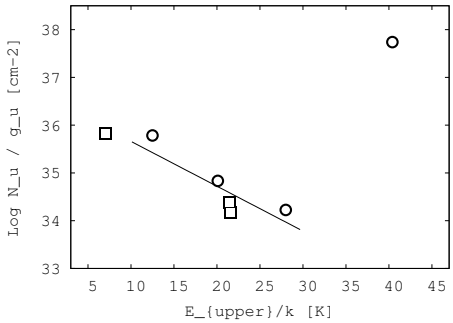

Figure 2.3: Population diagram of CH_3OH in S235AB. E- and A-species are indicated by circles and squares respectively. Thermal emission fits to a line of slope T_{rot}^{-1}. Maser (non-thermal) emission deviating from the line is seen at $E_{upper} = 39$ K

To turn this argument around, assuming we can make a rough approximation for the temperature of the gas - in such a case we can estimate the expected population of a particular thermal transition based on its quantum mechanical properties (such as statistical weights and Einstein coefficients). Emission from a particular transition can be recognised as a maser when its population number density exceeds that which would be expected for a thermal gas.

Since masers are produced in small, dense condensations of gas we can expect them to have only small turbulent motions within the coherent masing region of the cloud, leading to narrow line widths of only 1 to 2 km s^{-1} for each maser feature. This is also a product of exponential gain amplifying the peak of the would-be Gaussian, where velocity coherence persists for a longer path length.

2.2 Time variation and the 'Maser burst'

As we have mentioned the amplitude of emission is very sensitive to the path length of the masing material. Also we mentioned that masers are found in energetic and dense regions. Short timescale turbulence in these environments can cause short timescale changes in the path length of the masing material - which gives the brightness of maser

emission a time variation which has been seen to change on timescales of days (or even shorter).

A sudden increase in maser brightness is known as a 'burst'. Deguchi & Watson (1989) proposed a maser burst model in which an increase in path length, achieved by the overlapping of two masing clouds along the line of sight, can produce an increase of two or more orders of magnitude in observed brightness. Multi-epoch VLBI observations by Shimoikura et al. (2005) found observational evidence of this process in the case of the water masers of Orion KL, however there are few other examples of a maser burst caught 'in the act'. There were 2 strong maser bursts during our VLBI monitoring observations of S235AB-MIR in which fluxes of ∼100 Jy were reached, as shown in Figure 4.10.

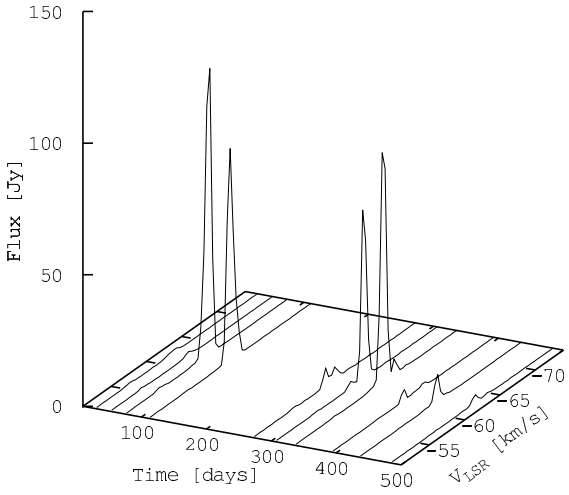

Figure 2.4: Scalar averaged spectra of the blue lobe H_2O emission at full scale, highlighting the variable burst nature.

Two peaks can be seen in epoch 5 (MJD 56564) at −64.68 km s^{-1} and −62.58 km s^{-1} which respectively correspond to the blue and green components seen in Figure 4.11, where feature B is at map offset (0,0). In epoch 6 (34 days later) the total flux of feature B raised from 7 Jy to 80 Jy as the two components overlapped both in space and velocity. Therefore we observe that the bursting mechanism in the masers of S235AB-MIR (Felli et al., 2007) is the same as that which was seen in Shimoikura et al. (2005). Figure 4.11 illustrates the 'pre-burst' stage of this mechanism.

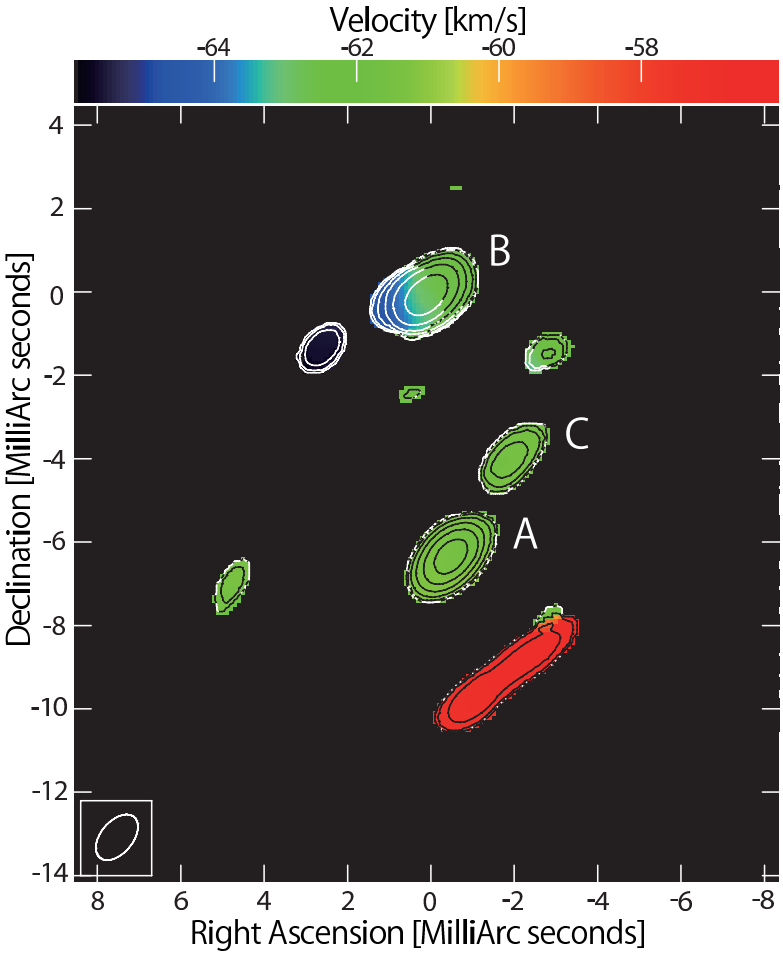

Figure 2.5: An example of astronomical maser emission. This map was produced from maser emission seen in S235AB-MIR (*see* Section 4.2). Here colours represent line of sight velocity and contours indicate amplitude at 3, 5, 10, 20, 40, 80 times the image rms noise of 200 mJy.

3

VLBI

3.1 Fundamentals of VLBI

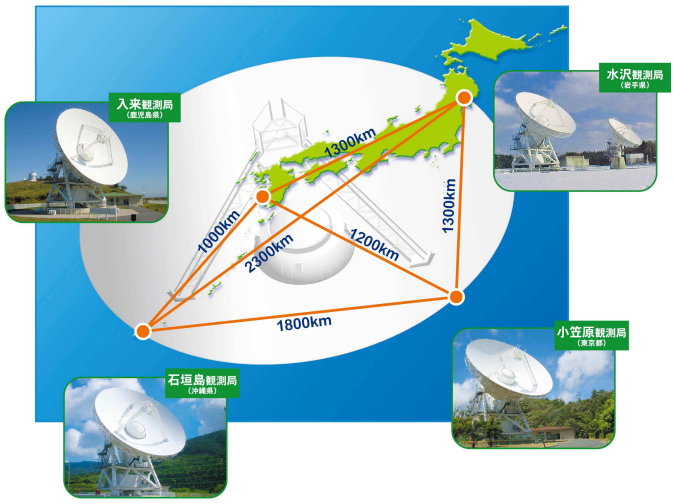

Figure 3.1: The VERA VLBI array from www.sinet.ad.jp/case/kagoshima/vera_arry.jpg

Radio telescopes are very different from conventional optical telescopes; radio telescopes do not make images using multi-pixel cameras, such as the CCD cameras of optical astronomy. Infact, one radio antenna effectively has just one 'pixel' - it simply measures the amplitude of a signal which enters the telescope beam from space. Yet, we often see beautiful high resolution images which are produced by radio telescopes - how is this possible using only single pixel antennae? The answer is to use interferometry; a technique of combining a group of individual radio antennae to create a 'synthesised' telescope with an angular resolution (beamsize) equivalent to that of a single dish telescope of the size of the whole array as illustrated in Figure 3.1. In the case of very long baseline interferometrty (VLBI), where the individual antennae are distantly separated, the resulting beam is very fine - perhaps only a few milliarcseconds (mas) in angular

size. In this chapter I aim to explain how interferometry works using visualisations that hopefully make the process more intuitive and easy to understand.

3.1.1 Signals: measurement and correlation

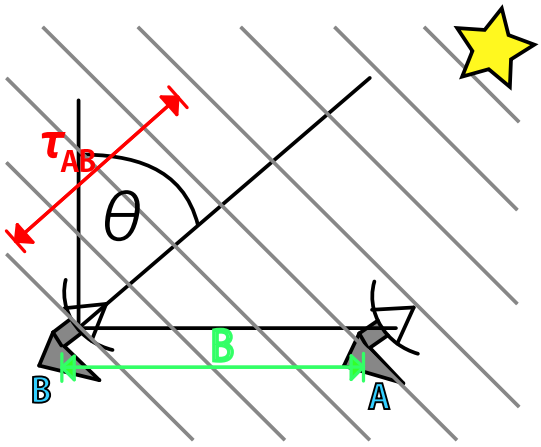

Figure 3.2: Delay in signal arrival times

Interferometry is often discussed in terms of 'delay' and 'phase'. These are interchangeable quantities but some concepts are more easily discussed in terms of phase and some other concepts in terms of delay. I will begin with delay since this is more intuitive and better suited for an introduction to VLBI.

Are you sitting comfortably? then lets begin.

The first thing to understand is the concept of arrival times; a signal from space arrives at different antennas on Earth at different times (*see* Figure 3.2). The difference in arrival times is called 'delay' and is usually written with the greek letter 'tau', τ. In Figure 3.2 the signal first reaches antenna A and then after some delay it reaches antenna B. We will denote the delay between antennas A and B as τ_{AB}.

When a signal enters the radio telescope - its voltage, v_t, is measured and recorded. The signal looks like noise; positive and negative voltage fluctuations changing rapidly with time. Since the signal comes from some celestial radio source the signal measured at antenna A, v_{tA}, should look the same as the signal measured by antenna B, v_{tB}, but with some time shift caused by the delay τ_{AB}.

In order to measure the delay, τ_{AB}, the recorded signals from antennas A and B are taken to a correlator. Here, the signals are compared to eachother and shifted in time by introducing small time lags. At each time lag the correlator will multiply the signals together. If the signals are out of time with eachother the result of multiplying two signals will also just look like noise. However, when the signals match eachother the multiplication of v_{tA} with v_{tA} will return only positive signals (positive x positive = positive, and, negative x negative = positive), indicating that correlation was achieved. By shifting v_{tB} until we achieve correlation with v_{tA} we can find the value of τ_{AB}. This principle is shown in Figure 3.3. Note that what we are essentially doing here is

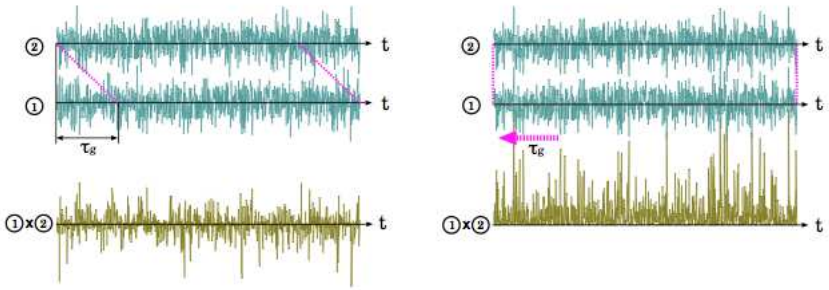

Figure 3.3: Measuring delay at the correlator
http://www.astro.sci.yamaguchi-u.ac.jp/jvn/reduction/kvnlecnote/kchap3.pdf

interfering two signals with eachother and measuring the output response - this is where the term 'interferometrty' comes from.

To introduce the concept of 'phase' we just imagine that our signal is sinusoidal instead of noise. Now, a difference in the arrival time will cause the waves to arrive at different points in their phase as is shown in Figure 3.4 - we call this difference a 'phase shift', and denote it as $\Delta\phi$. As mentioned previously, phase and delay are interchangeable - they are different representations of the same thing. They relate to eachother by the relation: $\Delta\phi = 2\pi\nu\tau$, such that the delay of the signal arrival time between antennas A and B, τ_{AB}, would cause a difference in phase of

$$\Delta\phi_{\mathrm{AB}} = 2\pi\nu\tau_{\mathrm{AB}} \tag{3.1}$$

As an example, if we observe a typical VERA water maser at frequency of 22 GHz, a delay of 1×10^{-10} seconds would cause a phase shift of X degrees, corresponding to the same phase shift as is shown in Figure 3.4.

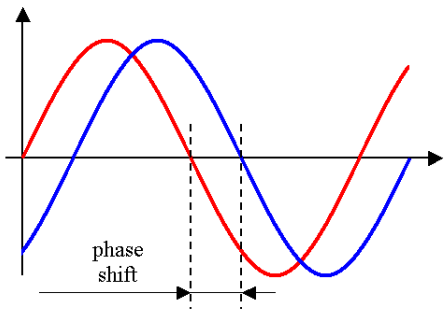

Figure 3.4: Phase shift

The delay is incredibly small, meaning that if we want to match the signal times during correlation we must record the data using very precise clocks. However, in reality, the delays are finer than the accuracy of the correlator (usually [Xs]) furthermore, the

delay changes over time - caused by weather and Earth rotation etc. - meaning that the value of τ_{AB} itself will also fluctuate on short timescales. Thus the delay determined by the correlator must be measured every second or so - this is called the 'parameter period'. Fine tuning delay calibration is done post-correlation during data reduction. We return to this topic later.

Below (Figure 3.5) is a simple schematic diagram showing signal recording and correlation pictured using our noise-like signal (useful in explaining delay) and sinusoidal signal (useful in explaining phase).

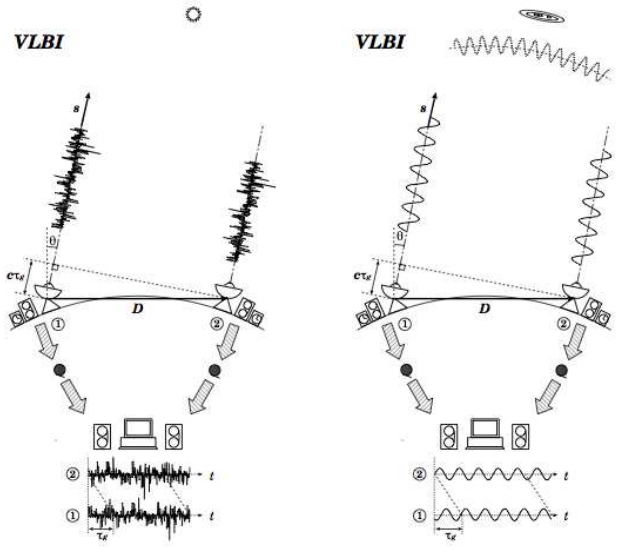

Figure 3.5: Signal recording and correlation
http://www.astro.sci.yamaguchi-u.ac.jp/jvn/reduction/kvnlecnote/kchap3.pdf

3.1.2 Visibilities and fringe patterns

Another commonly used term in VLBI refers to 'visibilities'. Radio signals have amplitude, A, and as we discussed previously, they have phase, ϕ, too. A 'visibility' is a quantity, used by radio astronomers, that has information about both amplitude and phase as can be seen in their mathematical expression: $\Psi = A\ cos(\phi)$. Remember that the signals v_A and v_B are multiplied during correlation, thus the correlated visibilities are a multiplication of eachother and therefore become

$$\Psi_A \Psi_B = A^2 \left(\frac{1}{2}\ cos(\phi) \right) \tag{3.2}$$

For now, the most important detail to notice is that the resulting interference pattern is a cosine function. We call this the 'fringe pattern', where the angular separation between fringes is called the 'fringe spacing' and is defined by $\theta = sin^{-1}(\lambda/B) \approx (\lambda/B)$ where λ is the observing wavelength and B is the projected baseline length)*see* Figure 3.6).

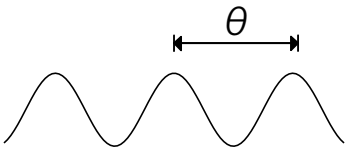

Figure 3.6: After correlation: fringe spacing

3.1.3 An example using two antennae

Now, let's imagine that we have a two antenna VLBI array, and that we make a very short observation of a point source directly above the array. Also, let's imagine that the fringe pattern is projected onto the sky as a 2D surface above the array as shown below (Figure 3.7).

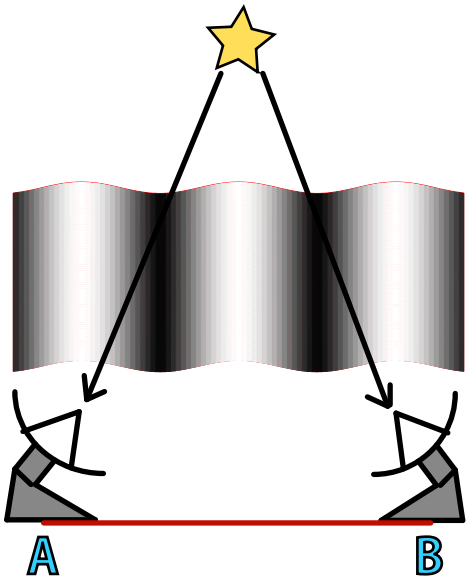

Figure 3.7: Fringe pattern of a point source observed on a single baseline

The signal should arrive at antenna A and antenna B simultaneously, therefore the delay, τ_{AB}, is zero. From Equation 3.1 we see that this means the phase difference is also zero. Then, from Equation 3.2 we see that $cos(\phi) = cos(0) = 1$, therefore the interferrometer has a maximum response at this position on the sky; the position of the point source, directly above the array.

If we were to observe a real source using the setup above our interferometric image would just look like the fringe pattern (Figure 3.8). We can see that the point source exists somewhere in the central vertical line i.e. we can resolve the position of the star in the horizontal direction, but the star could exist anywhere within the vertical stripe i.e. we know nothing about the position of the star in the vertical direction. This is

important - that one baseline can only resolve emission in one direction on the sky - and that our angular resolution depends on the fringe spacing (which depends on the baseline length).

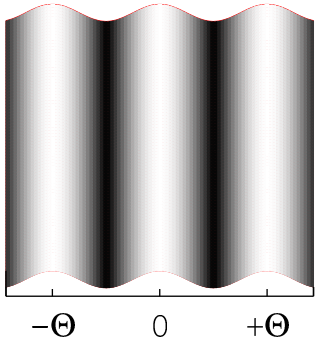

Figure 3.8: The fringe pattern: peaks separated by a fringe spacing

What we are essentially doing is convolving the source emission with the fringe pattern. This means taking the Fourier transform of the sky emission and the interference pattern, multiplying these together and then doing an inverse Fourier transform of the result to get the image. As a visualisation, it is useful to imagine that the fringe pattern acts like a filter which is multiplied with the sky emission. I will demonstrate this with some more examples.

Now lets consider that we wait 3 hours and observe the source again (for simplicity lets say the point source is at celestial North). The Earth will have revolved by 45° meaning that our antenna setup will have rotated by 45° too (Figure 3.9). If we wait another 3 hours and combine our three images then we get something like Figure 3.10

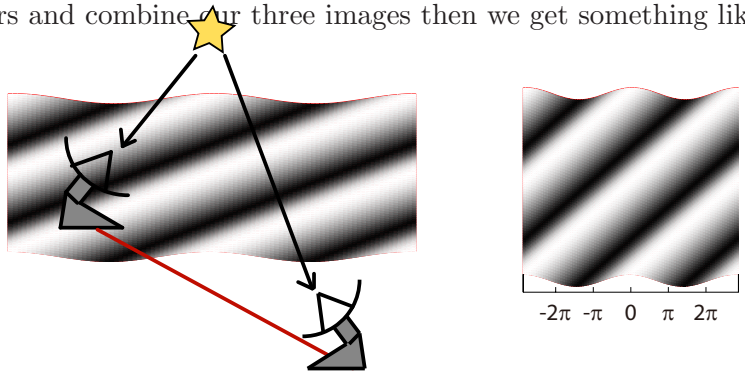

Figure 3.9: The fringe pattern changes after Earth rotation of 3 hrs

We see that at the center of all maps has a positive response, therefore integrating the two maps preserves a positive response here (central white peak). There are some regions in the combined map (grey regions) that have one positive and one negative response, thus cancelling eachother out, and other regions have two negative responses (dark pits) thus preserving a negative responses.

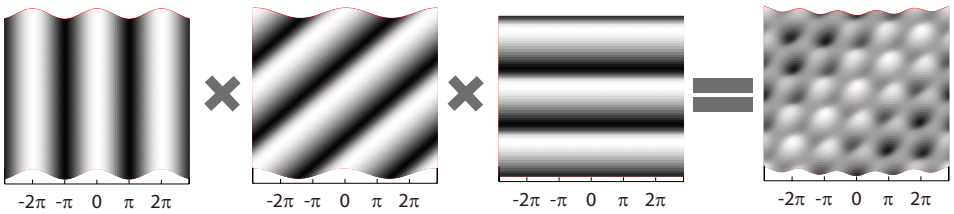

Figure 3.10: Combining scans from $t = 0$, $t = 3$ hr and $t = 6$ hr.

Now we have our first intuitive idea as to how VLBI images are formed - by multiplying together several fringe patterns as we have done here. In this simple visualisation we already know that the point source is at the center of the map, where the fringe patterns add up positively. However, note that several regions of positive response also appear around the central peak. These are 'side-lobes', and they can be suppressed by combining fringe patterns from various baselines of different length and orientations, as we will see.

3.1.4 Combining baselines

Lets now consider the effect of baseline length and combining baselines. Lets consider a three baseline scenario, our original baseline from earlier examples, plus one longer baseline and one shorter baseline - their lengths are B, $1.25 \times B$ and $0.77 \times B$, respectively. Remember that $\theta \approx (\lambda/B)$, thus increasing the baseline length will shorten the fringe spacing. As a result the longer baseline has a fringe spacing of $\phi/1.25 = 0.8 \times \theta$ and the shorter baseline has a fringe spacing of $\theta/0.77 = 1.3 \times \theta$. The fringe pattern of the VLBI array is the multiplication of the fringe patterns from the individual baselines i.e it would become the function $f_\phi \propto cos(\phi) \times cos(0.8\phi) \times cos(1.3\phi)$ which is illustrated in Figure 3.11.

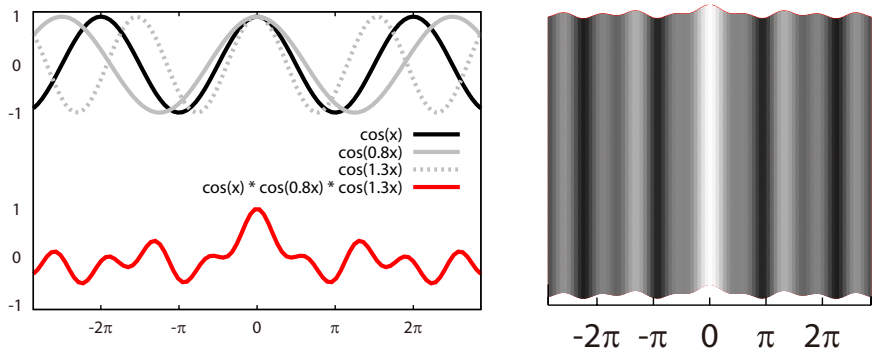

Figure 3.11: Combining baselines

As before, lets observe a point source with this 3-baseline scenario and combine it with a similar images taken 3 hours and 6 hours later (Figure 3.12). Compared to before the sidelobes are far more suppressed thanks to combining fringe patterns from short

and long baselines, and by integrating the three observations at different times - and the point source is more resolved thanks to the shorter fringe spacings contributed by the longer baseline.

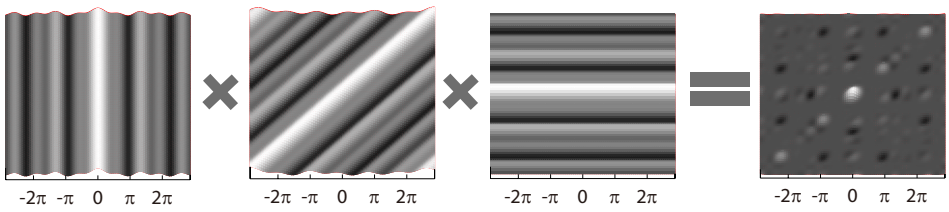

Figure 3.12: Forming a dirty beam

The two important topics to take home are that combining long and short baselines contribute narrow and wide fringe spacings to the combined fringe patter. This helps to suppress sidelobes. And that another way to suppress side lobes is to observe over long durations of time so that the positive and negative regions of the fringe pattern cancel/smooth eachother out. This can also be achieved by including baselines at various angles to eachother.

Rather than combining three fringe patterns at a intervals of 0, +3 and +6 hours, as we have done in our example, in real VLBI observations it is common for users to observe for $\sim$ 8 hours, continuously integrating the whole time. The resulting fringe pattern is then called the 'dirty beam' and it is with this pattern that the sky emission is convolved to form an image - known as a 'dirty map'. The best angular resolution image achieved by the VLBI array depends on the angular width of the central peak in the fringe pattern (the central peak in the dirty beam) - which depends on the longest baseline via the equation we already encountered: $\theta \approx \lambda/B$. This defines the size of the 'synthesized beam'. And example of a typical VERA dirty beam is shown in Figure 3.13.

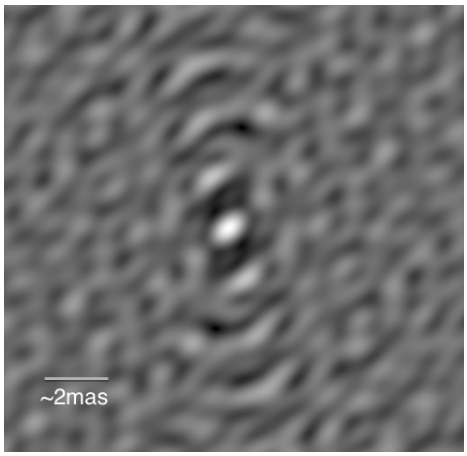

Figure 3.13: Example VERA dirty beam

3.1.5 The phase tracking center and offset point sources

Returning to our two-antenna example, we imagined imaging a source which was directly above the center of the baseline, such that the signal reached both antennae at the same time - therefore the delay was zero. In the case that the source is not directly above the array we may wish to point the array toward the offset source. The position of the map center is known as the 'phase tracking center', and we can 'steer' the position of the phase tracking center by artificially introducing some delay into one of the antennae.

Looking at Figure 3.14, we can see that the artificial delay required to be introduced to antenna B in order to steer the phase tracking center by some sky angle θ is given by: $\Delta\tau = Bsin\theta \ / \ c$. Where B is the absolute baseline length and c is the speed of light. The process of introducing this delay to steer the VLBI array is called 'delay tracking', and it ensures that the source remains stationary as it tracks across the sky over the course of the observations.

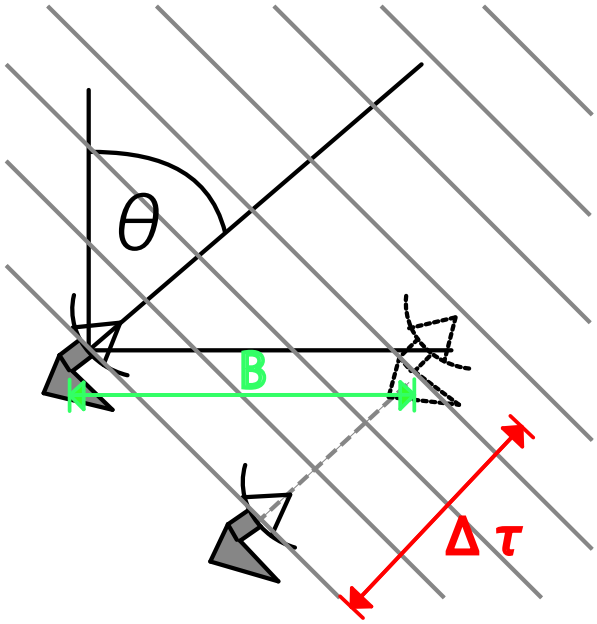

Figure 3.14: Delay tracking

The inverse situation is encountered when we observe a source which is offset from the phase tracking center. The angular offset will be measured as a delay of $\Delta\tau = Bsin\theta \ / \ c$ in the signals arriving at antennas A and B. Lets consider the case of a point source which is offset only in the East direction from the phase tracking center - being observed once by a 2-antenna array and then again 6 hours later - and that we combine the two images as we did before. The situation is illustrated in Figure 3.15.

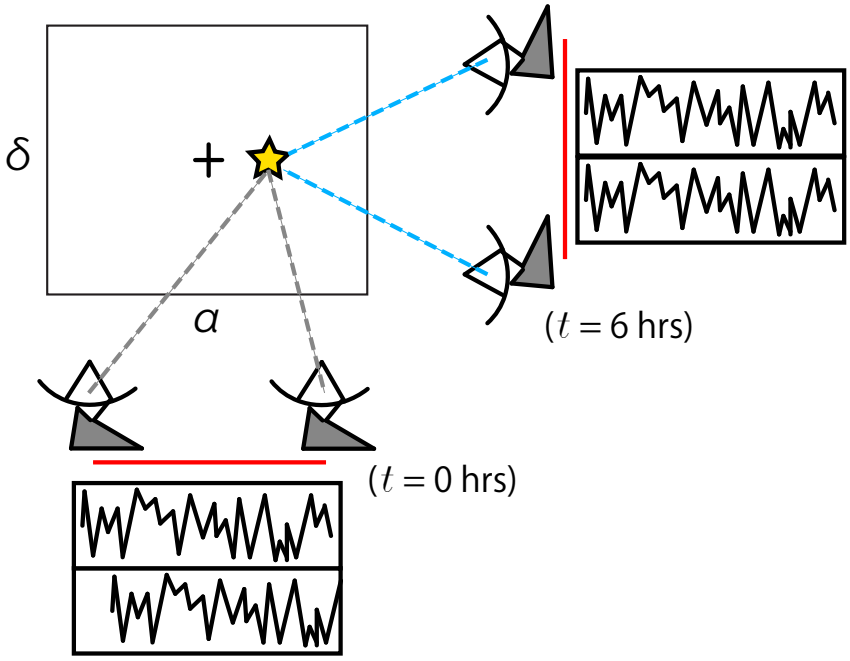

Figure 3.15: Imaging offset points and the corresponding delay

This situation helps to illustrate the directive resolution of VLBI arrays. At the second observing session (t = 6 hrs) the baseline is orientated North-South, meaning that its fringe pattern only resolves emission in the North-South direction. Looking at the (blue) antenna signals we see that the delay is zero, this is because there is no angular offset from the phase tracking center *in the direction aligned to the North-South baseline*. However, in the first observation (t = 0 hrs) we see that there is a delay in the signals reaching antennas. This delay is calculated much in the same way as delay tracking, using $\Delta\tau = Bsin\theta \ / \ c$. This is how it is possible for a VLBI array to image the 2D distribution of emission on the sky.

3.1.6 Resolving out extended sources

Until now we have only considered VLBI example scenarios using observations of point sources i.e. objects smaller and therefore unresolved by the synthesised beam. This is fine for the case of masers, which are typically unresolved, however there are also sources of extended emission such as quasars with jets.

It is useful to imagine that an extended source as an ensemble of 2D-Gaussian peaks. An example scenario is given in Figure 3.16 where the extended sky emission is decomposed into three Gaussians, at positions $x = 0$ (the center) and slight offsets from the central position ($x = \pm 0.5\times$ synthesized beam). Convolving the fringe pattern with each of these sources will produce three independent fringe patterns which are then combined with eachother. As we see, the peaks and troughs of the three fringe patterns interfere destructively, reducing the response of the correlated signal. Note also from Equation 3.1

that the corrolation output scales with the square of amplitude, thus a reduction such as this quickly leads to extended emission being lost from a VLBI image. Thus the extended emission is said to be 'resolved out'.

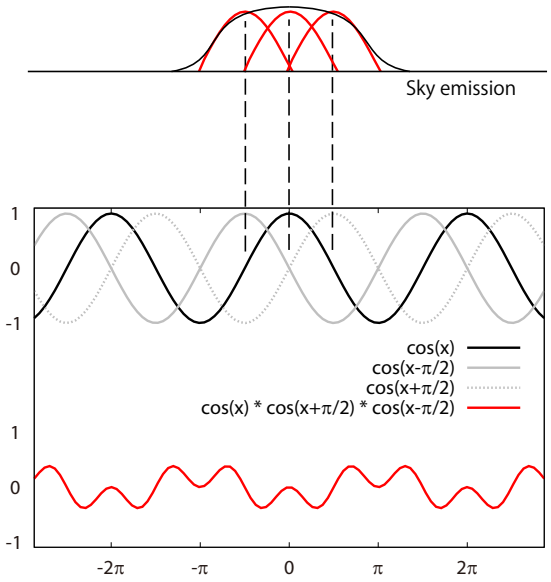

Figure 3.16: Destructive interference when imaging extended sources

To avoid resolving out emission it is best to include short baselines, since these contribute wide fringe spacing to the fringe pattern. Using our analogy to a filter, the wider spacings are better at representing emission through the fringe pattern (we do not need to break the source up into Gaussian components) this preserves a high response at signal correlation.

It is also interesting to note that one can understand something of the structure of a object by its measured intensity at different baselines reveal information about at which angular scale the source becomes resolved out because the amplitude will begin to decrease as it is resolved out on longer baselines. This can be useful when chosing suitable VLBI calibrators.

3.1.7 The CLEAN map

As mentioned previously, what the interferometer essentially 'sees' is a map which is the convolution of the dirty beam (combined fringe pattern of the array) and the true sky emission (which, as we discussed above, resolves out large scale structures). This map is called the 'dirty map'. What we hope to obtain is the true sky emission therefore we must deconvolve the dirty map with the dirty beam, this leaves only the sky emission which is created during data reduction.

The process of deconvolution is called the CLEAN algorithm which was introduced in Högbom (1974). It works on the assumption that any map can be decomposed into an ensemble of Gaussians. The astronomer first choses the brightest emission peak in

the map and borders it with a 'CLEAN box'. An emission pattern shaped like the dirty beam is subtracted from the map and its map position and amplitude is stored as a 'CLEAN component'. This subtraction is done in small iterations, and with each subtraction of a dirty beam the associated sidelobes are also subtracted, meaning that the noise in the original map is gradually reduced. After iterating a few subtractions of clean components the astronomer may then see secondary emission peaks emerging from the noise. CLEAN boxes are also set around these secondary peaks and more CLEAN components are taken until there are no more peaks left in the map. Finally, the CLEAN components are added together into what is called the CLEAN map (CLEAN components convolved with an 'ideal' Gaussian beam). Also, the final residual noise (which is usually quite small) is added to give an idea of map quality and a signal to noise ratio for CLEAN components.

3.2 phase referencing

Up to now, our example scenarios have only dealt with the signal delays caused by geometry; the angle to the source, the length and orientation of the baseline(s). This simplification is very useful for understanding the fundamental concepts of VLBI, however in reality there are other sources of delay which we have not yet considered. These sources of delay are significant, and without addressing them at data reduction we cannot make high-quality VLBI images. The biggest delay contributors are atmospheric delays and hardware related delays. Some sources of delay change rapidly with time while others remain almost constant. Therefore we must be careful when separating and calibrating delays from different causes.

As was done previously we will change our concept of dealing with signal delays to the concept of phase. Let's consider some maser emission in a single channel being detected during a long VLBI observation. During some short time interval at the beginning of the observation the signal has a phase of $+90°$ and its spectrum shows a brightness peak, as shown in the left part of Figure 3.17. At some later time, as shown in the right part of the figure, there is some cloud above one of the antennas, causing a a delay in signal arrival times, which leads to a phase shift. The maser is still detected at this time interval but the phase has become $-90°$. Now if we integrate our exposure time over these two time intervals the phases will interfere destructively and we will lose the maser emission entirely.

This exact situation can and does arise in VLBI. In our example case we simply said that the second observing interval was 'later' - however if it were only a few seconds later perhaps the issue would not be so bad. In this line of thinking astronomers define the 'coherence time' which is the interval of time over which it is safe to integrate the exposure time. Essentially it is the amount of time over which the atmosphere is considered stable, and in practical cases is about 1 to 3 minutes in maser VLBI at 22 GHz. However, in the previous section we discussed how VLBI observations need long exposure times of about ~ 8 hours. Therefore we see that we must calibrate all phase shifts (atmospheric and hardware related) with a time resolution of something like the coherence time; a time resolution of a few minutes. If we can successfully calibrate all phase shifts then integrating the signals over time will preserve the emission amplitude,

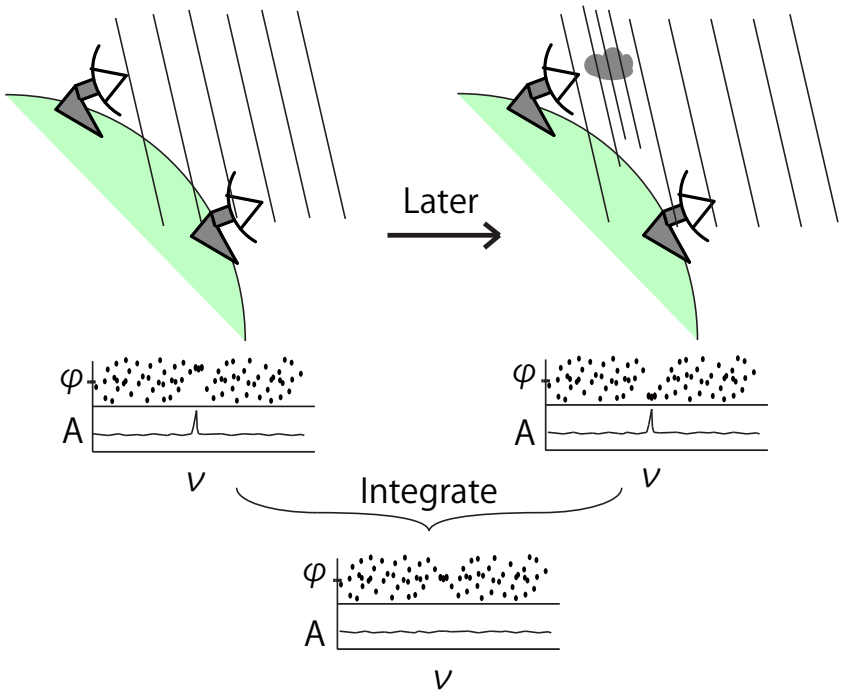

Figure 3.17: Destructive phase

while reducing the random noise. In VLBI maser astrometry the task of measuring and calibrating phase shifts can be achieved using 'phase referencing'.

To set up the explanation of phase referencing lets consider one baseline with two antennas A and B. The phase shift in the arriving signals, $\phi_{\rm AB}$ can be decomposed into the following:

$$\phi_{\rm AB} = \phi_{\rm dir} + \phi_{\rm bl} + \phi_{\rm ion} + \phi_{\rm trop} + \phi_{\rm inst} + \phi_{\rm str} + \epsilon_{\rm therm} \tag{3.3}$$

Here we have separated the geometric phase term into those which depend on the source direction on the sky, $\phi_{\rm dir}$, and phase errors arising from uncertainties in the baseline vector (antenna positions), $\phi_{\rm bl}$. Furthermore, $\phi_{\rm ion}$ is the phase contributed by the ionosphere and $\phi_{\rm trop}$ - the troposphere. $\phi_{\rm inst}$ is the instrumental phase coming from differences of hardware at each station (for example cable lengths etc.). $\phi_{\rm str}$ is a phase term coming from the structure of the source(s) on the sky as we discussed previously with regards to extended sources. $\epsilon_{\rm therm}$ is the contribution from thermal noise. For simplicity we only deal with one frequency channel here.

VLBI data is most often reduced using the Astronomical Image Processing System (AIPS) developed by the National Radio Astronomy Observatory (NRAO). One particular task, essential for VLBI data reduction, is called FRING. This task measures

the phase of post-correlated signals for each baseline, thus it can measure $\phi_{\rm AB}$ at time intervals set by the data reducer. By measuring $\phi_{\rm AB}$ and calibrating it at intervals of a few minutes we can avoid the problem of short coherence time by correcting for the effects of atmosphere and hardware.

However, note that if we measure and calibrate $\phi_{\rm AB}$ then we can no longer separate it into its individual contributions. In maser astrometry, the most important information is the position of the masers, however this information - which is contained in the $\phi_{\rm dir}$ is solved when running FRING. Practically, this means that the brightest maser will be moved to a directional offset of zero, i.e. the map's phase tracking center.

Phase referencing is a technique of solving for $\phi_{\rm AB}$ using a simple and stationary celestial object which is angularly near to the maser - usually a quasar - which is termed the phase reference source. The works on the grounds that the atmosphere along the line of sight to the quasar is the same for the maser. Thus most phase contributions measured for the quasar, $\phi^q_{\rm AB}$, should be the same as those for the maser, $\phi^m_{\rm AB}$. Thus, by determining $\phi^q_{\rm AB}$ using FRING and using the results to calibrate $\phi^m_{\rm AB}$ we can cancel many common terms;

$$\begin{aligned} \phi^m_{\rm AB} - \phi^q_{\rm AB} &= (\phi^m_{\rm dir} - \phi^q_{\rm dir}) \\ &+ (\phi^m_{\rm bl} - \phi^q_{\rm bl}) + (\phi^m_{\rm ion} - \phi^q_{\rm ion}) + (\phi^m_{\rm trop} - \phi^q_{\rm trop}) + (\phi^m_{\rm inst} - \phi^q_{\rm inst}) \\ &+ (\phi^m_{\rm str} - \phi^q_{\rm str}) - \epsilon^m_{\rm therm} - \epsilon^q_{\rm therm} \end{aligned} \tag{3.4}$$

Assuming point sources ($\phi_{\rm str} = 0$), and aside from thermal noise, the only terms that are not the same are $\phi_{\rm dir}$, therefore if we subtract the phase solutions measured for the quasar, $\phi^q_{\rm AB}$, from the uncalibrated phase data of the maser, $\phi^m_{\rm AB}$, we can distill the angular separation of the two objects, which (given that we know the position of the quasar, and that it does not move) gives the relative astrometric position of the maser. This is the backbone principle used in relative VLBI astrometry.

For VLBI arrays such as the VLBA and EVN (Very Long Baseline Array, and, European VLBI Network) phase referencing is achieved by alternating scans of the target maser and the reference quasar. Then the above subtraction is achieved by first interpolating the phase solutions measured during quasar scans to match in time with scans on the maser. This must be performed in a time less than the coherence time. On the other hand, VERA has the benefit of being a dual-beam VLBI array (Kawaguchi et al., 2000). Using the dual beams, observing the maser and reference source simultaneously removes the need to slew antennas and interpolate phase measurements between sources, enabling excellent determination of quick changing phase contributions.

3.2.1 Inverse phase referencing

The inverse phase referencing (IPR) technique for VERA was first introduced by Imai et al. (2012). Those authors provide a discussion of the advantages of IPR and the challenges of its implementation in dual-beam VLBI. They also provide a link to a webpage hosting working scripts that can run IPR (and conventional phase referencing) written in ParselTongue. We introduce here an approach to IPR VLBI data reduction using AIPS POPS.

In the IPR approach to reducing VLBI data the phase and rate solutions obtained using the maser emission are used to calibrate the continuum source data. This practice is commonplace for (single beam) VLBI arrays using fast switching and a standardised frequency setup, however it is more complicated using VERA in VERA7 and VERA7MM modes which allocate only a small bandwidth to the maser emission and a much wider bandwidth to the continuum source.

VERA dual-beam observations allow simultaneous observations of maser emission and a continuum source in separate telescope beams, henceforth referred to as the *'A-beam'* and *'B-beam'*, respectively.

With regards to phase calibration the first step is to apply source specific delay-tracking solutions which are based on tropospheric models calibrated using GPS measurements of the zenith path delay at each station (Honma et al., 2008a). Then we normalise phase gradients in the B-beam baselines by solving for the group delay using a bright continuum source. These solutions are also applied to the maser data since the wide bandwidth of the B-beam provides better determination of phase slope than the narrow bandwidth of the A-beam. Instrumental phase contributions from the dual-beam system were measured using an artificial noise source and subsequently removed.

At this stage all a-priori, station position, instrumental and group delay solutions have been applied. What remains are mostly atmospheric phase residuals which, at 22 GHz, are dominated by the dynamic troposphere (*see* Asaki et al. 2007).

Phase and rate solutions from the maser emission were then obtained with the task FRING in the A-beam at intervals of 1-2 minutes. Solutions were applied to the B-beam data - thus phase-referencing the continuum source. Finally - the continuum source was imaged, producing a map in which the co-ordinates have an origin at the phase tracking center of the B-beam in RA and Dec - with the continuum source offset somewhat from the map origin.

Since the precise co-ordinates of the continuum source are well-known its actual offset from the phase tracking center should be negligibly small. The measurable offset comes from the solutions carried over from the A-beam; the separation of the maser with respect to the phase tracking center in the A-beam. The offset of the continuum source therefore gives the absolute co-ordinates of the maser. Fringe-rate solutions from the maser were also applied to the A-beam, thereby self-calibrating it, which produced high quality maser maps and revealed many of the weak maser spots used in this work.

The flowchart in Figure A1 outlines the reduction method in terms of the main AIPS tasks however a step-by-step reduction guide, in the format of a POPS log file, is hosted at the following webpage:

`http://milkyway.sci.kagoshima-u.ac.jp/~rossburns88/Scripts.html`

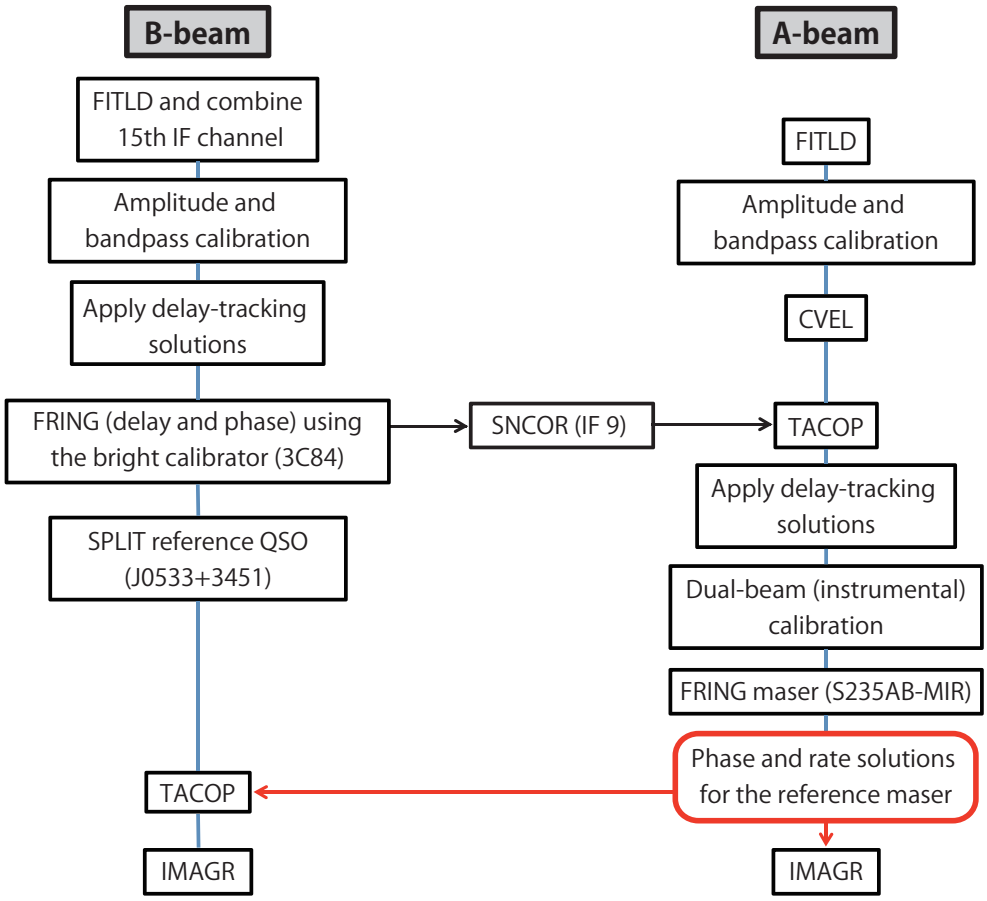

Figure 3.18: Flowchart of the inverse phase-referencing procedure for VERA data.

4

Formation of Massive Stars

Now that we have covered the emission processes and relevant techniques involved in maser VLBI we can proceed to discuss their use for the purposes of scientific research. The first topic which we investigate through maser VLBI concerns the formation of massive stars.

I will discuss the current status and standing issues with the theories of massive star formation. In this section I will give a deep discussion into how material accretes onto the central object in the face of radiation pressure and residual angular momentum. I will discuss the episodic nature of accretion and ejection, which is another characteristic expected from theories. Here I will discuss my results from a massive star forming region known as S255IR-SMA1 (Burns et al., 2016b), which shows evidence of episodic ejection. Furthermore, theories conclude that accretion requires removal of angular momentum from the disk which feeds the star here I will discuss my results on the massive star forming region known as S235AB-MIR which appears to have a rotating jet which may be capable of angular momentum transport (Burns et al., 2015).

4.1 Accretion: Overcoming radiation pressure

4.1.1 Introduction

The rarity, deeply embedded nature and large distances to massive young stellar objects (MYSOs) makes them difficult to observe and as a result their formation process, and especially the distinction from low-mass star formation, has yet to achieve consensus among astronomers. As the number of observational studies increases we begin to find MYSOs which exhibit many of the features commonly associated with low-mass star formation, such as circumstellar disks (Beltrán et al., 2004; Hirota et al., 2014), collimated outflows (Beuther et al., 2002; Davis et al., 2004) and even jet rotation (Burns et al., 2015). Distilling the distinction between low and high mass star formation is therefore of high priority in the search for a theory of massive star formation.

Corcoran & Ray (1998) show that, in low-mass YSOs, the L_{IR} excess, a tracer of accretion activity, scales linearly with outflow luminosity - a relationship indicative of the typical disk-jet-outflow process ubiquitous to low-mass star formation. This relationship was found to extend unbroken from $L_{bol} = 10^{-1} - 10^{5}$ $L_{\odot}$ (Caratti o Garatti et al., 2015), suggesting that stars in this luminosity range may be formed by a common process; that low mass star formation mechanisms can be 'scaled up' to a few tens of solar masses.

4. FORMATION OF MASSIVE STARS

In the case of low-mass stars, outflows are thought to be driven by a disk-launched collimated magnetocentifugal jet. In this scenario linear momentum from the jet seeps into the ambient gas environment, entraining it. The momentum transfer is more efficient nearer to the jet, and consequently the outflow velocity drops at larger radii from the outflow axis - producing a large-scale, low-velocity molecular outflow (Cabrit et al., 1997).

Whether or not the outflows from MYSOs are also driven by a magnetically collimated jets is yet to be firmly established. The often cited lower degree of collimation (Wu et al., 2004) in outflows from massive stars may indicate a different origin, such as a radiation driven outflow brought about by the flashlight effect in wind-blown cavities (Zinnecker & Yorke, 2007). Uncovering the driving mechanism of outflows in MYSOs is therefore a point of comparison between high-mass and low-mass star formation and therefore represents a clue as to whether or not massive star formation, at least to a few tens of solar masses, can be seen as a scaled-up version of the disk-jet-outflow process of low mass star formation. This forms the first topic of our study.

In addition to the issue of outflow mechanisms, perhaps a more fundamental issue encountered when attempting to explain the formation of massive stars concerns how accretion mechanisms can continue to operate when stellar radiation pressure becomes intense enough to halt infall - a condition which is thought to limit conventional star formation to stellar masses to about $8M_{\odot}$ (Palla & Stahler, 1993). This issue, amongst others, has lead to the belief that massive star formation cannot be an up-scaled version of low-mass star formation (Zinnecker & Yorke, 2007). In light of this, Hosokawa et al. (2015) show that if the stellar feedback from a massive star can be suppressed by bloating it with bursts of intense accretion, it seems possible to circumvent this limit and build stars up to hundreds of solar masses.

Thus, in this work, we compare the mechanisms of high-mass and low-mass star formation with regards to outflow driving mechanisms and episodic accretion bursts, using S255IR-SMA1 as a case study.

S255IR-SMA1 is the brightest source of molecular line emission in the S255IR star forming region (*see* Zinchenko et al. 2015), which is sandwiched between two evolved HII regions, S255 and S257. It is also a source of continuum emission in both millimeter (Wang et al., 2011; Zinchenko et al., 2015) and centimeter (Rengarajan & Ho, 1996), idicating the presence of a dusty core and ionizing emission from a luminous embedded star. Zinchenko et al. (2015) estimate the mass of the embedded star to be M $\simeq$ 20 $M_{\odot}$ based on its spectral energy distribution.

S255IR-SMA1 is an ideal target for this study because it has a circumstellar disk (a feature associated with low-mass star formation) and a massive molecular outflow. It also exhibits episodic ejection, hinting at episodic accretion. Moreover, previous very long baseline interferometry (VLBI) maser observations made with the very long baseline array (VLBA) revealed the presence of clusters of 22 GHz H_2O masers, at close proximity ($<$ 100 AU) to the MYSO, which aligned geometrically with the massive molecular outflow (Goddi et al., 2007) - suggesting the possible presence of a jet. Thus, this MYSO exhibits all of the ingredients required for our investigation.

Our approach is to re-visit the water masers in S255IR-SMA1 with further VLBI observation to look for evidence of a collimated maser jet which might help reveal the

driving nature of the massive outflows in this MYSO. We also seek the physical scales involved in ejection to infer the accretion history of S255IR-SMA1.

4.1.2 Observations and Data Reduction

All observations were carried out using VLBI Exploration of Radio Astrometry (VERA). Observations of S255IR-SMA1, and the continuum reference source J0613+1708, were made simultaneously by utilising the dual-beam capabilities of VERA (Kawaguchi et al., 2000). This removes the need to slew antennae and interpolate atmospheric phase solutions between sources - as is required for *fast-switching* VLBI phase referencing. As such, dual-beam observations achieve excellent suppression of the dynamic troposphere phase contribution, which is known to be the dominant source of astrometric phase error at 22 GHz (Asaki et al., 2007).

Left-handed circular polarisation signals were recorded to magnetic tapes at each VERA station, sampled at 2-bit quantisation, and filtered with the VERA digital filter unit (Iguchi et al., 2005). Signal correlation was carried out using the Mitaka FX correlator (Chikada et al., 1991). The total bandwidth of 256 MHz was divided into 16 intermediate frequency (IF) channels, with 15 IFs being allocated to continuum sources and 1 IF allocated to the maser emission. The maser IF, assuming a rest frequency of 22.235080 GHz, was correlated in 'zoom band' mode giving 8 MHz bandwidth and a channel spacing of 15.63 kHz, corresponding to a velocity resolution of 0.21 km s^{-1}. Fourteen of the 15 IFs allocated to continuum sources had bandwidths of 16 MHz and a resolution of 125 kHz channel spacing. The 15th IF allocated to continuum sources was correlated at the same bandwidth and resolution as the maser zoom band. In order to make uniformity in the continuum source IFs the 16 MHz bandwidth IFs were halved and combined with the zoomed 8 MHz bandwidth IF, allowing all 15 IFs to be merged.

Individual source phase tracking centers were set to $(\alpha, \delta)_{\rm J2000.0} = (06^{\rm h}12^{\rm m}54^{\rm s}.00640929$, $+17°59'22".95890)$ and $(\alpha, \delta)_{\rm J2000.0} = (06^{\rm h}13^{\rm m}36^{\rm s}.360073$, $+17°08'24".94542)$ for S255IR-SMA1 and J0613+1708, respectively. The continuum source J0613+1708 is listed in the VLBA calibrator list (Fomalont et al., 2003) and was observed at an unresolved K-band flux of ∼40 mJy in our observations with VERA. Intermittent observations of BL Lac, DA55 or 3C84 were made every 1.5 hrs for bandpass and group delay calibration. Typical observing sessions were ∼8 hrs long, providing ∼2.5 hrs on-source time and good uv-coverage.

The a-priori delay tracking models used in correlation were improved upon after basic inspection of fringe map analysis to correct for the maser offset from the delay tracking center. In this step we also refined delay tracking solutions using more accurate antenna positions utilising global positioning system (GPS) measurements which also measured atmospheric water vapour zenith delays at each station (Honma et al., 2008a) and include fine corrections for the earth rotation parameters.

In total there were 12 observation epochs with intended spacing of around 3 months. In three epochs, toward the middle of the monitoring observations, we experienced antenna trouble at at least one station - rendering phase referencing between the quasar and maser impossible. Data from these epochs were not used for parallax measurement, but their self-calibrated maps and fluxes contributed to proper motion and spectrum analyses. Epoch 9 suffered some unexplained fatal error and subsequently could not

Table 4.1: Summary of observations

Epoch number	Observation date	Modified Julian date	Number of features
1	23rd Nov 2008	54793	15
2	1st Feb 2009	54863	15
3	18th May 2009	54969	10
4	28th Aug 2009	55072	12
5	15th Sep 2009 †	55089	12
6	27th Sep 2009 †	55101	14
7	24th Oct 2009 †	55128	13
8	13th Dec 2009	55178	14
9	28th Jan 2010 †	55224	-
10	10th Feb 2010	55237	12
11	4th Apr 2010	55290	8
12	11th Aug 2010	55419	9

† These epochs were not used in parallax determination.

Table 4.2: The general properties of H_2O masers in S255IR-SMA1 detected with VERA.

Maser ID	$V_{\rm LSR}$ (km s^{-1})	Detected epochs	$\Delta\alpha\cos\delta$ (mas)	$\Delta\delta$ (mas)	$\mu_\alpha\cos\delta$ (mas yr^{-1})	μ_δ (mas yr^{-1})
A	4.798	12345678*10 11 12	26.851	-6.846	1.03 ± 0.16	-1.01 ± 0.18
B	4.166	12345678*10**	8.894	-15.367	-1.31 ± 0.18	-2.83 ± 0.16
C	4.374	12345678*10 11 12	5.322	-12.98	-1.93 ± 0.21	-2.10 ± 0.20
D	5.428	12345678*10 11 12	4.018	-11.924	-1.27 ± 0.20	-0.09 ± 0.88
E	3.745	*****678*10**	0.604	-11.377	-2.30 ± 0.17	-1.45 ± 0.15
F	5.851	***456*8*10**	-0.87	-6.76	-1.79 ± 0.20	-1.70 ± 0.20
G	0.161	12345678*10 11 12	0.046	-4.794	-2.95 ± 0.16	-0.13 ± 0.15
H	3.953	12345678*10 11 *	-1.019	-3.62	-1.97 ± 0.18	-1.55 ± 0.19
I	1.846	1234********	-4.352	2.585	-2.73 ± 1.38	-0.90 ± 0.71
J	11.322	*2345678*10 11 12	73.987	131.344	-1.20 ± 0.17	0.49 ± 0.17
K	10.275	***45678*10 * 12	85.739	152.066	-1.42 ± 0.16	0.05 ± 0.15
L	12.169	12345678*10 11 12	88.909	152.196	-0.95 ± 0.17	0.27 ± 0.16
M	11.539	*****678*10 11 12	150.041	253.838	-2.95 ± 0.16	1.22 ± 0.29
N	6.476	**345*78*** 12	275.557	245.008	1.83 ± 0.19	1.47 ± 0.25
O	5.849	12**********	249.885	235.729	–	–
P	3.11	12**********	43.809	8.626	–	–
Q	3.321	12**5678****	40.716	5.044	0.51 ± 0.16	-2.83 ± 0.45
R	2.689	1**********	83.969	29.766	–	–
S	3.11	1**********	76.449	22.751	–	–
T	0.998	*2**********	1.52	39.99	–	–
U	5.217	1**********	22.615	-11.963	–	–
V	5.212	*2**********	18.842	-15.06	–	–
W	4.585	1**********	16.933	-15.294	–	–
X	3.324	*****6******	-2.696	-5.001	–	–
Y	13.008	*2**********	173.378	264.51	–	–

Column (2): Line of sight velocities are quoted as that which wa measured for the first detection.
Column (3): Numbers indicate detection in the corresponding epoch, while asterisk represents non-detection.

be imaged, only its spectrum was useful. The observation calendar is summarised in Table 4.3.

All data were reduced using the Astronomical Image Processing System (AIPS) developed by the National Radio Astronomy Observatory (NRAO). Data reduction utilised the *inverse phase-referencing* method for VERA data, which was introduced in Imai et al. (2012). A detailed guide is given in Burns et al. (2015). Flux calibration was performed using system temperatures and gain information recorded at each station. Next we applied the aforementioned delay tracking solutions which are source specific. A characterised noise signal was injected into the two VERA beams to allow correction of the delay introduced by differences of hardware in the dual beam system (Kawaguchi et al., 2000), and group delay was calibrated using the intermittent scans of BLLAC, DA55 or 3C84. What remains at this point are time-varying phase residuals attributed to atmospheric fluctuations which, at 22 GHz, are dominated by the dynamic troposphere (Asaki et al., 2007). Atmospheric calibration was carried out by fringe fitting phase residuals using the emission from a strong reference water maser at solution intervals of 1 or 2 minutes. These solutions were then applied to the visibility data of J0613+1708, thus phase-referencing it. Imaging of J0613+1708 then gives the relative astrometric position of water masers in S255IR-SMA1 with respect to J0613+1708. The phase solutions obtained from the reference maser were also applied to the other maser data of S255IR-SMA1 thus self-calibrating it and generating high dynamic range, astrometrically accurate maser maps.

Maser maps were produced by applying the CLEAN procedure, based on Högbom (1974), to emission peaks registered at a signal-to-noise cutoff of 7. Following common nomenclature, a maser 'spot' refers to an individual maser brightness peak, imaged in one spectral channel, and a maser 'feature' refers to a group of spots which are considered to emanate from the same physical maser cloud, thus a maser feature typically comprises of several maser spots. Maser spots are categorised into features when they are part of the same spectral feature and found within 1 mas of another spot in that feature. We define the nominal astrometric position of a maser feature by determining the flux weighted average of the brightest three spots in the feature.

4.1.3 Results

4.1.3.1 Maser detections and distribution

In total, 25 individual maser features were detected with VERA, each comprising of multiple maser spots. The LSR velocities, detection frequency, positions and proper motions of all maser features are summarised in Table 4.4 (positions are quoted as offsets from the phase tracking center in the maser beam, *see* Section 2). The time-evolution of the maser spectrum is shown in Figure 4.1, and shows some velocity features to be stable while others are more variable. The increase in brightness of the emission peak at 2 km s^{-1}, at around $MJD = 55230$ days, is discussed in Section 4.1.4.1.

The distribution of water maser features in S255IR-SMA1 is shown in Figures 4.2 and 4.3. Masers form three main groups; those located to the NE of the system which are slightly redshifted with respect to the star ($V_{LSR} = 5.25$ km s^{-1}, see Section 4.1.4.3), those in the SW which are slightly blueshifted with respect to the star, and the more

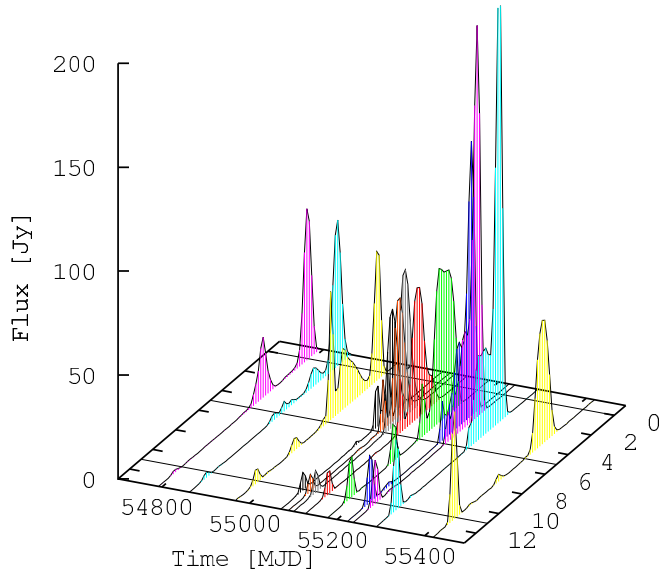

Figure 4.1: Scalar averaged spectrum of maser emission in S255IR-SMA1 as a function of time. Colours are arbitrary.

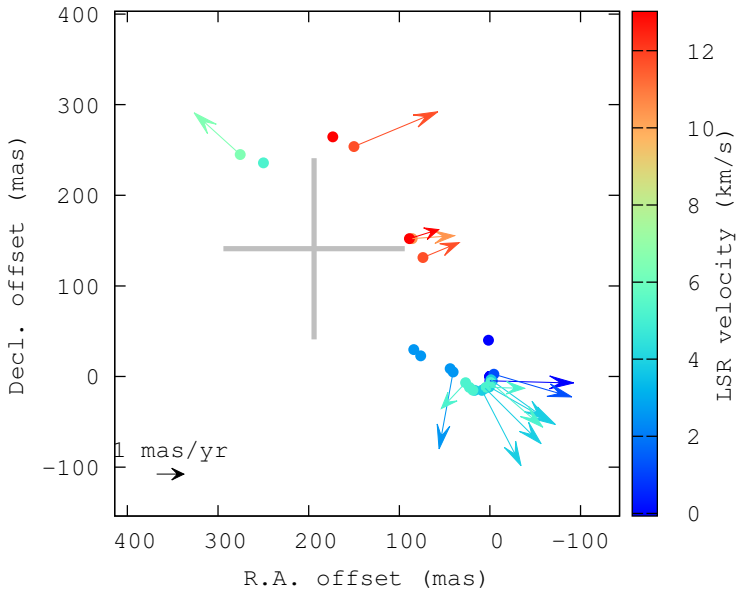

Figure 4.2: Distributions, internal proper motions and line-of-sight velocities of H_2O maser features in S255IR-SMA1. The peak position of the centimeter source from Rengarajan & Ho (1996) is indicated with a cross whose size indicates to the positional error in the measurement.

redshifted water masers ($\sim$ 12 km s^{-1}) near to the source of the centimeter emission marked as a plus sign in Figure 4.2. We refer to these three maser groups as the 'NE masers', the 'SW masers' and the 'red masers', respectively.

4.1.3.2 Annual parallax

The annual parallax of a maser source, obtained via astrometry, can be used to measure its trigonometric distance. Astrometric motions of maser features trace sinusoidal paths across the sky-plane. This motion can be separated into a linear component which arises from the proper motion of the maser with respect to the Sun, and a sinusoidal component caused by the annual parallax. Astrometric maser motions are deconstructed into these separate components by simultaneous fitting of data with a linear and a sinusoidal function, assuming a common distance. We only performed this fitting for maser features which were observable in at least 7 epochs, spanning at least one year, and that were not spatially resolved. Maser features suitable for fitting are indicated by underlined, boldface feature ID's in Table 4.4, and are labelled in Figure 4.2. We avoided using features C and D, eventhough they were present in 11 epochs, because their interaction with each other spatially distorted the maser emission in our images, compromising astrometric accuracy. These maser features were used in proper motion analysis.

We measured an annual parallax of $\pi = 0.563 \pm 0.036$ mas, corresponding to a source distance of D $= 1.78^{+0.12}_{-0.11}$ kpc, very close to the annual parallax of S255 measured with 6.7 GHz methanol masers by Rygl et al. (2010), using the European VLBI Network (EVN). Both ours and the parallax distance of Rygl et al. (2010) differ from the kinematic distances determined previously - about 2.5 kpc (Russeil et al., 2007; Chavarría et al., 2008; Ojha et al., 2011), likely because S255 is in the Galactic anticenter direction, with $l = 193°$, where systemic line of sight velocities approach zero - making kinematic distances unreliable. As such, the discrepancy between trigonometric and kinematic distances is reasonable and the distance obtained by parallax should be adopted.

4.1.3.3 Systemic and internal proper motion

We measured the proper motions of maser features that were detected in at least 3 epochs by measuring motions relative to Feature G (the reference maser) in the self-calibrated maps. The absolute proper motion of Feature G, obtained from the parallax fitting stage outlined in Section 4.1.3.2, was then added to all other masers, thus converting proper motions relative to Feature G into absolute proper motions relative to the reference source, J0613+1708. Errors were calculated in quadrature to include the uncertainty in the motion of Feature G.

The observed proper motion of a maser feature is a combination of two components; the 'source systemic motion' which is a group motion common to all masers arising from the relative motion of the SFR and the Sun, and the 'internal motions' which are motions of individual maser features with respect to the driving source. In S255IR-SMA1 we were able to measure proper motions in both the NE and the SW masers. First we averaged the motions of masers associated with each outflow lobe to get the individual lobe proper motions. Then we determined the systemic motion from the residual of summing the

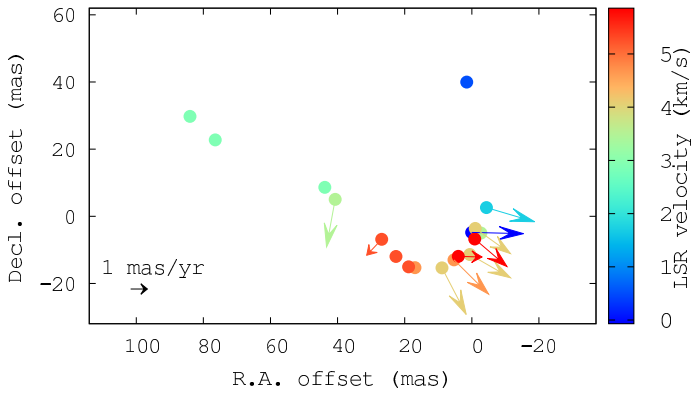

Figure 4.3: Zoom of the SW micro-bowshock region in S255IR-SMA1. Two possible jet models, one corresponding to the narrowest jet and one to the widest jet, are drawn with long black dashes and short grey dashes, respectively.

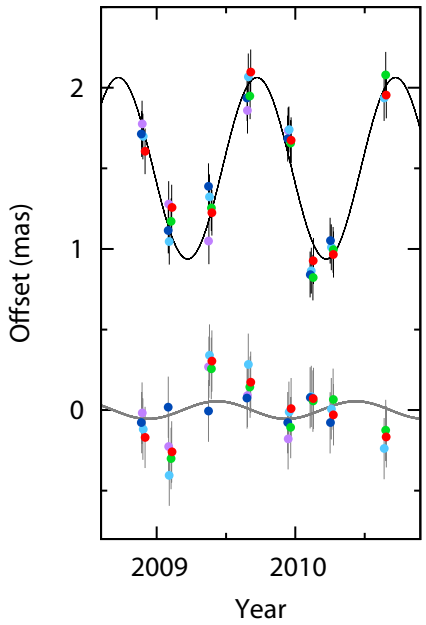

Figure 4.4: Annual parallax motions of 5 maser features in S255IR-SMA1 which are coloured arbitrarily. The upper, black line shows the modelled parallax in the Right ascension direction while the grey line below shows the same for the declination direction. Small horizontal offsets are introduced for readability.

proper motions of the lobes, assuming symmetry. We did not include the red masers in this calculation as they do no appear to be associated with the symmetric outflow system. We derive a (heliocentric) systemic motion of $(\mu_\alpha \cos\delta,\ \mu_\delta) = (-0.13 \pm 0.20,\ -0.06 \pm 0.27)$ mas yr^{-1}, where errors are the quadrature sum of the average error for each lobe, divided by $\sqrt{N}$ where N is the number of features in the lobe. The result is consistent with the VLBI observations of S255IR-SMA1 by Rygl et al. (2010) made using the 6.7 GHz methanol maser which is considered to be a good tracer of systemic motions since such masers are excited radiatively at close proximity to the star.

Subtracting the systemic proper motion from the measured proper motions gives the internal motions of water masers with respect to the source. These are shown in Figures 4.2 and 4.3, and reveal a highly collimated bipolar jet orientated in the NE-SW direction. At the tip of jet in the SW direction the masers form a "micro-bowshock" structure, which resembles the maser micro-bowshock discovered by Furuya et al. (2000) in the low-mass YSO micro-jet source S106-FIR. Our data represents the first comparable case seen in an MYSO. The micro-bowshock in S255IR-SMA1 has a width of 30-50 mas and is 188 mas from the system center, assumed to be midway between the NE and SW lobes of the jet, which has a position angle of PA = 49°.

4.1.4 Discussion

4.1.4.1 Time variation of maser velocity and brightness

During our monitoring observations several maser features exhibited velocity drifts where the spectral peak of the maser feature increased or decreased in LSR velocity by some small amount (typically less than 1 km s^{-1} yr^{-1}). It was only the spectral peak of the feature that changed; the wider bulk of the spectral feature remained stable in velocity. As such the velocity drifts are probably not physical cloud accelerations, and are instead subtle changes in the internal velocity structure of the maser cloud.

We observed an alignment where the spectral peaks of two bright maser features (Features C and G) drifted into the same velocity channel. This explains the flux increase seen at about $MJD = 55230$ days in Figure 4.1, which is an alignment in velocity only and not an alignment on the sky-plane. This situation is different to a 'burst' which is where masers align spatially, thereby increasing the path length of the masing material in the line of sight to the observer - causing a sudden increase in maser brightness of a few orders of magnitude (*ex.* Shimoikura et al. 2005; Burns et al. 2015)

Interestingly, Feature J exhibited a steady increase in flux from 4 to 82 Jy which can be seen clearly in Figure 4.1 at $v_{\rm LSR} = 11.3$ km s^{-1}. This increase was not seen to be caused by a velocity convergence as described above, and no changes were seen in the structure of the masers in our images. As such the slow flux increase may be attributed to some physical change in the environment of the masers, near to S255IR-SMA1 - however we cannot speculate further on the cause.

4.1.4.2 Quasar jet in J0613+1708

The reference source J0613+1708 has a quasar jet in the North direction. Non-point-like structures in the positional reference source can influence the 2D Gaussian fitting used

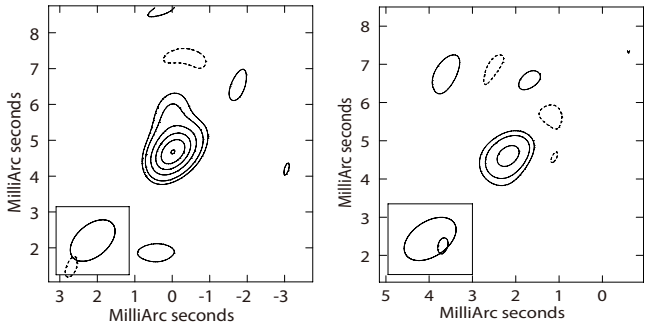

Figure 4.5: J0613+1708 images from (*left*) epoch 1, in which good observing conditions were seen at all VLBI stations, and in and (*right*) epoch 4, in which conditions were not so good. The contours correspond to -3,3,5,9,13,17,21 times the image *rms* noise which are 1.8 mJy and 2.8 mJy for epochs 1 and 4 respectively.

in determining its position from the interferometric images - in turn degrading maser astrometry. We checked to see if such an issue affected our data.

The extent of the jet in our images depended on the final quality of the inversely phase referenced quasar image, which differs for each observing epoch depending on observing conditions - in some epochs the jet is clearly resolved while in others the jet is buried in noise (Figure 4.5). An inflence, if present, would manifest as a reduced astrometric accuracy in the Dec. direction; the direction of the jet. Yet, since the parallax fitting residuals in R.A. and Dec. were similar it seems that the jet structure did not degrade the astrometric accuracy of our observations.

4.1.4.3 Properties of the micro-bowshock in S255IR-SMA1: jet driven nature of the molecular outflows

A maser micro-bowshock is a jet whose leading surface is traced by masers. Bipolar outflow- and jet-tracing maser observations are frequently reported in the literature (*ex.* Imai et al. 2007; Nagayama et al. 2008; Moscadelli et al. 2011; Torrelles et al. 2014 and G236.81+1.98 in Choi et al. 2014), what makes a micro-bowshock jet special is its intelligibility. Jet tracing masers typically become more chaotic in distribution and motion, losing their bow-shock shape as they propagate into the local medium, making it difficult to distinguish whether masers are associated with a jet or a molecular outflow. The risk of misinterpretation is especially dangerous when using water masers, which are variable, have short lives and may be produced in bias at isolated regions of high collisional energy - rather than giving uniform coverage of the phenomenae at hand. The clean edge traced by masers in a micro-bowshock lets there be no ambiguity that it is a jet which is being traced and we can directly derive the geometry, physical scale and velocity of the jet from the maser distribution and proper motions.

In order to determine the 3D motion of the jet at the source we must convert to the velocity frame of the central star in S255IR-SMA1. The LSR velocity range of the rotating core observed by Zinchenko et al. (2015) is $3-7$ km s^{-1} for CH_3OH 4_2-3_1 E and $3-8$ km s^{-1} for CH_3CN 12_3-11_3. Taking the central velocity of these ranges should give

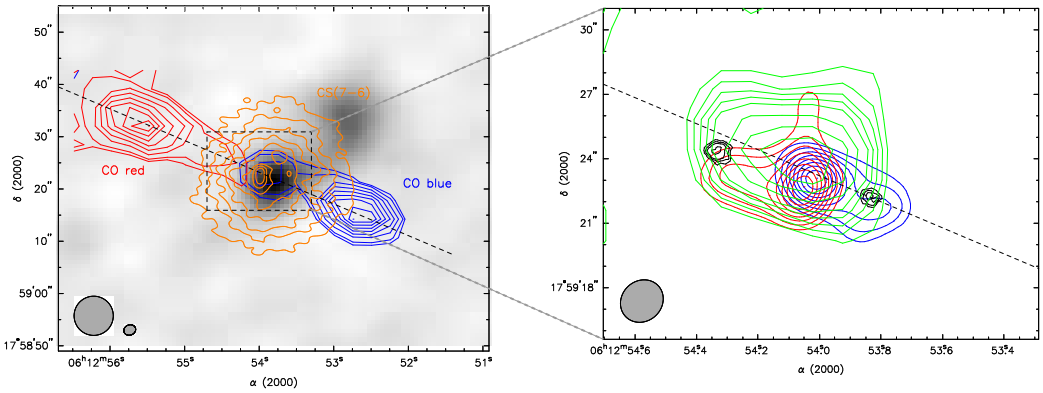

Figure 4.6: Molecular line maps of Zinchenko et al. (2015) showing *left:* the large scale, 7000 year old CO $(3-2)$ molecular outflow, overlaid onto the dust continuum image at 0.8 μm, showing also the CS $(7-6)$ core as yellow contours, and *right:* the smaller scale, 1000 year old molecular outflow, where blue and red contours show $HCO^+(4-3)$ at velocity intervals of -19 to -3 km s^{-1} for the blue wing and 11 to 27 km s^{-1} for the red wing (Zinchenko et al., 2015). Black contours show the positions of FeII bow shocks (Wang et al., 2011) and green contours indicate the 2 cm continuum emission (Rengarajan & Ho, 1996). The short dashed line indicates the orientation of the outflow system.

the best estimate of the line of sight velocity of the central object; the protostar, giving $v_{LSR} = 5.25$ km s^{-1}. The average line of sight velocities of the NE and SW jet masers are 6.48 km s^{-1} and 4.03 km s^{-1}, respectively giving a central systemic line of sight velocity of 5.26 km s^{-1}, consistent with the velocity of the protostar. As such, taking a symmetric velocity structure, each lobe has a line of sight velocity of $v_{LOS} = 1.22$ km s^{-1} relative to the protostar, with the NE maser jet on the receding side of the system and the SW jet approaching side.

As mentioned in Section 4.1.3.3, the internal proper motions of the jets are derived assuming a symmetric system. By subtracting the systemic proper motion from the average proper motions of masers in each jet lobe we calculate sky-plane jet lobe velocities of $v_{sky} = 18.74$ km s^{-1}. We see that $v_{sky} > v_{LOS}$ meaning that the 3D motion vectors are dominated by proper motions i.e. the jet move primarily in the sky-plane (we calculate a system inclination of $i = 86.25°$ to the observer). The 3D velocity of each jet lobe is $v_{3D} = 18.78$ km s^{-1} with respect to the protostar, with a position angle of PA $= 49°$ which matches reasonably well with those of the larger molecular outflows (PA $= 67°$, Zinchenko et al. 2015). The orientations of these outflows align to the rotation axis of the core/disk.

The age of the jet is given simply by the physical length of the jet divided by its velocity. Since the absolute position of the protostar is uncertain it is intuitive to instead use the half separation of the maser lobes. The semi-major angular separation between lobes is 188 mas, which, at a distance of 1.78 kpc corresponds to a physical length of $\sim$ 335 AU. Using the 3D velocity we calculate a jet dynamic timescale of $t_{dyn} = 130$ years.

We infer the width of the jet directly from Figure 4.3, considering two possible shapes allowed by the observed maser distribution. The narrower has a width of 30 mas while the wider has a width of 50 mas. This corresponds to a physical width size range of 55 to 90 AU, giving a collimation degree of 7.5 to 12.5.

In this work we reveal the presence of a highly collimated primary jet in S255IR-SMA1. The presence of such a jet provides a suitable driving mechanism for the outflows in S255IR-SMA1. The differences in ages of the jet and outflows suggest an episodic nature - we discuss this in the next section. Our VLBI results, when considered in the context of the findings of Wang et al. (2011) and Zinchenko et al. (2015), present clear evidence of a disk-jet-outflow scenario, an arrangement common to low-mass YSOs, in S255IR-SMA1, a massive star of ~ 20 $M_{\odot}$.

4.1.4.4 High-mass vs low-mass star formation: Episodic accretion

Even if the outflow driving mechanism of MYSOs resemble their low-mass counterparts, we still cannot freely scale up low mass star formation without encountering the issue of radiation pressure - which stands as the most predominant issue separating high- and low-mass star formation; it is still unclear as to how material at the inner radii of the disk accretes onto the star in the face of a strong stellar UV field (*see review by* Zinnecker & Yorke 2007). According to the current theories of star formation radiation pressure should halt the accretion process, limiting the mass of stars to about $8M_{\odot}$ (Palla & Stahler, 1993).

In S255IR-SMA1 we find clear evidence in direct contrast of this widely accepted standpoint. We see that that the most recent ejection event in S255IR-SMA1 takes place well inside a region of radio centimeter emission (the green contours in Figure 4.6) indicative of the recent production of stellar UV radiation. The scale of the maser jet (188 mas) is far smaller than the extent of the radio emission ($\sim 3''$) suggesting that the most recent accretion event happened *despite* the establishment of a compact H_{II} region - meaning that accretion must have overcome radiation pressure during the most recent episode. This is strong evidence that some hidden mechanism is at work which has allowed the accreting material to bypass radiation pressure in S255IR-SMA1. Here we discuss one of the proposed methods of circumventing the luminosity problem, recently reported by (Hosokawa et al., 2015).

During an intense burst of accretion a protostar is thought to inflate (Yorke & Bodenheimer, 2008; Hosokawa et al., 2010). The increased stellar radius causes the effective temperature to drop - which in turn reduces the intensity of the stellar UV feedback, enabling steady accretion on to the star. Hosokawa et al. (2015) showed that, in the case of primordial massive stars, if accretion bursts happen at a rate which is quicker than the gravitational contraction of the star then it is possible to keep the star 'bloated' long enough for the star to accrete tens to hundreds of solar masses, while suppressing the formation of a HII region. They propose that the accretion of a disk fragment would be sufficient to cause inflation of the star, and that repeating burst on timescales shorter than a few 10^4 years would be sufficient to outpace gravitational contraction. Their models show that strong UV radiation from the star forms compact HII regions which grow and wane depending on the accretion activity. As such, the main issue separating

high-mass and low-mass star formation - radiation pressure - may be circumvented by means of episodic accretion.

Mass accretion rates and the frequency of accretion episodes are not directly observable in a practical sense as monitoring observations with temporal baselines of tens of thousands of years would be required. Fortunately, the tight correlation between accretion and outflow activity (Corcoran & Ray, 1998; Caratti o Garatti et al., 2015) means that the accretion history of a young star can be inferred from its history of ejections - which is observable as a series of symmetric shock fronts extending from the star.

At least three episodes of ejection are known to have taken place in S255IR-SMA1. The larger, and therefore older outflow was observed in ^{12}CO(2−1) and has dynamic age of about 7000 years (Wang et al., 2011), and a second younger ejection event is also seen, whose presence is indicated by bow shocks of FeII (Wang et al., 2011). Shock-front tracers are invaluable in distinguishing truly separate ejection events from apparently separate outflow events which may arise simply from differences in gas excitation conditions within a single outflow. Bow shock tracers appear at the leading tip of an ejection and therefore also provide reliable indicators of extent and dynamic timescales. The younger ejection traced by FeII was also seen in the HCO^+ maps of Zinchenko et al. (2015) (*see* Figure 4.6) who estimate its dynamic age to be 1000 years.

The 7000 year old ejection and the 1000 year old ejection align with each other in the ENE-WSW direction (Figure 4.6) - to which the 130 year old maser jet (*this work*, Goddi et al. 2007) also aligns reasonably - suggesting no large change in the orientation of the system over this period. Consequently, the time between ejection events, and therefore the inferred time between accretion bursts is of the order of a few thousand years, i.e less than 10^4 years, which, according to the models of Hosokawa et al. (2015), is frequent enough to have repeatedly bloated the young star in S255IR-SMA1, thus holding off gravitational contraction. The inferred accretion history indicates that it may have been plausible S255IR-SMA1 to have achieved a prolonging of accretion well into the production of a compact HII region via the episodic accretion mechanisms proposed in Hosokawa et al. (2015).

Zinchenko et al. (2015) find a rotating core at the center of SMA1 which very likely houses a circumstellar disk. The axis of rotation aligns to the outflow, as is expected in a disk-jet-outflow system and they also remark that any such disk must be significantly fragmented. In conclusion, it would appear that for the case of S255IR-SMA1 the formation of its massive star could be explained using scaled-up features commonly associated with low-mass star formation; a disk-jet-outflow system, with the added ingredient of episodic accretion bursts from the fragmented circumstellar disk.

4.2 Dispersal of angular momentum

Of the mainstream theories it is emerging that disk aided accretion is a strong candidate for explaining the formation of stars up to at least B type, as observational evidence of disks associated with such accreting stars is found (Hirota et al., 2014; Beltrán et al., 2004). Such protostellar disks are thought to be able to shield accreting material from stellar radiation and transport it down to radii of ∼100 au from the central object (Zinnecker & Yorke, 2007; Cesaroni et al., 2007).

However, one necessity of disc accretion theory which has yet to be properly confronted with observations concerns how angular momentum is carried away from the protostellar disk to enable accretion. Proposed methods of removing angular momentum include Alven waves in the disk material, magnetic breaking in the ionic component of the rotating disk, and by physically carrying rotating material away from the disk vertically via magnetocentrifugally driven rotating jets (*see review by* Konigl & Pudritz 2000).

In addition to disk observations it is therefore also appealing to look for evidence of rotating jets near massive young stellar objects (MYSOs) in order to uncover their role in the angular momentum budget of accreting stars. A demonstration of such an investigation is the *Ori-S6* MYSO (Zapata et al., 2010). This kind of work poses an observational challenge since MYSOs are deeply embedded and rarely have observable collimated jets (Navarete et al., 2015). We therefore turn to masers in our investigation of rotation in MYSO jets.

Collisionally excited H_2O masers are associated with a diverse range of kinematic phenomena in the young stellar objects (YSOs) of star forming regions (SFRs), including jets, wide-angle outflows and expanding shells (*see for example* Torrelles et al. 2012). The bright and compact masers are ideal for very long baseline interferometry (VLBI) observations, which can penetrate the obscuring parent cores in which massive stars form and reveal the motions of young jets (Moscadelli et al., 2011; Furuya et al., 2000). Multi-epoch observations allow determination of the internal 3D kinematics at shocked regions via combination of line-of-sight and proper motion measurement. Furthermore the annual parallax of a maser source provides a precise estimation of its distance, which is crucial for evaluating its physical properties. As such VLBI is an indispensable technique for studying the formation of stars and provides a mechanism for the search for rotating MYSO jets.

VLBI observations in this paper were carried out using VERA (VLBI exploration of radio astrometry) (Kobayashi et al., 2003) which is a Japanese VLBI network dedicated to maser astrometry of primarily Galactic sources. The bright H_2O maser in S235AB was chosen as a VERA target for its interesting 'maser burst' behaviour (up to 120 Jy) (Felli et al., 2007) which has a dominant blue-shift maser (DBSM) spectrum. Its annual parallax was also sought for it's contribution to the mapping of the Perseus Arm.

In addition to H_2O masers, the S235AB region also exhibits class I methanol masers (Kurtz et al., 2004; Pratap et al., 2008), and SiO jet (Burns et al., 2016a), and two bipolar outflows of HCO^+, driven from a dusty molecular core seen in 450 and 850 μm (Felli et al., 2004). Felli et al. (2006) proposed a *class I* mid infrared source, S235AB-MIR, as the outflow progenitor from *Spitzer* images. By SED modelling of sub-millimeter continuum data from Felli et al. (2004) and *Spitzer* mid-infrared photometries, Dewangan & Anandarao (2011) showed S235AB-MIR to be the only massive YSO in the S235AB cluster, with a stellar mass of 11 $M_\odot$ and still accreting.

No centimeter emission has been detected in S235AB-MIR (Tofani et al., 1995; Felli et al., 2006), suggesting no significant development of an ultra compact H_{II} region (UCHIIR). Saito et al. (2007) estimated the most massive member of the S235AB

Table 4.3: Summary of observations made with VERA.

Observation Epoch	Date	MJD	Detected spots
1	2013 Jan 29	56321	17
2	2013 Feb 21	56344	18
3	2013 Mar 15	56366	26
4	2013 Apr 21	56403	12
5	2013 Sep 29	56564	30
6	2013 Nov 02	56598	24
7	2013 Dec 02	56628	26
8	2014 Jan 28	56685	21
†9	2014 Mar 11	56727	19
†10	2014 Apr 29	56776	19

† These epochs were not used in parallax determination.

cluster to be of spectral class B1 from $C^{18}O$ observations. Thus, a plausible interpretation above picture is that of a deeply embedded accreting *B*-type star which is too young to produce a detectable UCHIIR.

4.2.1 Observations and Data Reduction

Simultaneous VERA observations of S235AB-MIR and the continuum reference source J0533+3451 were made in dual-beam mode (Kawaguchi et al., 2000). Observing the maser and reference source simultaneously removes the need to slew antennae and interpolate phase measurements between sources, enabling excellent determination of the dynamic troposphere phase contribution (*see* Asaki et al. 2007).

Phase tracking centers were set to $(\alpha, \delta)_{\rm J2000.0} = (05^{\rm h}40^{\rm m}53^{\rm s}.38445496, +35°41'48".4470)$ and $(\alpha, \delta)_{\rm J2000.0} = (05^{\rm h}33^{\rm m}12^{\rm s}.7651060, +34°51'30".336990)$ for S235AB-MIR and J0533+3451, respectively. The continuum source J0533+3451 is listed in the VLBA calibrator list (Petrov, 2012) and was observed at an unresolved *K*-band flux of ∼20 mJy in our observations with VERA. Intermittent observations of BL Lac, DA55 or 3C84 were made every 1.5 hrs for bandpass and group delay calibration. Typical observing sessions were 8 hrs long, providing 2.5 hrs on-source time and sufficient *uv*-coverage.

Left-handed circular polarisation signals were sampled at 2-bit quantisation, and filtered with the VERA digital filter unit (Iguchi et al., 2005). The total bandwidth of 256 MHz was divided into 16 intermediate frequency (IF) channels, each with a bandwidth of 16 MHz. One IF was allocated to the maser signal, assuming a rest frequency of 22.235080 GHz. The other 15 IFs, in adjoining frequency, were allocated to J0533+3451. Signal correlation was carried out using the Mitaka FX correlator (Chikada et al., 1991). Channel spacings of 31.25 kHz were used for the maser data, corresponding to a velocity resolution of 0.42 km s^{-1}.

Global positioning system (GPS) measurements of the atmospheric water vapour content at each station were used to refine an a-priori model of expected atmospheric delay (Honma et al., 2008a). Solutions were applied post-correlation.

VERA observations were conducted in 10 epochs, closely spaced to support maser identification in view of the extreme variability of emission. The observation calendar is summarised in Table 4.3. An error (possibly caused by a shift in the adopted antenna positions) in our correlation settings in epochs 9 and 10 resulted in inaccurate astrometry such that data from these epochs could not be used in measurement of the annual parallax. These data were only used in maser distribution and line of sight velocity analysis.

All data were reduced using the Astronomical Image Processing System (AIPS) developed by the National Radio Astronomy Observatory (NRAO).

Data were reduced using the *inverse phase-referencing* method for VERA data, which was introduced in Imai et al. (2012). In this approach the bright maser emission is used to calibrate dynamic tropospheric fluctuations in phase and rate - thus acting as the phase reference - while group delay is solved using a bright continuum source. These solutions are applied to the data of a nearby continuum source whose precise co-ordinates are already known. The relative position of the maser to the nearby continuum source gives the accurate position of the maser.

The main advantage of the inverse phase-referencing technique is its ability to detect weak continuum sources ($\sim$10 mJy, Imai et al. 2012). Furthermore, since the phase-rate solutions applied to the nearby reference source are also used to self-calibrate the maser data, the phase-referenced maser maps have high dynamic range.

Emission peaks in the maser maps were imaged using the CLEAN procedure, based on Högbom (1974) and detections were registered at a signal-to-noise cutoff of 5. Following common nomenclature, a maser 'spot' refers to an individual maser brightness peak, imaged in a specific velocity channel, and a maser 'feature' refers to a group of spots which are considered to emanate from the same physical maser cloud. Maser spots are categorised into features when they are grouped within 1 mas of another spot, and are continuous in velocity. Features and their associated spots are denoted by letters and numbers respectively in column 1 of Table 4.4.

4.2.2 Results

4.2.2.1 Maser detections

In total, 19 maser features were catalogued comprising some $\sim$60 spots, all of which showed notable time variability. Maser detections are summarised in Table 4.4. Features can be separated into three main groups by comparing local standard of rest (LSR) velocities to that of the molecular core, which has a velocity of -17 km s^{-1} (Felli et al., 2004). The groups are: 'red lobe', 'core velocity' and 'blue lobe' masers, which were observed from $+2$ to $+14$, around -18, and from -55 to -65 km s^{-1}, respectively.

Red lobe and core velocity masers were detected sporadically, and were weak - with typical fluxes of ≤ 1 Jy. The red lobe group had only two individual maser features and the core velocity masers had only one maser feature. Masers from these groups reside loosely together in a region of about 120 $\times$ 120 au.

Blue lobe maser emission was strong, extremely variable and exhibited a 'burst' nature where the cross-power flux rose from 10^0 Jy to 10^2 Jy on three occasions. These masers are blueshifted > 40 km s^{-1} with respect to the molecular core. Blue lobe masers

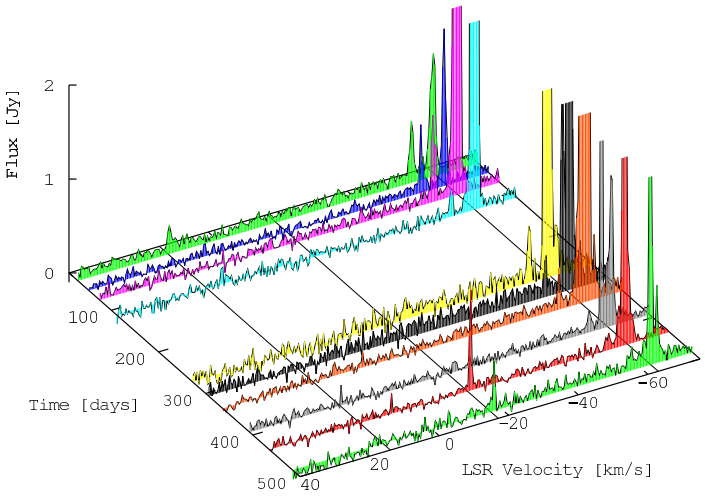

Figure 4.7: Scalar averaged spectra of the H_2O emission for each epoch, limited to 2 Jy to show weaker detections. Lines of constant velocity indicate the red lobe, the core velocity and the blue lobe maser velocities in descending velocity order.

reside in a compact region of about 15 × 15 au at a separation of 2" from the other maser groups.

Relative intensities and time variation of the aforementioned velocity components are shown in Figure 4.7. The spectrum of S235AB-MIR exhibits a classical DBSM profile, providing early evidence that the water masers may be driven by a jet (Caswell & Phillips, 2008; Motogi et al., 2013, 2015). Figure 4.8 shows the velocities and distributions of all detected maser features, revealing a jet. A dashed line drawn through the central positions of the main maser groups traces a position angle of $PA = 217°$ which delineates the geometric axis of the system. The right-hand panel of Figure 4.8 shows a position-velocity (p-v) diagram across this axis.

4.2.2.2 Parallax and proper motions

Astrometric motions of masers are a combination of a linear component corresponding to the proper motion of the maser on the sky, and a sinusoidal component due to annual parallax. These two components are separated by simultaneous fitting of a linear and sinusoidal function to the observed data. Long temporal baselines and dense sampling are vital to correctly separate the two components, therefore we only fit parallaxes using masers associated with the persistent features; A and B.

We performed data fitting using 3 different approaches: individual, group and feature fitting. 'Individual fitting' refers to fitting the parallax and proper motion of each individual maser spot independently. Fitting is done using the same velocity channel at each epoch i.e. we assume non-acceleration in the line of sight. We use only the most stable masers that were identifiable in at least 5 epochs and persist for at least 1 year.

'Group fitting' involves fitting the astrometry of multiple spots together by assuming a common distance. In this procedure we use all masers that are identifiable in at least

Table 4.4: The general properties of H_2O masers in S235AB-MIR detected with VERA.

Maser ID	V_{LSR} (km s^{-1})	Detected epochs	$\Delta\alpha\cos\delta$ (mas)	$\Delta\delta$ (mas)	$\mu_\alpha\cos\delta$ (mas yr^{-1})	μ_δ (mas yr^{-1})	π (mas)
$A1$	−60.06	**345**8**	−6.95	32.45	0.62 ± 0.27	-1.95 ± 0.22	
$A2$	−60.48	**3*5**8**	−6.92	32.47			
$A3$	−60.90	1*3**4**56*** 10	−6.76	32.88	1.30 ± 0.29	-2.36 ± 0.23	
$A4$	−61.32	1234**56**789 10	−6.72	32.88	1.17 ± 0.18	-2.42 ± 0.15	0.713 ± 0.092
$A5$	−61.74	1**23***56**7**8* 10	−6.68	32.91	1.34 ± 0.19	-2.48 ± 0.15	0.675 ± 0.061
$A6$	−62.16	1***567**8**9 10	−6.69	33.01	1.20 ± 0.25	-2.43 ± 0.20	0.558 ± 0.083
$A7$	−62.58	**12****56*89 10	−6.65	33.09	1.24 ± 0.22	-2.43 ± 0.18	
$A8$	−63.00	12**5**89 10	−6.61	33.09	1.08 ± 0.23	-2.38 ± 0.18	
$A9$	−63.42	1**2****5**8**9** **10**	−6.54	33.02	0.95 ± 0.23	-2.37 ± 0.18	
$A10$	−63.84	123***5****9 10	−6.44	32.97	0.60 ± 0.37	-2.36 ± 0.29	
$A11$	−64.26	*23******	−6.57	32.81			
$A12$	−64.68	**3*******	−6.49	32.70			
						Average	$\pi = 0.649 \pm 0.144$
	Feature A group fitting				1.06 ± 0.08	-2.35 ± 0.07	$\pi = 0.656 \pm 0.038$
	Feature fitting result				0.36 ± 0.19	-2.45 ± 0.10	$\pi = 1.018 \pm 0.093$
$B1$	−60.06	***4******	−6.33	36.85			
$B2$	−60.48	***4*6****	−6.27	36.81			
$B3$	−60.90	**34*67***	−6.67	37.18	1.26 ± 0.31	1.47 ± 0.24	
$B4$	−61.32	*2345**6**7***	−6.56	37.05	1.34 ± 0.26	1.10 ± 0.20	
$B5$	−61.74	***2**3**4**56**7***	−6.53	37.05	1.54 ± 0.26	1.17 ± 0.20	
$B6$	−62.16	**1**23*567***	−6.42	37.28	1.43 ± 0.23	0.86 ± 0.18	
$B7$	−62.58	123***5**67***	−6.47	37.14	1.45 ± 0.23	0.92 ± 0.18	
$B8$	−63.00	*2**3***5678**	−6.24	36.98	1.52 ± 0.22	0.68 ± 0.18	
$B9$	−63.42	*23*5**6**78**	−6.15	36.86	1.40 ± 0.22	0.83 ± 0.18	
$B10$	−63.84	**3*56**78***	−6.14	37.02	1.42 ± 0.29	0.63 ± 0.23	
$B11$	−64.26	**3*5678**	−6.10	36.99	1.43 ± 0.29	0.64 ± 0.23	
$B12$	−64.68	**3***5**67***	−6.11	36.98	1.31 ± 0.35	0.88 ± 0.28	
$B13$	−65.10	**3*567***	−6.21	37.06	2.17 ± 0.35	0.64 ± 0.28	
$B14$	−65.52	****56**7***	−3.72	37.33			
	Fearure B group fitting				1.48 ± 0.08	0.89 ± 0.07	$\pi = 0.628 \pm 0.057$
	Feature fitting result				1.89 ± 0.14	0.74 ± 0.21	$\pi = 0.449 \pm 0.069$
	Collective group fitting of spots in features A and B						$\pi = 0.639 \pm 0.033$
$C1$	−59.22	1**23*******	−8.103	33.71			
$C2$	−59.64	**1********	−8.063	33.65			
$C3$	−60.06	1*34****9*	−7.935	33.594			
$C4$	−60.48	***4****9*	−7.568	33.221			
$C5$	−60.90	****5***9*	−6.271	33.644			
$C6$	−61.32	****56789 10	−6.206	33.644			
$C7$	−61.74	****56789 10	−6.291	33.709			
$C8$	−62.16	****5678**9** 10	−6.316	33.714			
$C9$	−62.58	****5678**9** **10**	−6.061	33.509			
$C10$	−63.00	******7**89 10	−6.498	33.529			
$C11$	−63.42	******789 10	−6.493	33.514			
$C12$	−63.84	******789 10	−6.528	33.509			
$C13$	−64.68	*******8**	−6.393	33.251			
	Feature fitting result				1.37 ± 0.19	-0.44 ± 0.15	$\pi = 0.632 \pm 0.077$
D	+14.12	12********	−1213	1563			
E	+2.73	*********10	−1155	1599			
F	−17.91	*******89 10	−1136	1619	0.79 ± 0.12	-2.41 ± 0.14	
G	−61.32	1234******	−8.19	36.35	1.47 ± 0.20	-1.91 ± 0.20	
H	−60.91	****5*78**	−7.19	36.29	0.84 ± 0.22	1.44 ± 0.30	
I	−65.94	****567***	−1.68	36.30	3.46 ± 0.20	-2.02 ± 0.21	
J	−55.43	123*******	−9.36	32.22	2.60 ± 0.18	-6.18 ± 0.20	
K	−56.28	123*5*****	−5.18	26.21	3.77 ± 0.18	-5.61 ± 0.20	
L	−56.70	***4******	−4.38	25.25			
M	−57.54	********9*	−11.14	37.03			
N	−61.32	****5*****	−1.41	30.14			
O	−63.86	*********10	−3.12	29.39			
P	−64.25	****5*****	−5.69	39.10			
Q	−64.70	********9*	−5.06	33.18			
R	−64.70	*********10	−1.67	35.90			
S	−64.70	*********10	−2.16	33.21			

Column (3): Epoch numbers indicate detection, while asterisk represents non-detection. For each epoch the brightest velocity component(s) in features A, B and C are indicated with underlined boldface.

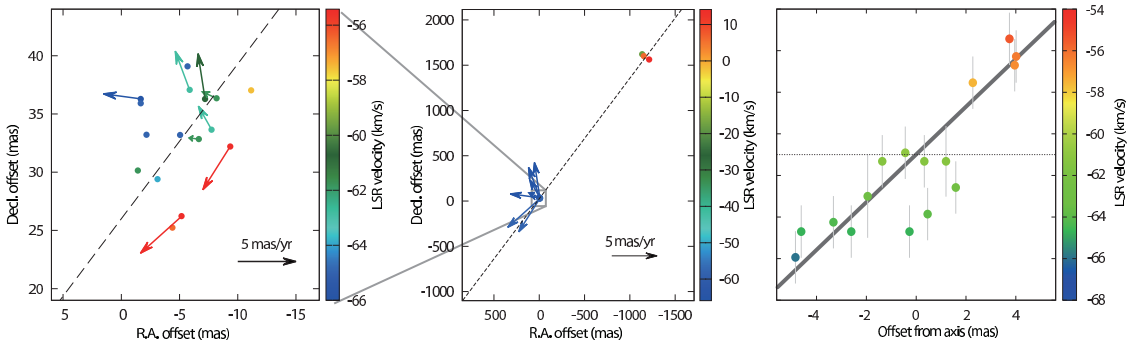

Figure 4.8: Positions and internal motions (corrected for systemic motion) of masers in S235AB-MIR. Coordinates are given respective to the phase tracking center of the maser data. *Middle* shows the full scale maser distributions including the three maser groups discussed in the main text. A short dashed line traces the jet axis. The proper motion of feature F ($v_{LSR} = -17.91$ km s^{-1}) is too small to see. *Left* shows a zoom of the cluster of blue lobe masers. *Right* shows a p-v diagram of the blue lobe masers with respect to the jet axis, where vertical bars are the half-widths of typical maser velocity features, larger bars at offsets of +1 and -2 mas correspond to features A and B, respectively, which have wider velocity profiles. The thick grey line is the least squares fit and traces a gradient of 1.2 km s^{-1} mas^{-1}.

4 epochs and are associated with features A or B. We perform 'group fitting' on masers in features A and B together, and also separately for comparison. 'Feature fitting' is an approach where we determine the nominal position of the entire maser feature by calculating the flux-weighted average position of the three brightest maser spots.

The results of these three fitting procedures are summarised in Table 4.4, where astrometric positions in columns 4 and 5 are quoted as offsets from the phase tracking center of the maser beam which was set to $(\alpha, \delta)_{\rm J2000.0} = (05^{\rm h}40^{\rm m}53^{\rm s}.38445496, +35°41'48".4470)$.

'Individual fitting' was done on 3 masers in feature A. Each maser spot gave consistent parallax and proper motion values. The 'group fitting' of maser spots in feature A gave results that were consistent with the average of the 'individual fitting' results. However, when using 'feature fitting' the same consistency could not be obtained. For thermal sources the flux of each component should be steady, thus the nominal position of the feature should trace the gravitational center. However, feature A exhibits multiple velocity components as can be inferred from column 3 of Table 4.4 (see table footnote) and any changes in the relative brightnesses of components will affect the determination of the nominal astrometric position of the feature. Therefore, regarding feature A, fitting is best done using spots rather than features.

Multiple maser components also exist in feature B as is confirmed by its maser burst nature (*see subsection 4.2*). As such, 'feature fitting' was also inappropriate for feature B. Emission was not detected for a whole year in any one channel barring 'individual fitting', however 'group fitting' for this feature gave a parallax that matched very well to the results for feature A.

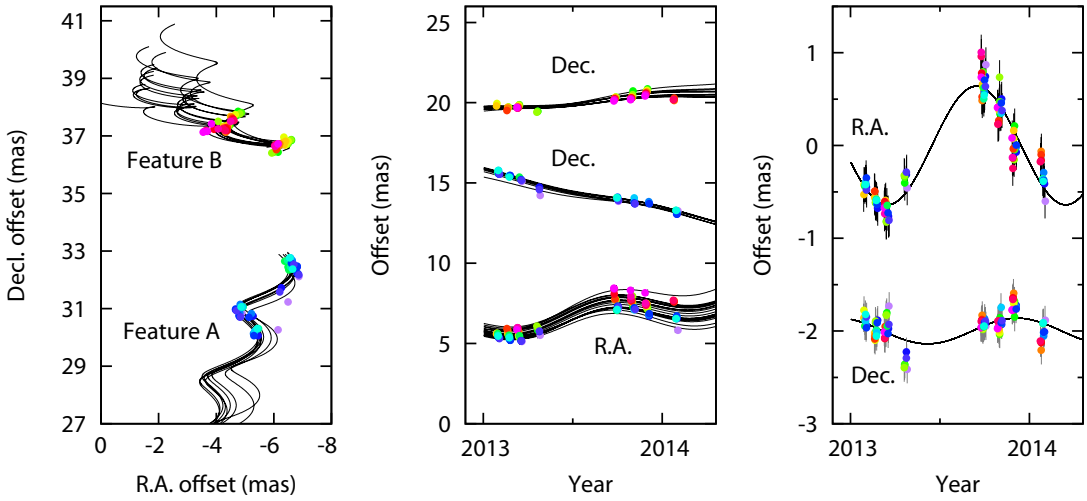

Figure 4.9: Parallax and proper motion fitting of spots (coloured arbitrarily) associated with maser features A and B in S235AB-MIR. *Left*: Sky-plane motions of the maser spots with respect to the phase tracking center. *Middle*: arbitrary scale astrometric offsets in Dec. (above and middle for Features B and A, respectively) and R.A. (below) as a function of time. *Right*: parallactic motion in R.A. (above) and Dec. (below) for all spots in features A and B after subtraction of linear proper motions. Small horizontal offsets (within ±7 days) were introduced to data points in the middle and right-hand plots for readability.

Maser emission in feature C per individual epoch is narrower in velocity than that of features A and B, and does not exhibit multiple velocity peaks or a burst nature. This suggests that feature C has a simpler physical and velocity structure than features A and B. However, feature C is seen to increase in velocity over time (*see subsection 4.5*). As a result, the temporal baseline of emission seen in any one maser channel was too short for astrometry using 'individual fitting' or 'group fitting'. The proper motion of this maser feature was obtained through 'feature fitting', its parallax value was consistent with the aforementioned results from features A and B, however the parallax was not used as it violates the criterion that masers must not be accelerating.

In order to conclude the annual parallax of S235AB-MIR we decided to use 'group fitting' for maser spots in features A and B together. Error floors (*see* Hachisuka et al. 2009) of 0.19 and 0.15 mas were added to RA. and Dec. positions, respectively, in order to achieve a $\chi^2 = 1$ fit. The annual parallax of S235AB-MIR was $\pi = 0.639 \pm 0.033$ mas corresponding to a trigonometric distance of $D = 1.56^{+0.09}_{-0.08}$ kpc, firmly placing it in the Perseus Arm.

The failure of 'feature fitting' for features A and B demonstrates that the type of fitting procedure used can affect parallax estimates, especially in the presence of unresolved structure. Proper motions shown in Table 4.4 are those determined in by group fitting, assuming this common distance. Maser astrometries and their components are shown in Figure 4.9.

4.2.2.3 Internal and systemic motions

The observed proper motions of Galactic masers are a combination of internal motions inherent in the SFR, and the systemic motion of the SFR with respect to the Sun.

Considering Galactic motion, S235AB-MIR resides in the Galactic anticenter direction ($l = 173.7°$), where systemic proper motions are small. Using the Galactic rotation curve from Reid et al. (2014): $\Theta = \Theta_0 - 0.2(R - R_0)$, where $R_0 = 8.34 \pm 0.16$ kpc, $\Theta_0 = 240 \pm 8$ km s^{-1}, and using our distance to S235AB-MIR; 1.56 kpc, we calculate $\Theta = 240$ km s^{-1}. From this, we estimate the proper motion contribution due to Galactic rotation using a formulation from Ando et al. (2011):

$$\mu_l cosb = \frac{1}{a_0 D}\left[\left(\frac{\Theta}{R} - \frac{\Theta_0}{R_0}\right) R_0 cos\ l - \frac{\Theta}{R} D\right]$$

Which gives $\mu_l cosb = -0.019$ mas yr^{-1}. We must also correct for the motion of the Sun with respect to the LSR, which is taken as $(U, V, W)_\odot = (+10.3, +15.3, +7.7)$ km s^{-1} from Ando et al. (2011) (based on Kerr & Lynden-Bell 1986). These contribute an apparent motion of $(\mu_\alpha cos\delta, \mu_\delta) = (+0.27, -2.41)$ mas yr^{-1}. By subtracting this motion from the observed proper motions we isolated the internal motions of water masers in S235AB-MIR which are shown in Figure 4.8.

Alternatively we sought to infer the internal proper motions by use of a reference maser. Feature F has a velocity that is well removed from those of the blue and red lobe masers and instead has a velocity close to that of the molecular core; this feature seems unrelated to the jet. By designating feature F as the reference maser we can separate the internal motions (traced by blue and red lobe masers) from the source systemic motion (traced by feature F).

Feature F has a proper motion of $(\mu_\alpha cos\delta, \mu_\delta) = (+0.79 \pm 0.12, -2.41 \pm 0.14)$ mas yr^{-1} which is almost identical to the correction factor calculated above from the LSR-frame motion. As such both the reference maser approach and LSR-frame approach produce very similar internal motions. In the latter approach the source systemic proper motion would be equivalent to that of feature F; $(\mu_\alpha cos\delta, \mu_\delta) = (+0.79 \pm 0.12, -2.41 \pm 0.14)$ mas yr^{-1}. This value is consistent with other Perseus Arm sources catalogued in Reid et al. (2014).

Resultant internal proper motions are typically smaller than the line of sight velocities and motions do not appear well collimated. This can be explained by projection effects from a pole-on geometry, as was seen in the case of G353.273+0.641 which is also a DBSM jet source (Motogi et al., 2015).

4.2.3 Discussion

4.2.3.1 Driving source: S235AB-MIR

Felli et al. (2006) proposed the *class I* MYSO S235AB-MIR as the progenitor of the molecular outflows and maser emission in this region. Our observations confirm that the blue-shifted and red-shifted velocity components, which are separated by 2", lie either side of S235AB-MIR and in agreement with the corresponding blue and red-shifted lobes of the NNW-SSE molecular outflows seen in HCO^+ (Felli et al., 2004). Less extended blue and red-shifted lobes, also orientated NNW-SSE, are seen in $C^{34}S$. Felli et al. (2006)

consider two possible interpretations of the $C^{34}S$ velocity lobes; a molecular outflow and a rotating disk. Positions, line of sight velocities, and proper motions of water masers presented in this work support the outflow interpretation of Felli et al. (2006), such that the $C^{34}S$ gas is a component of the NNW-SSE outflow. Furthermore, the proper motions of water masers oppose the radio and millimeter source VLA-1/M1 as progenitor of the NNW-SSE outflow, rather supporting the view that the outflows are driven by S235AB-MIR.

The HCO^+ emission has a distinct quadrupole morphology - one bipolar set of lobes orientates to NNW-SSE with the other set almost perpendicular. At the current best resolution the outflows appear concentric. Regarding establishment, one possible explanation is that of a sudden change in the outflow direction of a single bipolar outflow driven by the MYSO in S235AB-MIR, due to an encounter with another cluster member (Bally & Zinnecker, 2005). Another possibility is that of multiple bipolar outflow progenitors in the S235AB-MIR core, at angular sizes finer than those probed in the *Spitzer* images. Considering this scenario, we cannot rule out the possibility that the high velocity water masers in S235AB-MIR are driven by a companion low mass YSO. However, the emission maps of Felli et al. (2004) show that the orientation and velocity structure of the $C^{34}S$ (dense gas tracer) emission correlates with that of the NNW-SSE HCO^+ outflow and water masers (this work), whereas no $C^{34}S$ gas was seen to trace the NE-SW outflow. So, it is reasonable to assume that the former may therefore be energetically dominant and would thus likely be attributed to the MYSO.

4.2.3.2 Maser burst

A sudden increase in maser brightness is known as a 'burst'. Deguchi & Watson (1989) proposed a maser burst model in which an increase in path length, achieved by the overlapping of two masing clouds along the line of sight, can produce an increase of two or more orders of magnitude in observed brightness. Multi-epoch VLBI observations by Shimoikura et al. (2005) found observational evidence of this process in the case of the water masers of Orion KL, however there are few other examples of a maser burst caught 'in the act'. There were 2 strong maser bursts during our VLBI monitoring observations of S235AB-MIR in which fluxes of ∼100 Jy were reached, as shown in Figure 4.10.

Column 3 of Table 4.4 shows the detected velocity components (rows) for each epoch (columns), where the brightest peaks in in each epoch are shown as underlined boldface digits for spots associated with features A, B and C. From the peaks we can see that feature B has a complex velocity structure; velocity drifts and multiple peaks. Two peaks can be seen in epoch 5 (MJD 56564) at -64.68 km s^{-1} and -62.58 km s^{-1} which respectively correspond to the blue and green components seen in Figure 4.11, where feature B is at map offset (0,0). In epoch 6 (34 days later) the total flux of feature B raised from 7 Jy to 80 Jy as the two components overlapped both in space and velocity. Therefore we observe that the bursting mechanism in the masers of S235AB-MIR (Felli et al., 2007) is the same as that which was seen in Shimoikura et al. (2005). Figure 4.11 illustrates the 'pre-burst' stage of this mechanism.

Bursting activity was also seen in feature B at epoch 3 in which it reached a flux of 120 Jy. The bursting mechanism in epoch 3 was the same as described above.

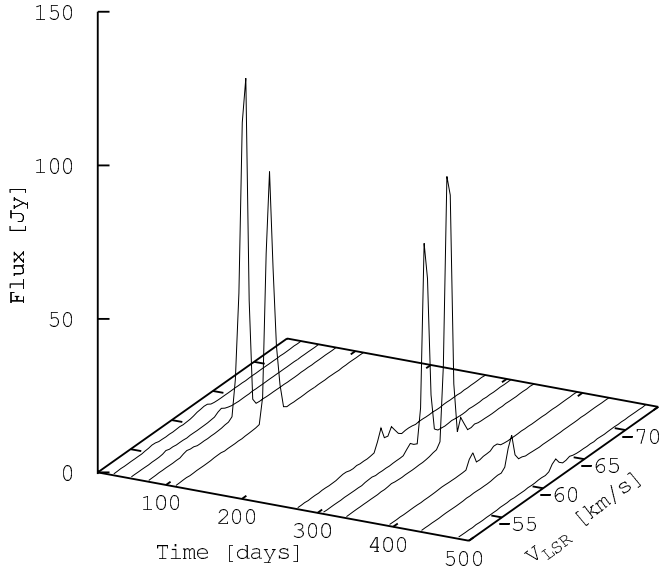

Figure 4.10: Scalar averaged spectra of the blue lobe H_2O emission at full scale, highlighting the variable burst nature.

Feature A also has a complex velocity structure. In this case feature A appears as a single peaked maser feature in epoch 1, which gradually separates in velocity into two defined peaks by epoch 3, and then recombines at epoch 5 - where a modest maser burst raised its flux to 20 Jy from its usual flux of 2∼3 Jy.

The peak velocities of the overlapping maser components involved in the burst often differed by a few km s^{-1}, i.e. the burst occurred at the intermittent velocity between the peaks. This suggests the existence of a significant amount of population inverted gas at velocities away from the original peaks. Such behaviour indicates that the physical maser cloud may have a spatially unresolved structure and possibly some internal motions since the bursting components were part of the same maser feature. Such scales cannot be investigated directly at the current angular resolution of terrestrial VLBI arrays, however the presence of such substructures has recently been observed in the results of space VLBI observations (RadioAstron newsletter: #19 - released 6th March 2013, and #27 - released 31st March 2015).

4.2.3.3 H_2O masers: the jet and the velocity gradient

H_2O masers can be collisionally excited on the surface of shock fronts created when a protostellar jet pushes into ambient gas (*ex: conical jet surface* Moscadelli et al. 2000, U-*shaped 'micro-jet'* Furuya et al. 2000). The large velocity difference in blue (−66 km s^{-1}) and red lobe (+14 km s^{-1}) masers in S235AB-MIR indicate that these masers are likely tracing a jet. Elongated red masers parallel to the jet axis, shown in Figure 4.11, may represent shocked gas on the inner surface of the jet.

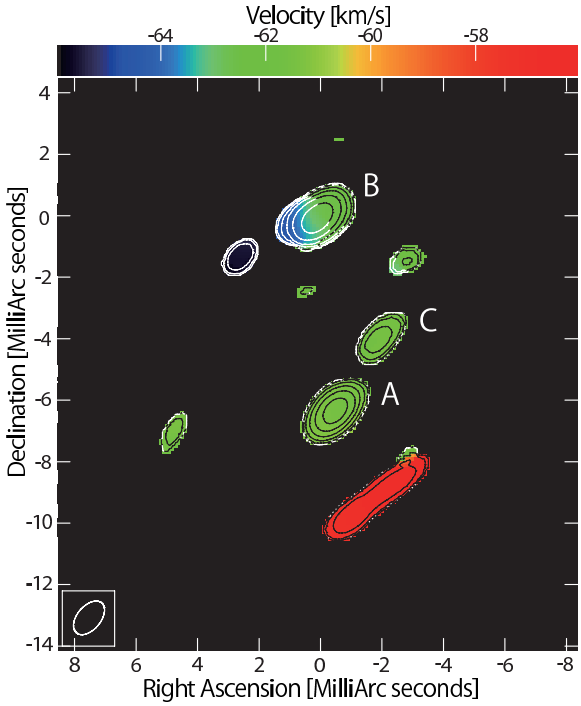

Figure 4.11: First moment (velocity) map of water maser emission in epoch 5 (MJD 56564) where positions are relative to the reference maser in feature B. The three main features are labelled. Two velocity components in feature B, at map position (0,0), are the progenitors to the maser burst seen in epoch 6 (reaching 80 Jy). Contours are 3, 5, 10, 20, 40, 80 times the image rms noise of 200 mJy.

The jet axis determined by H_2O masers in Figure 4.8 is in good agreement with the orientations of large scale HCO^+ and smaller scale $C^{34}S$ outflows from Felli et al. (2004). We made a p-v diagram using offsets from the jet axis plotted against line-of-sight velocity in the right-hand panel of Figure 4.8. Maser features are well fit to a straight line as would be expected from solid body rotation. Its gradient of 1.2 km s^{-1} mas^{-1} corresponds to 0.77 km s^{-1} au^{-1} at 1.56 kpc.

Velocity gradients across jet axes have been reported in several YSO observations and simulations (Zapata et al., 2010, 2015; Coffey et al., 2004; Woitas et al., 2005; Bacciotti et al., 2002; Cerqueira et al., 2006). To explain these velocity structures there is current debate between supporters of the jet rotation interpretation (Zapata et al., 2010, 2015; Coffey et al., 2004; Woitas et al., 2005; Bacciotti et al., 2002) and those who propose alternative explanations (Soker, 2005; Cerqueira et al., 2006). Although we believe S235AB-MIR possibly evidences a rotating jet we consider other commonly suggested explanations of velocity gradients in jets, before discussing a model of jet rotation.

4.2.3.4 Interpreting the velocity gradient

Precessing jets are occasionally found in MYSOs (Caratti o Garatti et al., 2015). In this scenario the jet is comprised of a continuous ballistic ejection whose direction is time-dependent, causing the well-known 'wiggle' morphology. Cerqueira et al. (2006) show that the velocity field created by a precessing jet and a rotating jet are difficult to distinguish in radial velocity profiles of emission line observations. Such conclusions are based on large scale gas motions encompassed within the precession angle; scales larger than the radius of the jet. The H_2O masers in S235AB-MIR trace scales comparable to the physical radius of the jet ($\sim$20 au, Furuya et al. 2000; Coffey et al. 2004). A velocity gradient on a jet radius scale can only be formed if there is motion within the jet itself - thus rejecting a precession scenario.

Velocity structures may also arise from dispersion at the tip of a jet driven bow shock. In this scenario the shocked gas at the tip of the jet is forced edgeways as it decelerates into ambient material. Lee et al. (2000) modelled jet-driven bow shocks and found their p-v diagrams to be symmetric across the central axis (their Figure 26). This contrasts with the p-v diagram of water masers in S235AB-MIR which is distinctly asymmetric (Figure 4.8). Furthermore, radial velocity gradients seen in the bow shocks of Lee et al. (2000) are several orders of magnitude lower than that observed in S235AB-MIR (roughly 2×10^{-3} km s^{-1} au^{-1} for the case of HH 111 in their Figure 27). The bow shock interpretation is therefore inconsistent with the velocity gradient seen in S235AB-MIR

If masers were produced in the shock front of an expanding arc it would be possible to reproduce a velocity gradient across the direction of collective motion if the arc were flattened on a plane, inclined to the observer and fanning out at constant velocity from a common driving source. However a fanned out jet scenario is a strictly ballistic model, requiring the proper motions of maser features to interpolate to a common kinematic center. In contrast, blue lobe masers in S235AB-MIR form a cluster, as opposed to an arc, and proper motions do not interpolate; some of the maser features in S235AB-MIR have proper motions that are parallel to the jet axis while some are near perpendicular to it - which is difficult to explain by purely ballistic motion.

We also note that blue lobe masers have been known since Henkel et al. (1986) yet the maser group remains compact despite differences in line of sight velocities and divergent proper motions. This is difficult to reconcile using ballistic arguments since masers would be expected to have dispersed more by the present day.

Since only a modest number of maser features were detected in S235AB-MIR we cannot fully dismiss all ballistic interpretations of the observed velocity gradient using the current data alone and require confirmation from observations that sample jet gas directly. Nevertheless, without a satisfactory ballistic explanation for the kinematics of water masers in S235AB-MIR we proceed with a rotating jet as our working hypotheses. As we will see, a rotating jet interpretation forms consistencies with the aforementioned arguments that had conflicted with ballistic explanations. To our present knowledge S235AB-MIR is the first candidate rotating jet traced by water masers and, if confirmed with further observations, presents an ideal laboratory to study magnetocentrifugal jets in a *class I* YSO with an accurate distance.

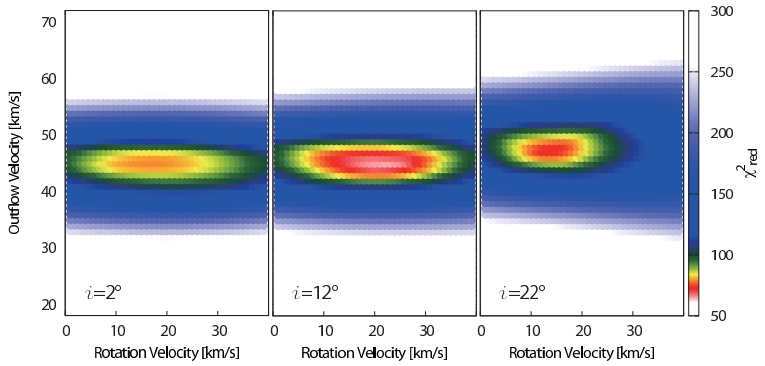

Figure 4.12: Plots of $\chi^2_{\rm red}$ for fitting parameters at inclination slices of $i = 2, 12, 22°$ using model fitting condition 1.

We created a kinematic model of a rotating cylinder to compare with the sky-plane distributions and 3D (sky-plane and line of sight) velocities of the water masers in S235AB-MIR. A cylindrical surface model was chosen for its analogy to an interface between a jet and the ambient gas - where masers are excited. Also the choice of a cylinder over a conical surface circumvents the ambiguity of the driving source position (which should not matter since jets are able to de-collimate and re-collimate). The fixed physical parameters of the model were the jet position angle, PA, and radius, r, which were readily determined from the maser maps (Figure 4.8) as $PA = 217°$, $r = 7.5$ au. The free parameters were the linear jet velocity, $v_{\rm out}$, the tangential rotation velocity, $v_{\rm rot}$, and the inclination to the line of sight, i. For comparison with observational data the modelled 3D motions were projected into the sky-plane and line of sight.

Modelled values were compared with the maser data with regards to: positional offset from the jet axis, line-of-sight velocity with respect to the parent cloud (-17 km s^{-1}) and, when present, R.A and Dec. internal proper motions. We employed a 'reduced χ^2' fitting approach in which $\chi^2_{\rm red} = \chi^2/N$, where N is the number of degrees of freedom, evaluated as $N = \textit{number of data points} - \textit{number of fitted parameters} - 1$. Variables that produce the lowest $\chi^2_{\rm red}$ correspond to the best match between model and data. For a check of consistency and to investigate the effects of varying degrees of freedom on $\chi^2_{\rm red}$ we considered 3 different conditions when modelling data, which were - to use data from: 1) all maser features. 2) only masers features with measured proper motions. 3) only maser features without measured proper motions (only position and line of sight velocities).

The resulting parameters were:
1) $v_{\rm out} = 45$ km s^{-1}, $v_{\rm rot} = 22$ km s^{-1}, $i = 12°$: $\chi^2_{\rm red} = 65$,
2) $v_{\rm out} = 45$ km s^{-1}, $v_{\rm rot} = 19$ km s^{-1}, $i = 10°$: $\chi^2_{\rm red} = 55$,
3) $v_{\rm out} = 45$ km s^{-1}, $v_{\rm rot} = 28$ km s^{-1}, $i = 10°$: $\chi^2_{\rm red} = 9$.

All fitting conditions generally agree on a high outflow velocity and a shallow inclination angle, with the most deviation seen in determination of the rotation velocity. We adopt $v_{\rm out} = 45$ km s^{-1}, $v_{\rm rot} = 22$ km s^{-1}, $i = 12°$ from condition 1 results since the fit used all data.

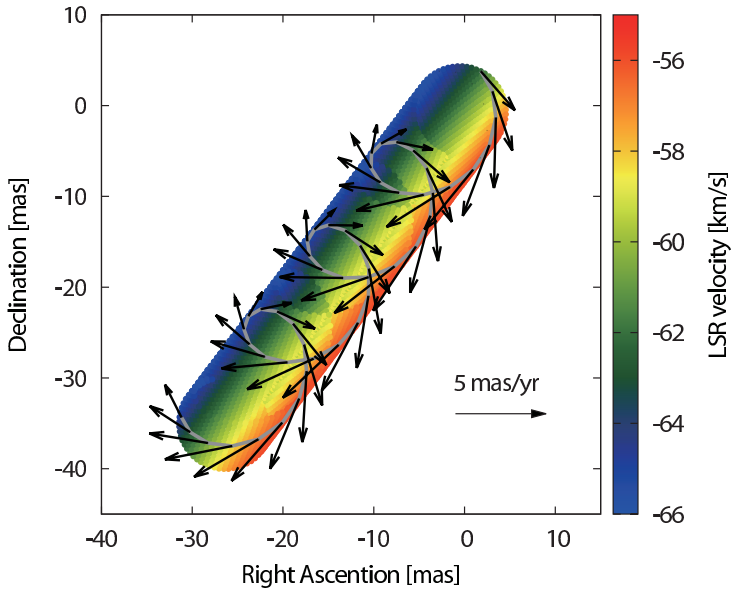

Figure 4.13: Rotating cylinder model produced by the best fitting parameters. The grey line illustrates a test particle trajectory in which vectors show the direction and magnitude of proper motions and colour indicates the line of sight velocity.

Values of $\chi^2_{\rm red}$ for parameters using condition 1 are shown in Figure 4.12 where the 3D $(v_{\rm out}, v_{\rm rot}, i)$ distribution of values is represented in 'slices' at inclination angles of $i = 2, 12, 22°$. Modelled and observed maser distributions and proper motions are well matched (Figures 4.8 & 4.13) with the redder masers having larger proper motions in a more southernly direction and vice versa. Additionally the p-v diagram produced by the model shows good agreement with the p-v diagram drawn using the maser data (Figure 4.14).

4.2.3.5 Overview of jet parameters

To evaluate the success of the model fitting we calculated the scalar sum of 3D motions in the fitting residuals and compared this to the the scalar sum of 3D motions in the data. We find that the model can account for 80% of observed motions, with 20% remaining as residuals, which we adopt as the total model error. The relative fitting success of each individual parameter ($v_{\rm out}$, $v_{\rm rot}$ and i) can be determined by the '3D' shape of the $\chi^2_{\rm red}$ locus in Figure 4.12. In our fitting iterations $\chi^2_{\rm red}$ increases by 50% its minimum value within $\Delta v_{\rm out} = \pm 4$, $\Delta v_{\rm rot} = \pm 16$ and $\Delta i = \pm 12$, corresponding to expected error contribution ratios of $(\epsilon^2_{v_{\rm out}}{:}\epsilon^2_{v_{\rm rot}}{:}\epsilon^2_i) = (1^2{:}4^2{:}3^2)$. The total model error can be separated into relative contributors, which allows us to assign error values to our best-fit model parameters, which become $v_{\rm out} = 45 \pm 2$ km s^{-1}, $v_{\rm rot} = 22 \pm 3$ km s^{-1}, $i = 12 \pm 2°$.

Our modelled rotation velocity of $v_{\rm rot} = 22 \pm 3$ km s^{-1} agrees well with those measured by Coffey et al. (2004) and Woitas et al. (2005) on similar scales. The jet velocity gradient is linear and steep, at 1.2 km s^{-1} mas^{-1} which corresponds to 0.77 km s^{-1} au^{-1} at a

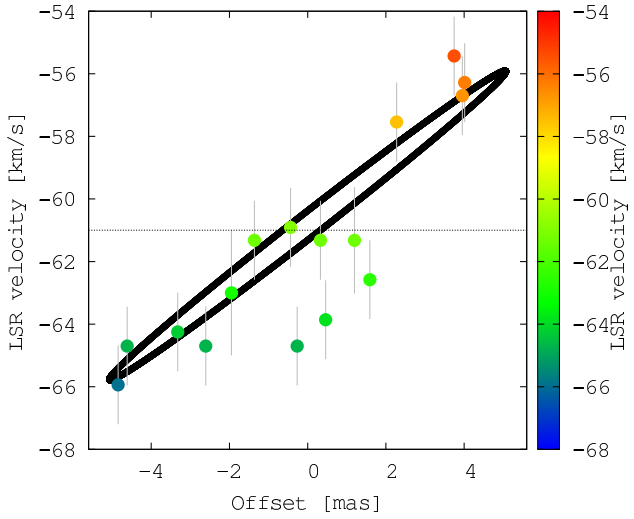

Figure 4.14: Position-velocity diagram for maser features associated with the blue lobe of the jet where offsets are measured from the jet axis (from Figure 4.8). Also shown is the position-velocity profile produced by our rotating cylinder model (*solid line*). The horizontal line at -61 km s^{-1} indicates the median velocity of the blue lobe masers.

distance of 1.56 kpc. The very steep gradient is consistent with the trend seen in Zapata et al. (2010) for velocity gradients to steepen at radii closer to the jet.

The outflow velocity component of the jet is comparable with those frequently reported in the literature and the inclination angle is typical for a DBSM source, which are also known to be jet driven (Caswell & Phillips, 2008; Motogi et al., 2013, 2015). Regarding the age of the jet, if we take a symmetric case where the star stands between the red and blue lobes the jet length would be $r_\star$ = projected distance/ sin $i = 1.5 \times 10^4$ au, using $D = 1.56$ kpc. Therefore the approximate dynamical age of the maser jet is $t_{\rm jet} = r_\star / v_{\rm out} = 1600$ *years*, assuming constant velocity. This value will vary between $0 < t_{\rm jet} < (2 \times 1600)$ years depending on the position of the star. Note that this is not an estimate of the YSO age, which is ~ 4000 years (Dewangan & Anandarao, 2011).

The low uncertainty seen in $v_{\rm out}$ is echoed by the consistency in the determination of $v_{\rm out}$ using fitting conditions 1, 2 and 3. This indicates that LSR velocity information dominates the determination of the outflow velocity. Larger uncertainty is seen in $v_{\rm rot}$ this parameter also shows less consistency when comparing the fitting conditions indicating that internal motions are important for characterising rotation. In the case that a better estimate for the systemic motion of the source becomes known we may refine the model of water masers in S235AB-MIR using more accurate corrections to internal motions.

Although ambiguities may remain in our model due to the small number of detected H_2O masers, it is important to note that *all* models for all combinations of parameters and fitting conditions produce results that favour rotation in some way, *consistently rejecting a ballistic-only interpretation.*

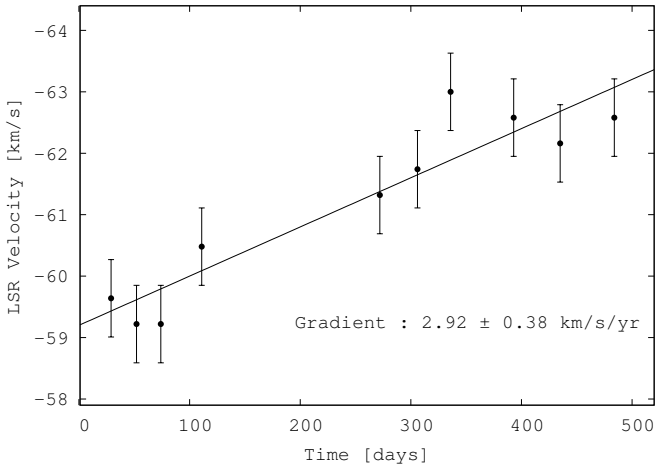

Figure 4.15: Peak LSR velocity of feature C as a function of time, showing acceleration to bluer velocities.

Evidence supporting the presence of a rotating jet is itself important as it promotes magnetocentrifugal jet motions as a viable mechanism for removing angular momentum from an accreting system. We do not quantify this angular momentum using our VLBI data because maser emission does not scale with mass. Masers have no net charge and thus their bulk motions are not directly influenced by magnetic fields. We propose that H_2O masers in S235AB-MIR are likely entrained in - and trace the kinematics of - a rotating jet of molecular gas. As such, we intend to revisit S235AB-MIR using millimeter array observations of jet tracers, which should provide suitable quantification of the angular momentum carried in the jet.

4.2.3.6 Accelerating maser

A stable velocity increase was observed in feature C, which was the only maser feature to exhibit such behaviour. We derived a velocity drift rate of 2.92 ± 0.38 km s^{-1} yr^{-1}, where the error value is the standard deviation of a linear fit to the data (Figure 4.15).

We introduced an additional error term of ± 0.63 km s^{-1} corresponding to the half-width of a typical maser spectral peak (these are the error bars in Figure 4.15) to account for the possibility that changes in velocity were misinterpreted from the changing in dominance of different velocity components in a maser feature. Subsequently the measured acceleration of feature C is 2.92 ± 1.01 km s^{-1} yr^{-1}.

Circular motions give rise to acceleration toward the axis of rotation therefore the appearance of an accelerating maser is a reasonable finding given the context. The measured acceleration is consistent with the model prediction, within the estimated uncertainty, which supports rotation as a possible origin and lends further support to the rotating jet interpretation of the velocity gradient in S235AB-MIR.

The velocity drift rate seen here is similar to that of DBSM maser source G353.273+0.641 (Motogi et al., 2015). In their case, slower masers near to the driving source are accelerated up to the outflow velocity (120 km s^{-1}), thus the masers appear to trace launching motions at the root of the jet. In our case, however, the masers seem to be well removed from the driving source, supporting an alternative explanation.

Felli et al. (2006) also observed a velocity drift in the water masers of S235AB using the single-dish Medicina radio telescope. They find two maser features in the −5 to 10 km s^{-1} range which exhibit accelerations of $\sim$ 1 km s^{-1} yr^{-1}. The velocity range creates a near overlap between the core velocity and red lobe masers discussed in this work. Felli et al. (2006) speculate that the velocity drift may have been due to the acceleration of masers from the central YSO up to faster redshift velocities (as seen in Motogi et al. 2015). This is certainly feasible given the spatial consistency of these maser groups as seen in our VLBI images. Unfortunately these masers were rarely detected in our observations due to their weak emission. This possible maser outflow event would make an excellent target for VLBI observations at higher sensitivity.

4.2.4 Conclusions

Using VLBI monitoring observations we measured the astrometries of H_2O masers in S235AB-MIR. Our annual parallax of $\pi = 0.63 \pm 0.03$ mas corresponds to a distance of $D = 1.56^{+0.09}_{-0.08}$ kpc, placing the source in the Perseus Arm. The source systemic motion was $(\mu_\alpha cos\delta, \mu_\delta) = (+0.79 \pm 0.12, -2.41 \pm 0.14)$ mas yr^{-1}.

The S235AB-MIR molecular core drives a maser jet however it is unclear if the core contains a single MYSO or if it also houses companion lower mass YSOs. As such, the identification of the jet progenitor remains pivotal and dictates the significance of the VLBI maser data.

We present evidence that the H_2O maser burst behaviour in S235AB-MIR is caused by the overlapping of maser components along the line of sight, as was seen by Shimoikura et al. (2005) in Orion KL, and propose that sub-feature scale structures exist which are not fully resolved at our current angular resolution.

Masers trace a young ($\sim$ 1600 years) jet which is aligned to outflows seen in HCO^+ and $C^{34}S$. The maser jet has a position angle of $PA = 217°$, a diameter of 15 au, and exhibits a well defined velocity gradient across its axis of 1.2 km s^{-1} mas^{-1}, corresponding to 0.77 km s^{-1} au^{-1} at a distance of 1.56 kpc.

3D motions, derived from line-of-sight and sky-plane velocities of 16 water maser features are well described by a rotating cylinder model, giving the water maser jet a manner comparable to a 'water spout'. Our best-fit model parameters were $v_{out} = 45 \pm 2$ km s^{-1}, $v_{rot} = 22 \pm 3$ km s^{-1}, $i = 12 \pm 2°$, which are the outflow velocity, tangential rotation velocity and line-of-sight inclination, respectively. Our parameters are consistent with other investigations of jet rotation at similar scales. These new observations support magnetocentrifugal jet rotation as a possible mechanism of dispersing angular momentum from the protostellar disks of accreting massive stars.

One maser feature was found to accelerate steadily at a rate of 2.92 ± 1.01 km s^{-1} yr^{-1}, which was consistent with that predicted in our rotating jet model. The velocity drift rate is similar to that seen in another DBSM source although likely different in origin.

5

Galactic Structure and Kinematics

To discuss the structure of the Galaxy I will bring together data from all of my parallax results (IRAS20056, IRAS20143, S235AB-MIR, IC2162) to update the current map of the Milky Way Galaxy, which has been compiled from VLBI distance measurements. I will introduce the Galactic constants, which are a set of parameters that describe the size and rotation of the Galaxy. Here I will discuss the history of the Galactic constants and the various ways in which they were measured or estimated. Finally, using VLBI results from star forming regions on the solar circle and tangent points (regions of special geometry in our Galax) I will discuss estimation of Ω_0, a parameter which describes the angular rotation of material near the Sun about the Galactic center.

5.1 IRAS 20143+3350: Tangent point

The Galactic circular rotation velocity evaluated at the position of the Sun, Θ_0, and the Galactocentric distance to the Sun, R_0, are two of the fundamental parameters used in discussing the structure and kinematics of the Milky Way. These parameters are central to estimating the kinetic distance of Galactic sources, thus influencing estimations of their physical properties. Furthermore, these parameters affect the shape of the Galactic rotation curve which has long been an essential tool for evaluating the dynamical mass distribution in the Milky Way.

The International Astronomical Union (IAU) recommends values of $R_0 = 8.5$ kpc and $\Theta_0 = 220$ km s^{-1} for the Galactocentric distance of the Sun, and Galactic circular velocity of the LSR (Kerr & Lynden-Bell, 1986). However a growing number of astrometric observations utilising very long baseline interferometer (VLBI) suggest the need to revise these values (Reid et al. (2009); Honma et al. (2012) *and references therein*), further stressing the importance of VLBI astrometry in our understanding of the Milky Way. It is possible to estimate Θ_0 and R_0, hereby referred to as the Galactic constants, by measuring the distance and motion of many sources in the disk of the Milky Way, with respect to the local standard of rest (LSR). Historically, they have been derived from global sinusoidal patterns shown in the proper motions and radial velocities of nearby stars (Oort, 1927). However, this method is based on the assumption that the systematic motion of the Solar neighbourhood does not deviate from Galactic circular motion. To circumvent this problem we must extend the sampling region to beyond the

optical observable range, which is limited by interstellar extinction. VLBI astrometry is a viable approach since radio observations do not suffer from interstellar extinction.

There are two approaches to estimating the Galactic constants. One method uses a sample of sources widely distributed on the Galactic disk. With a kinematic model of the Galaxy, multi-parameter fitting determines the Galactic constants. Although this approach has the advantage of statistically reducing the random motion inherent in the source sample by increasing the number of sources, the reliability of this method is undermined by the high number of variable parameters that are simultaneously solved for. The other approach focuses on sources at special locations where the Galactic constants can be derived with a lower dependancy on the model of Galactic kinematics. Two such locations are positions on the Solar circle and at the tangent point, defined as the position closest to the Galactic center on the assigned line of sight. Astrometric observations of a source near these locations can give the ratio of the constants, $\Omega_0 = \Theta_0/R_0$, with appropriate accuracy even if we do not know the exact location of the source (Nagayama et al., 2011; Ando et al., 2011).

IRAS 20143+3634 is an intermediate to high mass star forming region (SFR), as shown in this paper. Furthermore, IRAS 20143+3634 resides near the tangent point in the Cygnus direction. A source at the tangent point, with negligibly small deviation from the Galactic circular motion, moves only along the line of sight to the Sun. Thus we can infer that any lateral proper motion observed on the sky reflects only the Galactic rotation of the LSR, which leads to a simplified estimation of Θ_0, independent of the shape of the rotation curve. In this work, our aim was to use the astrometry of H_2O masers in IRAS 20143+3634 to measure its trigonometric distance and motion in the Galactic plane. Using these results, and those of other sources at the tangent points and Solar circle, we investigated the Galactic constants with fewer assumptions on Galactic structure and kinematics. This simplified approach may be considered more robust than the multi-parameter fitting method. IRAS 20143+3634 is an infrared source listed in the IRAS point source catalogue (Beichman et al., 1988), undergoing intermediate to high mass star formation. This source exhibits a highly compact core, seen in CS($J = 2 - 1$) observations (Ao et al., 2004), and wide velocity wings in ^{12}CO($J = 1 - 0$) indicative of the presence of outflows (Yang et al., 2002).

Disentangling the proper and parallactic motions of masers requires precise astrometric observations. Such precision is available through VLBI maser monitoring using VLBI Exploration of Radio Astronomy (VERA) (Kobayashi et al., 2003). All astrometric observations used in this paper were obtained by positionally referencing 22 GHz H_2O masers with respect to a well defined quasar position, which gives the source position in six dimensional phase-space. The first detection of H_2O maser emission in IRAS 20143+3634 was made by Sunada et al. (2007). In this paper we present the first VLBI observations of the annual parallax and proper motions of H_2O masers in IRAS 20143+3634. Using these measurements we measured the distance of IRAS 20143+3634 from the Sun and evaluated the Galactic constants.

This paper continues as follows: Observations and data reduction are discussed in §2. Results are reported in §3, including the methods used to evaluate the parallactic, internal and systemic motions of masers, and motion of the driving source. In §4 we re-evaluate the physical parameters of IRAS20143+3634 from archive data, using our

Table 5.1: Summary of observations made with VERA.

Observation Epoch	Date	Modified Julian Date	Synthesised beam mas × mas, PA	Detected spots
1	2008 Dec 11	54811	1.3×0.7, −51°	2
2	2009 Feb 10	54872	1.3×0.8, −56°	8
3	2009 May 29	54980	1.3×0.7, −58°	12
4	2009 Sep 26	55100	1.2×0.9, −44°	6
5	2009 Dec 14	55179	1.3×0.8, −45°	9
6	2010 May 26	55345	1.4×0.8, −30°	11
7	2010 Oct 17	55486	1.3×0.9, −41°	11
8	2010 Dec 26	55556	1.2×0.7, −42°	8

new distance estimate. We then discuss in detail the evaluation of Ω_0, the ratio of the Galactic constants, for a variety of methods and sources. Finally, we make comparisons between the observationally determined values of Ω_0, and that which is derived from the ratio of the IAU recommended Galactic constants. Conclusions made in this paper are summarised in §5.

5.1.1 Observations and data reduction

We observed H_2O maser emission in IRAS 20143+3634 over a period of about two years with a total of 11 observation epochs using VERA. We adopted a rest frequency of 22.235080 GHz for the H_2O(6-5) maser line. The phase tracking center of the source was set to $(\alpha, \delta)_{J2000.0} = (20^h16^m13^s.3617, +36°43'33".920)$. Using the dual-beam system installed on VERA we simultaneously observed J2015+3710, which is listed in the VLBA Calibrator Source List (Fomalont et al., 2003), as a positional reference. The typical on-source integration time for each source was about 3 hours per epoch. The exact position of the reference source J2015+3710 was assumed to be $(\alpha, \delta)_{J2000.0} = (20^h15^m28^s.729794, +37°10'59".51480)$. A typical flux of ∼1 Jy was recorded for the reference source during the period of our observations. The angular separation of IRAS 20143+3634 and J2015+3710 was 0.°48.

Intermittent observations of the bright continuum sources NRAO530 and BL Lac were made every ∼1.5 hours to provide bandpass and group delay calibration. An artificial noise signal was injected into both the target and positional reference source beams to continuously correct the instrumental phase difference (Honma et al., 2008b). The total duration of a typical observation epoch was about 7-8 hours.

Left-handed circular polarisation signals were sampled with 2-bit quantisation, and filtered with the VERA digital filter unit (Iguchi et al., 2005). The 256 MHz total bandwidth of the recording system was divided into 16 intermediate frequency (IF) channels, with a bandwidth of 16 MHz each. One IF channel was allocated to the maser source while the remaining 15 IF channels were assigned to the reference source beam.

Interferometric correlation was processed using the Mitaka FX correlator (Chikada et al., 1991). The frequency resolution for the H_2O maser line was set to 31.25 kHz,

corresponding to a velocity resolution of 0.42 km s^{-1}. Since the a-priori delay model applied during correlation processing at the Mitaka FX correlator was not accurate enough for precise astrometry, the visibility phase was calibrated using a more accurate delay model based on recent results obtained in the analysis of geodynamics. In this model, fluctuations in the visibility phase caused by the atmosphere are calibrated based on GPS measurements of the atmospheric zenith delay due to tropospheric water vapour (Honma et al., 2008a).

Data reduction was carried out using the Astronomical Image Processing System (AIPS) developed by the National Radio Astronomy Observatory (NRAO). In the primary stage of data reduction we performed a normalisation of the auto-correlated visibility data taken at each station using the AIPS task ACCOR. Amplitudes were converted into system noise equivalent flux density in 'Jy' using the gain and system temperatures recorded at each station using the task APCAL. Doppler shifts of the maser emission due to the rotation of the Earth were corrected at each antenna station using CVEL. The fringe fitting of the reference source was performed by the task FRING. The positional reference source was self-calibrated by iterating the task pair IMAGR and CALIB. The final phase residual solutions were applied to the IRAS 20143+3634 data, appointing the positional reference source as the phase reference.

Using the calibrated data, maps were made for each velocity channel that showed emission by deconvolution of the modelled emission and beam pattern using the CLEAN procedure based on Högbom (1974). Finally the absolute peak position of each maser spot was determined using Gaussian fits applied to the CLEANed maser images, adopting a signal-to-noise ratio of 7 as our cut-off. Data of sufficient quality were collected on 8 epochs, the detections are summarised in Table 5.3 alongside the typical synthesised beam sizes.

5.1.2 Results

5.1.2.1 Distribution of H_2O masers in IRAS 20143+3634

The scalar averaged cross-power spectra displaying the LSR velocity distribution of H_2O masers is shown in Fig. 5.8. Maser spots were detected within an LSR velocity range of -10 km s^{-1} to $+6$ km s^{-1} with the most persistent emission appearing in the -2.3 to $+1$ km s^{-1} range. If maser emission was seen to persist continuously over three consecutive velocity channels, and also occupied the same region of space within 1×1 mas, those maser spots were considered to be one 'maser feature'. Using this criterion we identified 8 maser features from the 19 maser spots detected in our observations. A summary of detections and velocities of maser features and individual spots is given in Table 5.4. The spatial distribution of detected H_2O maser features is shown in Fig. 5.10 with vectors indicating the velocities and directions of those maser features for which proper motions were determinable (*see section 3.2*). The averaged LSR velocity of maser features is about -1 km s^{-1}, which is similar to the LSR velocity of the driving source, as indicated by thermal molecular line observations (Yang et al., 2002; Ao et al., 2004; Sunada et al., 2007).

Features 1 and 2 differ more than 4.5 km s^{-1} in radial velocity, and have a separation of over 300 mas (∼800AU) from the other maser features. This separation does not exclude them from being a part of the same star forming region, however, due to their

absence for the majority of the observing programme, we will not further discuss their nature in this paper.

5.1.2.2 Proper motion and parallax fitting

Astrometric maser motions are caused by a combination of periodical offsets due to annual parallax motion, a common proper motion observed for all maser spots caused by the systemic motion of the source with respect to the observer, and internal proper motions inherent to the source caused by phenomena such as expansions or outflows. By tracking the absolute positions of maser features for a period of over two years we successfully disentangled and evaluated the contributions of parallax and proper motions.

Simultaneous parallax and absolute proper motion fitting was done utilising two methods, which were then compared for consistency. Fitting was initially performed for all masers that were detected in at least 4 epochs by assuming that all maser spots are located at the same distance and each spot moves on the sky with a constant velocity. In this paper we call this approach "group fitting". Using group fitting we measured an annual parallax of $\pi = 0.367 \pm 0.037$ mas, corresponding to a trigonometric parallactic distance of $D = 2.72^{+0.31}_{-0.25}$ kpc.

For comparison, simultaneous parallax and proper motion fitting was performed for 5 individual maser spots that satisfied the criterion of having been detectable for a year or longer. The results are shown in column 7 of Table 5.4. The trigonometric parallaxes obtained were in the range of $\pi = 0.252$ to 0.430 mas, which agrees well with the value obtained through group fitting. Fitting was also done for maser spots that were detected in at least 3 epochs however their duration of less than a year makes them unreliable for estimating parallax, therefore only the information of their proper motions were estimated, using the parallax information from group fitting.

Fig. 5.11 shows the resulting fits to the data as offsets in right ascension (R.A.) and declination (Decl.) over the course of our observations. The derived parallaxes and proper motions of individual spots are summarised in Table 5.4 alongside the result obtained from group fitting.

Our trigonometric parallactic distance is almost a half of the kinematic distance estimates previously reported; 4.4 kpc by Sunada et al. (2007) from the peak velocity of NH_3 lines, and 4.63 kpc by Yang et al. (2002) using the velocity of CO lines. We should note that this large discrepancy is not due to a large source peculiar motion (see section 3.4). It is mainly due to the small velocity gradient against the distance of the Galactic rotation model, which means IRAS 20143+3634 is located where the error of kinetic distance is large. With Galactic coordinates (l, b)=(74°.57, +0°.85), our distance estimation indicates that IRAS 20143+3634 resides in the Local arm. It is in the proximity of the tangent point in this direction, based on a Galactocentric distance of the Sun of between 8 and 8.5 kpc (Fig. 5.9, *and see section 4.2*).

Table 5.2: H_2O maser detections, parallax and proper motions for IRAS20143+3634.

Spot ID.	Feature ID.	V_{LSR} (km s^{-1})	Detected epochs	$\Delta\alpha \cos\delta$ (mas)	$\Delta\delta$ (mas)	π (mas)	$\mu_\alpha \cos\delta$ (mas yr^{-1})	μ_δ (mas yr^{-1})
A	1	−9.47	*****67*	−225.13	−274.67			
B	2	6.53	**3*****	−169.82	−250.17			
C	2	5.68	*23*****	−169.81	−250.12			
D	2	6.10	*23*****	−169.74	−250.19			
E	3	−1.47	***45***	−29.10	16.25			
F	3	−1.05	*2345***	−28.91	16.73		-3.50 ± 0.25	-2.90 ± 0.57
G	3	−0.63	***45***	−28.91	16.25			
H	3	−0.63	*23*****	−27.87	15.81			
I	4	−1.89	****5678	−24.60	11.12	0.343 ± 0.094	-3.03 ± 0.19	-4.78 ± 0.46
J	5	−1.05	*****678	−22.02	16.58		-2.35 ± 0.38	-5.31 ± 0.87
K	5	−1.47	*****678	−21.86	16.64		-2.50 ± 0.38	-5.32 ± 0.87
L	5	−2.31	****567*	−21.14	15.94		-3.26 ± 0.26	-4.45 ± 0.61
	Feature 5 average	-1.61					-2.70 ± 0.23	-5.03 ± 0.24
M	6	−1.47	*23*****	−20.75	15.36			
N	7	−0.63	*****67*	−9.23	10.03			
O	7	−0.21	*****67*	−8.88	10.98			
P	8	1.05	***45678	−0.03	0.70	0.399 ± 0.084	-2.71 ± 0.14	-5.16 ± 0.34
Q	8	0.63	*2345678	−0.08	0.70	0.379 ± 0.073	-2.75 ± 0.09	-4.49 ± 0.21
R	8	−0.21	**345*78	−0.08	0.66	0.252 ± 0.178	-2.67 ± 0.11	-4.88 ± 0.27
S	8	0.21	12345678	0.00	0.00	0.430 ± 0.074	-2.73 ± 0.08	-4.49 ± 0.21
	Feature 8 average	0.42					-2.72 ± 0.01	-4.76 ± 0.14
			Group fitting			0.367 ± 0.037		
	Avg. of all features	-1.0 ± 0.5					-2.99 ± 0.16	-4.37 ± 0.43

Column (4): Epoch numbers assigned in column(1) of Table 1, while asterisk represents non-detection.

5.1.2.3 Internal maser motions

The absolute proper motion of maser features is a combination of the source systemic motion and the internal maser motions inherent in the source. By assuming that the internal maser motions are random and thus velocity vectors average to zero we can separate the internal motion from the source motion. This deconstruction was possible for 4 maser features for which the absolute proper motion could be measured. Fig. 5.10 illustrates the internal maser motions in IRAS 20143+3634. It can be seen that the more persistent, low-velocity maser features form a group confined to a 16×29 mas (44 × 79 AU using our distance) region. Their transverse velocities were in the range of 2.24 to 24.12 km s^{-1}. The nominal dispersion of these velocities is ∼10 km s^{-1}.

5.1.2.4 Systemic motion of IRAS 20143+3634

Estimating the source systemic motion using water masers may be controversial, since the maser emission is not biased to the mass of the source. In cases where maser emission clearly traces symmetrical structures, such as a bipolar outflow, the dynamic center of the source can be established by tracing the common origin of motion (*see, for example* Imai et al. 2011). This method assumes that all masers motions are driven by one common driving source. However, in the case where the nature of the driving mechanism is not so obvious it may be misleading to assume that a dynamic center of motion can be accurately found. Previous investigations of water maser sources suggest that the

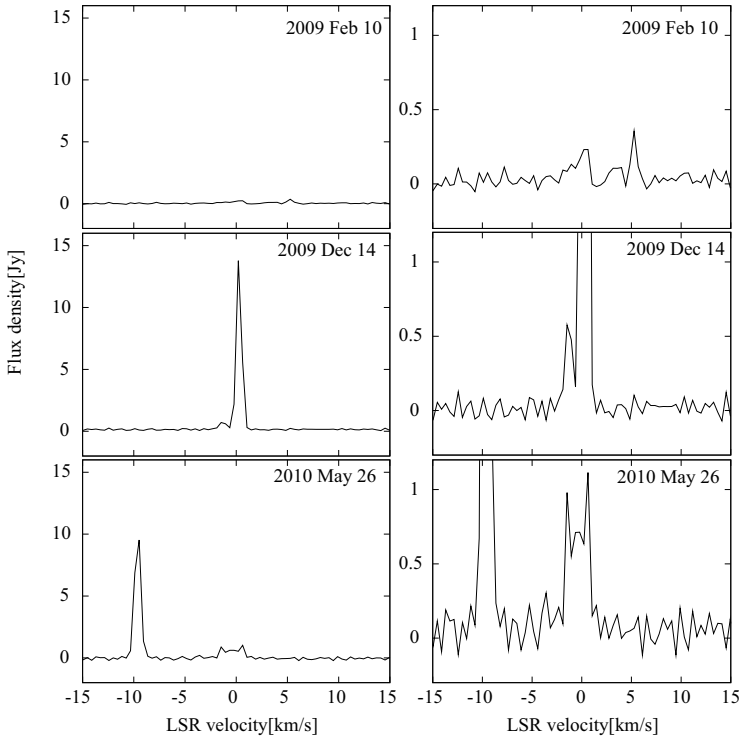

Figure 5.1: Scalar-averaged cross-power spectra of IRAS 20143+3634 at three epochs as noted in the top right corner of each panel, for full scale of the flux density (*left*), and expanded presentation (*right*).

average motion, based on well randomised maser features, gives an accurate estimation of the systemic velocity (Nagayama et al., 2011). In the case of IRAS 20143+3634 the distribution and radial velocities of masers seem randomised, as opposed to showing any bipolar structure. Therefore we estimate the systemic motion of IRAS 20143+3634 using the method demonstrated by Nagayama et al. (2011). Using this approach, the vector average of the four maser features for which proper motions were determined was $(\mu_\alpha \cos\delta,\ \mu_\delta) = (-2.99 \pm 0.16,\ -4.37 \pm 0.43)$ mas yr^{-1}. Where the error value is the standard error of the mean, $\sigma/\sqrt{4}$. Here, σ is the standard deviation of the proper motion of 4 features. This error evaluation was also used in the astrometric observations of WB89-437, ON1, and IRAS05168+3634 (Hachisuka et al. 2009; Nagayama et al. 2011; Sakai et al. 2012, respectively). The use of this method is reasonable for IRAS 20126+3634 because the averaged LSR velocity of the 4 features is -1 ± 1 km s^{-1}, which is consistent with the systemic LSR velocity indicated by the associated molecular cloud ($v_{\rm LSR} = -1 \pm 1$ km s^{-1} Ao et al. (2004)).

The observed proper motion is relative to the Sun. To evaluate the motion relative to the LSR, which we call the LSR proper motion, we have to correct for the Solar motion with respect to the LSR. In this paper we use the traditionally defined value of $(U_\odot, V_\odot, W_\odot) = (+10.3,\ +15.3,\ +7.7)$ km s^{-1} (Kerr & Lynden-Bell 1986, *see*

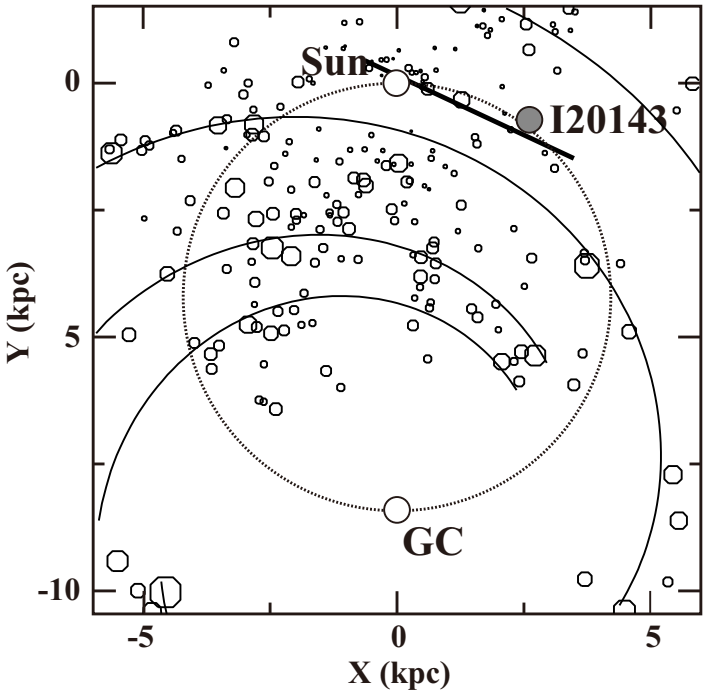

Figure 5.2: The location of IRAS 20143+3634 as seen from a face-on view of the Milky Way (shown as I20143). The dotted circle traces the tangent points. The background is the spiral structure from fig. 5 of Russeil (2003) showing the Local arm (solid line), in which they assume $R_0 = 8.5$ kpc. IRAS 20143+3634 is located near to the tangent point and in the local arm.

also Ando et al. 2011). We calculated the proper motion of IRAS 20143+3634 to be (μ_l, μ_b)=$(-5.75 \pm 0.33, +0.62 \pm 0.32)$ mas yr^{-1} with respect to the LSR, which, using our distance measurement of 2.72 kpc, yields velocities in the Galactic co-ordinates of (v_l,v_b)=$(-74.1 \pm 4.3, +8.0 \pm 4.1)$ km s^{-1}.

5.1.3 Discussion

5.1.3.1 Physical parameters of IRAS 20143+3634

Mass and luminosity are fundamental parameters of a SFR, whose evaluation depends on the estimated source distance. Our trigonometric distance revises the previous estimate by a factor of about 2. We therefore should revisit past estimates of the physical parameters of IRAS 20143+3634.

Ao et al. (2004) estimated the core mass of IRAS 20143+3634 to be $M_{\rm LTE} = 64 M_\odot$ from CS($J = 2-1$) emission (see Fig. 5.12) under the assumption of local thermodynamic

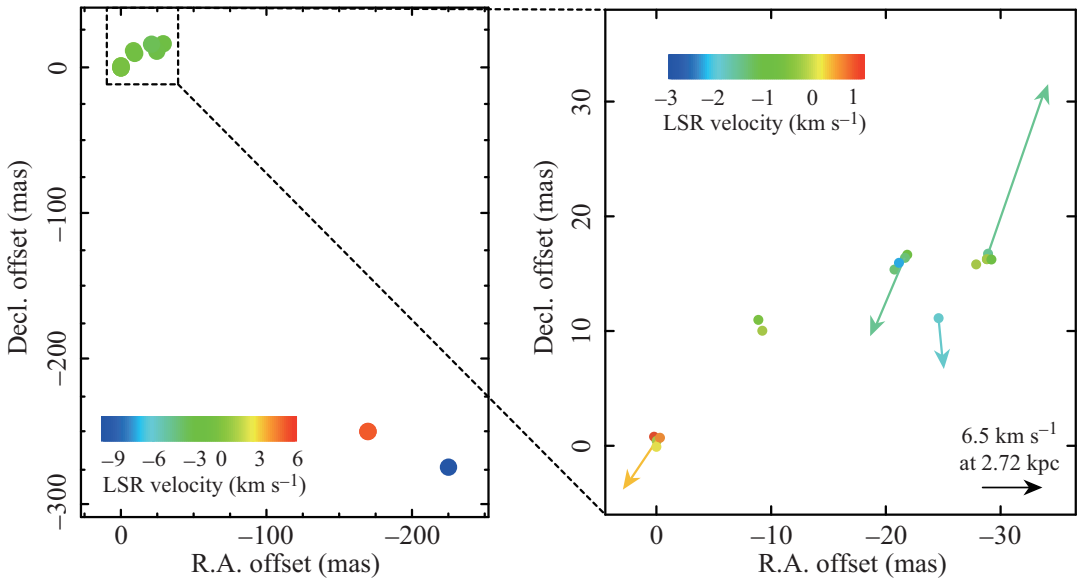

Figure 5.3: Spatial distribution of H_2O maser spots in IRAS20143+3634. Colour indicates the LSR velocity of maser spots, and arrows indicate the internal proper motions of maser features. The origin of the offset is the position of maser spot S with $v_{\rm LSR} = 0.21$ km s^{-1} at $\alpha = 20^h16^m13^s.3617$, $\delta = 36°43'33.920"$(J2000.0)

equilibrium (LTE). From velocity dispersion of the same emission they also estimated a virial mass of $M_{\rm vir} = 360 M_\odot$. With our new distance measurement we re-estimated a core mass of $M_{\rm LTE} = 22 M_\odot$ and $M_{\rm vir} = 213 M_\odot$, and infrared luminosity of $L_{\rm IR} = 894\, L_\odot$.

The revision of the distance reduces $M_{\rm LTE}$ and $L_{\rm IR}$, and enlarges the ratio $M_{\rm vir}/M_{\rm LTE}$. It enforces the trend which Ao et al. (2004) show in their fig 14; the less massive cores have a larger excess of $M_{\rm vir}$. As discussed in Ao et al. (2004), it suggests that the turbulent motion in the core dissipates gradually during the formation of the core and subsequent star formation. In their samples IRAS 20143+3634 is in the youngest stage.

The spectral energy distribution (SED) is a good indicator of the properties of the energy source. We compiled the SED of IRAS 20143+3634 using photometric data from the AKARI satellite measured with the Infrared Camera (IRC) and Far-infrared Surveyor (FIS) under AKARI point source names 2016133+364333 and 2016128+364336 respectively, and WISE magnitudes under the source name J201613.38+364333.6. These data are employed in the SED shown in Fig. 5.13.

We used a catalogue of young stellar object (YSO) models from Robitaille et al. (2007) and their SED fitting tool to find the best fit to the data via a reduced χ^2 approach. The best fit corresponds to a YSO of mass $7.62 M_\odot$, stellar temperature of $\sim 20,000K$, luminosity of $3 \times 10^3 L_\odot$ and stellar age of about 2×10^5 years. The best fit model presents an envelope mass of $\sim 29 M_\odot$ contained within an outer radius of 1×10^5AU. Combining our SED model results with re-estimations of the findings of Ao et al. (2004) we conclude that IRAS 20143+3634 appears to harbour an intermediate

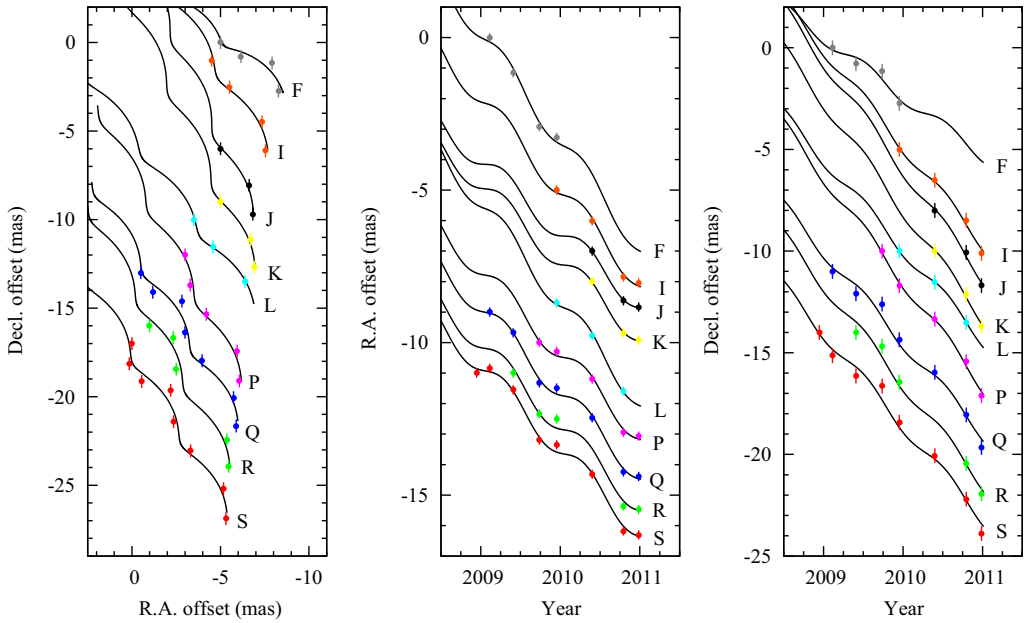

Figure 5.4: Apparent motions of 9 H_2O maser spots in IRAS20143+3634 on the sky, with positional errors, and the best-fit curves which were applied to the parallax and proper motion. Each maser spot is represented by an individual colour for clarity. (*Left*) positions of maser spots in R.A. and Decl. with time running from top-left to bottom-right. (*middle*) R.A. offsets over time, and (*right*) Decl. offsets over time.

to high mass YSO with outflows, imbedded in a hot molecular core and still accreting material. It is at an early evolutionary stage, resembling a Class I YSO.

5.1.3.2 The angular velocity of Galactic rotation of the LSR, Ω_0.

Nagayama et al. (2011) demonstrated that the angular velocity of Galactic rotation at the Solar radius, Ω_0, which equates to the ratio of the Galactic constants Θ_0/R_0, can be evaluated using astrometric observations of a source near the tangent point. For a source circularly rotating around the Galactic center on the Galactic plane at the Galactic longitude l, it is given by

$$\Omega_0 \quad = \quad -a_0\mu_l + v_r\left(\frac{1}{D\tan l} - \frac{1}{R_0\sin l}\right) \tag{5.1}$$

where D is the distance to the source from the Sun, v_r is its LSR velocity, μ_l is its systemic proper motion, and a_0 is a unit conversion factor from μ_l to Ω_0 or $a_0 = 4.74$ km s^{-1} kpc^{-1} (mas yr^{-1})$^{-1}$. In Equation (5.2), the second term becomes small for a source located near the tangent point, because $D\tan l = R_0\sin l$ at the tangent point (Nagayama et al., 2011). Moreover, the LSR velocity of IRAS 20143+3634 is also small. We can, therefore, estimate Ω_0 with improved accuracy from our data.

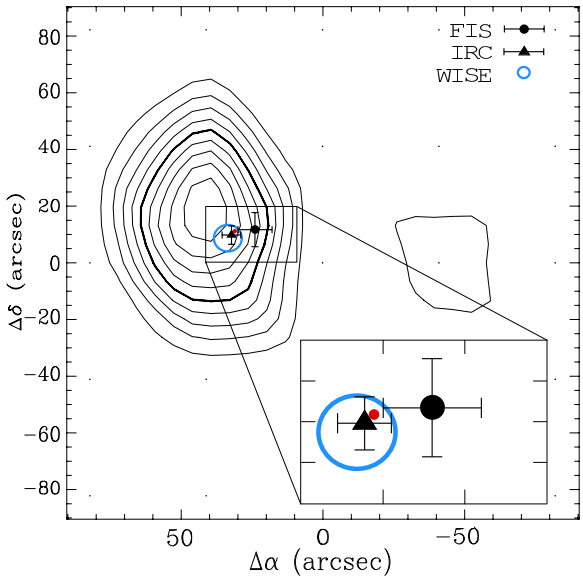

Figure 5.5: A contour map of CS line emission from Ao et al. (2004) with positions and accuracies of the sources detected with AKARI-FIS, AKARI-IRC, and WISE *(blue)*. The position of the H_2O masers is indicated by the small, *(red)* filled circle. The 30"×20" area around the masers is magnified for clarity.

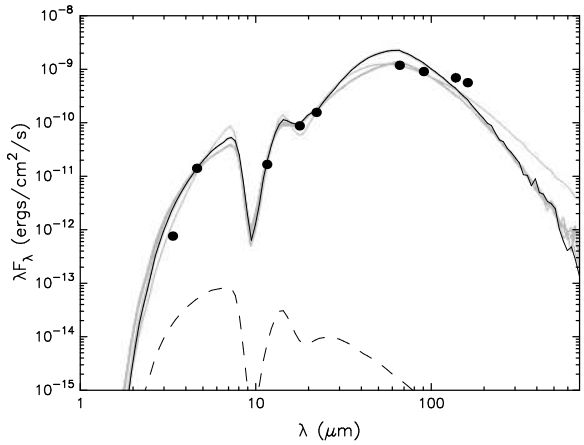

Figure 5.6: SED of MIR and FIR dust emission measured with AKARI at $\lambda = 18\mu$m 65μm 90μm 140μm and 160μm and WISE at $\lambda = 3.4\mu$m 4.6μm 12μm and 22μm. The thick black line shows the best fit to the photometry data, grey lines represent near-fit models with $\chi^2 - \chi^2_{best} < 3$. The dashed line shows the expected blackbody contribution from an embedded object.

By applying the observable quantities determined in this paper, namely $D = 2.72^{+0.31}_{-0.25}$ kpc, $\mu_l = -5.75 \pm 0.33$ mas yr^{-1}, and $v_r = -1.0 \pm 1.0$ km s^{-1} from the CS($J = 2-1$) line observations of Ao et al. (2004), we derive an angular velocity of the Galactic rotation at the LSR of $\Omega_0 = 27.3 \pm 1.6$ km s^{-1} kpc^{-1}, when we assume $R_0 = 8$ kpc. We demonstrate how the derived value of Ω_0 is less sensitive to the choice value of R_0 by varying it between the values $7 \leq R_0 \leq 9$ kpc. This only produces a deviation of $\Delta\Omega_0 = \pm 0.02$ km s^{-1} kpc^{-1}.

Prior to this work, there have been several VLBI astrometric observations of maser sources near the tangent points and the Solar circle. Their estimations of Ω_0 were $\Omega_0 = 28.7 \pm 1.2$ km s^{-1} kpc^{-1} for ON1 (Nagayama et al., 2011) and $\Omega_0 = 27.3 \pm 0.8$ km s^{-1} kpc^{-1} for ON2N (Ando et al., 2011). In cases where the authors had not done so, we estimated Ω_0 from the data of their observations, using the same method (and the same values in correcting for the Solar motion) as for IRAS 20143+3634. $\Omega_0 = 27.9 \pm 2.6$ km s^{-1} kpc^{-1} for W51 Main/South (Sato et al., 2010); $\Omega_0 = 27.8 \pm 1.0$ km s^{-1} kpc^{-1} estimated using the average of the proper motions of W75N, DR21, DR20 and IRAS20290+4052 in the Cygnus X region (Rygl et al., 2012); $\Omega_0 = 26.3 \pm 1.0$ km s^{-1} kpc^{-1} for W49N (Zhang et al., 2013). Our value of $\Omega_0 = 27.3 \pm 1.6$ km s^{-1} kpc^{-1} for IRAS 20143+3634 agrees very well with these values. With our result included, the mean value of Ω_0 estimated this way for tangent point and Solar circle targets is $\Omega_0 = 27.6 \pm 0.7$ km s^{-1} kpc^{-1}. All of these results are consistent with each other suggesting that the peculiar motions of these sources are small in the direction of Galactic rotation, and that the sources orbit circularly about the Galactic center.

Using a multi-parameter fitting procedure Honma et al. (2012) estimated $\Omega_0 = 29.2 \pm 0.8$ km s^{-1} kpc^{-1} for 52 SFRs measured with maser VLBI astrometry. Also, Reid & Brunthaler (2004) estimated $\Omega_0 = 28.2 \pm 0.2$ km s^{-1} kpc^{-1} from the proper motion of Sagittarius A* using VLBI astrometry. Furthermore, besides VLBI astrometry, Ω_0 was estimated using the velocity field of stars near the Sun; $\Omega_0 = 28.6 \pm 1.4$ km s^{-1} kpc^{-1} for Cephaid variables (Miyamoto & Zhu, 1998); $\Omega_0 = 31.6 \pm 1.4$ km s^{-1} kpc^{-1} for OB stars (Miyamoto & Zhu, 1998). The former is consistent with our value and the other VLBI estimations, although most targets of the VLBI estimations are SFR. Finally, since Ω_0 is the ratio of the Galactic constants, we can compare the value calculated using the IAU recommended Galactic constants; $\Omega_0 = 25.9$ km s^{-1} kpc^{-1} from $R_0 = 8.5$ kpc and $\Theta_0 = 220$ km s^{-1}. This value is significantly lower than ours and recent estimates.

We have summarised the current estimates of Ω_0 graphically, in Fig. 5.14. The horizontal axis denotes the distance to the sources used in each sample. Recent estimates of Ω_0 are consistent for a distance range of 1 to 8 kpc indicating that these estimates are not only valid in the local Galactic neighbourhood but also at larger distances from the Sun. This suggests that these sources rotate axisymmetrically in the disk of the Milky Way with only small peculiar motions.

The value of Ω_0 reveals non-linear distortion between the model and the actual velocity field in the disk of the Milky Way. It provides an additional and systematic error for distance estimates that are based on LSR velocities. Therefore, we should use a revised value of Ω_0. Fig. 5.14 suggests that the Galactic constants should be set with close attention paid to Ω_0 when they will be revised in the near future.

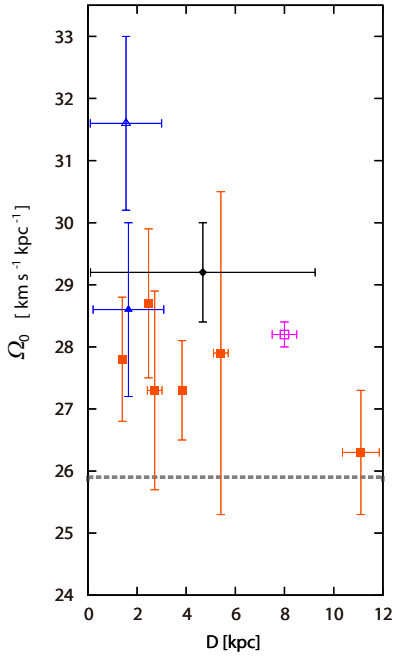

Figure 5.7: Estimated Ω_0 using different distance sources. The horizontal bar of each point represents the distance error or range of each sample. *Filled squares*: VLBI astrometry of tangent point and Solar circle targets (*In ascending distance: Cygnus X (Rygl et al., 2012), ON1 (Nagayama et al., 2011), IRAS 20143+3634 (this paper), ON2N (Ando et al., 2011), W51 Main/South (Sato et al., 2010), and W49N (Zhang et al., 2013)). Diamond*: Multi-parameter fitting for VLBI astrometry of 52 SFRs (Honma et al., 2012), *Open square*: Proper motion of Sgr A* (Reid & Brunthaler, 2004), *Open triangle*: Velocity field of 1352 OB stars and *Filled triangle*: 170 Cepheid variables (Miyamoto & Zhu, 1998), *Dashed line*: Calculated using the IAU 1985 recommended values.

5.1.3.3 Peculiar motion of IRAS 20143+3634

To evaluate the peculiar motion of the observed source with respect to the global Galactic motion we must consider the kinematics of the Galaxy. The observational properties of any Galactic sources depend both on the target source motion and that of the Sun. It is difficult to disentangle these two motions. With our estimate of $\Omega_0 = 27.6$ km s^{-1} kpc^{-1}, we infer $\Theta_0 = 221$ km s^{-1} for $R_0 = 8$ kpc, or $\Theta_0 = 235$ km s^{-1} for $R_0 = 8.5$ kpc. We can fairly assume the rotation velocity of IRAS 20143+3634 to be the same as Θ_0, because its Galactocentric distance is about $0.97R_0$; almost the same as the Sun.

Based on these two kinematic models we calculated the peculiar motion of IRAS 20143+3634 to be $(U_s, V_s, W_s) = (-0.9\pm2.9, -8.5\pm1.6, +8.0\pm4.3)$ km s^{-1} and $(U_s, V_s, W_s) = (-1.0 \pm 2.9, -9.3 \pm 1.5, +8.0 \pm 4.3)$ km s^{-1} for $R_0 = 8$ and $R_0 = 8.5$ kpc, respectively. Here, we again use $v_r = -1.0 \pm 1.0$ km s^{-1} from the CS($J = 2 - 1$) line observations of Ao et al. (2004). We adopt the notation used by Reid et al. (2009), where U_s is the velocity component toward the Galactic center, V_s is the velocity component measured

in the direction of Galactic rotation and W_s is the component of motion toward the north Galactic pole. By giving priority to the value of Ω_0, our two models are self-consistent within the errors for values of $8 \leq R_0 \leq 8.5$ kpc. If the Galactic constants were $R_0 = 8.5$ kpc and $\Theta_0 = 220$ km s^{-1} as given by the IAU recommended values, we instead measure a peculiar motion of $(U_s, V_s, W_s) = (3.8 \pm 2.9, -8.5 \pm 1.5,\ 8.0 \pm 4.3)$ km s^{-1}.

In all these cases the magnitude of peculiar motion of IRAS 20143+3634 in the Galactic plane is about 10 to 13 km s^{-1}, which is consistent with the random velocity of molecular clouds in the galactic disk. This suggests that the large discrepancy of the previous distance estimation of IRAS 20143+3634, based on its LSR velocity, was not due to the peculiar motion of the source, but was mainly caused by the source being located in a region of the Galaxy where the kinematic velocity falls to a value that approaches the random motion velocity. In such a situation, the kinematic velocity cannot give an appropriate distance and other distance estimation methods should be used.

It is appropriate to mention that the estimated 3-dimensional peculiar motions of SFRs can be influenced by the internal motions of masers, whereby an asymmetrically biased motion traced by water masers in particular could lead to a misinterpretation of the secular motion. A prominent example of an asymmetric outflow is shown in De Buizer (2006) where masers trace a one-sided jet. Comparison with the radial and proper motions of a core tracing maser species, such as the *class II* methanol maser, is a suitable probe for this effect, highlighting the importance of observing SFRs using multiple maser species.

5.1.4 Conclusions

By observing H_2O masers for a period of over two years with VERA, we measured the parallactic distance of IRAS 20143+3634. Our distance of $D = 2.72^{+0.31}_{-0.25}$ kpc is 60% of the previous distance estimate based on the LSR velocity. The new distance places IRAS 20143+3634 in the Local spiral arm, near to the tangent point in the Cygnus direction.

With our distance estimate, we re-estimated the virial and core masses of IRAS 20143+3634 to be $M_{\rm vir} = 213 M_\odot$ and $M_{\rm LTE} = 22 M_\odot$ using data from Ao et al. (2004), which were 360 $M_\odot$ and 64 $M_\odot$ in the original paper, respectively. The source appears to be more violent than those authors previously thought and has yet to have dissipated turbulent motions inherent in the core. Nevertheless, their conclusions on the general trend of YSOs are still valid. Combining this view with an SED compiled from mid- and far-infrared fluxes from AKARI and WISE, IRAS 20143+3634 appears as a young, 7.62 $M_\odot$ intermediate to high mass YSO.

Our distance gives the location of IRAS 20143+3634 to be near the tangent point. As Nagayama et al. (2011) show, astrometric observations of a source near the tangent point provide the ratio of the Galactic constants Ω_0 with little dependence of the Galactocentric distance of the Sun, R_0. From the astrometry of IRAS 20143+3634 we obtained $\Omega_0 = 27.3 \pm 1.6$ km s^{-1} kpc^{-1}. The value changes only ± 0.02 km s^{-1} kpc^{-1}, if we vary the value of the Galactocentric distance to the Sun between $7 \leq R_0 \leq 9$ kpc.

The values of Ω_0 derived from previous VLBI astrometric observations of sources near the tangent points and the Solar circle are consistent with each other. This consistency supports the simple circular rotation model of the Milky Way. The average value of these

estimates is $\Omega_0 = 27.6 \pm 0.7$ km s^{-1} kpc^{-1}. This value is also consistent with values based on other procedures and it is worth noting that all but few are higher than that calculated from the ratio of the Galactic constants recommended by the IAU since 1985 (Kerr & Lynden-Bell, 1986). The peculiar motion of IRAS 20143+3634 deviates from the simple circular rotation by about 10 km s^{-1}, which is consistent with the random velocity of sources in the Galactic disk.

5.2 IRAS 20056+3350: Solar circle

The morphology of a galaxy is determined visually and is highly influenced by the distribution of massive stars which are bright and typically confined to the spiral arms (Urquhart et al., 2014; Reid et al., 2014). Although the exclusivity of massive star formation to the spiral arms is not yet understood it does bring to light a strong interplay between the spiral pattern itself and the conditions required to trigger massive star formation. Thus, neither phenomena can be understood independently; we cannot explain massive star formation without explaining the role of the spiral pattern and we require the by-products of massive star formation to understand the morphology of galaxies by tracing the arms.

From our viewpoint within the Galactic disk, perhaps the most important parameter common to both fields of investigation is distance. In addition to the clear necessity of accurate distances for mapping the Galactic arms, the interpretation of the physical properties of a massive star forming region (MSFR) is greatly influenced by the distance estimate adopted - since many of these parameters have a non-linear relationship with distance.

For convenience, many investigators make use of the kinetic distances of Galactic star forming regions (SFRs). However, kinetic distance calculations require pre-calibration of the Galactic rotation curve and suffer from distance ambiguities ($D_{\rm near}$ and $D_{\rm far}$) for objects in the inner Galaxy. Moreover, they are unreliable when the source has a large peculiar velocity with respect to purely circular rotation in the Galactic disk. Consequently, the kinetic distance can be poorly determined for objects in some particular locations in the direction of the Galactic center and anticenter, and Local Arm.

Measurements of trigonometric parallaxes to Galactic MSFRs directly improves the reliability of their distances. Such experiments involve measurement of the annual parallax of MSFRs typically via astrometric monitoring of maser spots using VLBI networks such as the VLBI Exploration of Radio Astrometry (VERA), the Very Long Baseline Array (VLBA), and the European VLBI Network (EVN). In addition to distance measurement, masers are also extremely useful for understanding the processes of star formation itself since masers emitted by different molecular species and transitions are known to be associated with different physical environments (Bartkiewicz & van Langevelde, 2012). As a result, masers are often seen to trace structures such as expanding shells and shock fronts (Trinidad et al., 2013), and bipolar outflows (Imai et al. 2007; Nagayama et al. 2008; Moscadelli et al. 2011; Torrelles et al. 2014 and G236.81+1.98 in Choi et al. 2014). Masers thus allow the internal motions of star formation mechanisms to be seen even though the structures themselves may not be directly unobservable due to the embedded nature of such systems.

Finally, combining the proper motions and line of sight motions of masers sometimes allows estimation of the three-dimensional secular motions of a star forming region in the plane of the Galaxy. This is one of the unique advantages of VLBI maser investigations and is a dominant approach to understanding the kinematics and structure of the Milky Way Galaxy (MWG) via the evaluation of the Galactic constants, R_0, Θ_0 and Ω_0 (Honma et al., 2012; Reid et al., 2014). These parameters can be evaluated more reliably for SFRs that reside at special locations in the MWG such as the tangent points (Nagayama et al., 2011; Burns et al., 2014b) and Solar circle (Ando et al., 2011; Burns et al., 2014a).

All VLBI observations discussed in this paper were carried out using VERA (Kobayashi et al., 2003) which is a Japanese VLBI array dedicated to measuring the annual parallax of maser sources in the MWG. IRAS 20056+3350 was chosen for this investigation for its bright and stable maser emission at 22 GHz - first seen in Jenness et al. (1995) - and its presumed proximity to the Solar circle. IRAS 20056+3350 is listed in the IRAS catalogue of point sources (Beichman et al., 1988).

In this work we aim to make a contribution to each of the aforementioned topics. This paper continues as follows: Observations and data reduction are discussed in §2. Results are reported in §3, including analyses of the astrometric accuracy achieved in parallax fitting of maser spots. The physical nature of the IRAS 20056+3350 MSFR is explored in §4 in the context of archive and publicly available data, and its location is discussed with respect to other MSFRs who's distances have also been measured with VLBI annual parallax. Finally in this section we evaluate Ω_0 using the results obtained from our observations with VERA. Conclusions are reported in §5.

5.2.1 Observations and data reduction

Data were obtained using VERA in dual-beam mode. By observing H_2O masers in IRAS 20056+3350 and the J2010+3322 reference continuum source simultaneously we calibrated tropospheric phase fluctuations using the reference source and applied solutions directly to the maser data in real-time without interpolation.

We observed two sets of maser and continuum source pairs in each epoch; IRAS 20056+3350 and J2010+3322 and another pair IRAS 20215+3725 and J2015+3710. We do not use the latter in this work however we will discuss the results in a separate paper. The scan integration time of the pair is about 9 minutes. Intermittent observations of BL Lac or 3C454.3 were made every 1.5 hours for bandpass calibration. A typical observation session lasted roughly 8 hours, providing $\sim$ 3.3 hrs on-source integration and good coverage in the uv plane. Phase tracking centers for the maser and continuum source were set to $(\alpha, \delta)_{\rm J2000.0} = (20^{\rm h}07^{\rm m}31^{\rm s}.2593,\ +33^\circ59'41''.491)$ and $(\alpha, \delta)_{\rm J2000.0} = (20^{\rm h}10^{\rm m}49^{\rm s}.7233,\ +33^\circ22'13''.810)$, respectively. The positional reference J2010+3322 is listed in the VLBA calibrator search catalogue Fomalont et al. (2003).

Left-handed circular polarisation signals were sampled with 2-bit quantisation, and filtered with the VERA digital filter unit (Iguchi et al., 2005). The total available bandwidth of 256 MHz was divided into 16 intermittent frequency (IF) channels, each with a bandwidth of 16 MHz. One IF was centered on the maser emission, assuming a rest frequency of 22.235080 GHz, and the other 15 IFs, in adjoining frequency, were allocated to the continuum reference source.

Seven epochs of observations were carried out over a period slightly short of two years with epochs typically spaced 3-6 months apart. A summary of the observing calendar is given in Table 5.3. Maser spots were readily identifiable from one epoch to another due to the stability of emission and the low number of maser features (*see Section 3.1*).

Table 5.3: Summary of observations made with VERA.

Observation Epoch	Date	Detected spots
1	2012 Feb 05	2
2	2012 Apr 30	2
3	2012 Aug 09	2
4	2013 Feb 16	3
5	2013 Apr 22	3
6	2013 May 05	2
7	2013 Dec 24	2

Interferrometric correlation was carried out using the Mitaka FX correlator (Chikada et al., 1991). A frequency resolution of 15.625 kHz, corresponding to a velocity resolution of 0.21 km s^{-1}, was used for the maser data, and for the continuum source a frequency resolution of 250 kHz was used. We did not use the central IF of the continuum source data during data reduction since the frequency resolution of this IF channel did not match that of the other 14 IFs. This is an affect of the correlation process whereby the frequency resolution of this IF reflects that of the maser data. The small loss of bandwidth does not effect our goals adversely since the continuum source is readily detected with a signal to noise ratio of $\geq$ 80 without the inclusion of the central IF channel.

GPS measurements of the atmospheric water vapour content at each station were used to refine an a-priori model of tropospheric delay expected during the rise and fall of source elevation (Honma et al., 2008a). Model solutions were applied post-correlation. In the 6th epoch, GPS data were not available at VERA's Ogasawara station. For this epoch we instead used water vapour measurements from the Japan meteorological association (JMA) to the same effect, though at a lower time resolution. The reliability of these procedures is explored in detail in Nagayama et al. (2015).

All data were reduced using Astronomical Image Processing System (AIPS) developed by the National Radio Astronomy Observatory (NRAO). Amplitude and bandpass calibration for both beams was carried out using the standard procedures of reduction of astrometric VLBI data in AIPS. During the first round of data reduction we created phase referenced images of the maser emission by calibrating maser data using phase solutions obtained for J2010+3322 in the AIPS task FRING. The positions of masers were determined by the peaks of 2D Gaussian fits applied to the final images. Using this procedure we found the two brightest maser spots (spot ID:A and spot ID:B; *see*

Table 5.4). The other spots (spot ID:C and spot ID:D) were only seen in self-calibrated images created in the second round of data reduction. In this reduction procedure we made single-beam images by self-calibration using the AIPS task pair IMAGR and CALIB on the brightest maser spot (spot ID:A). Subsequent maser positions were determined relative to the astrometric position of the bright reference maser, which was determined from the phase-referenced map.

5.2.2 Results

5.2.2.1 Distribution of H_2O masers in IRAS 20056+3350

A modest total of 4 individual maser spots were detected in our observations. Maser spot detections are summarised in Table 5.4 where position offsets are given relative to the reference maser (Spot ID:A) for which we measure first epoch absolute co-ordinates of $(\alpha, \delta)_{\rm J2000.0} = (20^{\rm h}07^{\rm m}31^{\rm s}.2586, +33°59'41".477)$. The LSR velocity domain of masers, ascertained from Doppler shifts, ranges from -2.25 to $+7.27$ km s^{-1}. Thus, all detected masers are blueshifted with respect to the parent cloud - whose velocity from molecular line observations is known to be $+9$ km s^{-1} (*see section 4.2.1*). The spatial distribution and velocities of maser spots detected in IRAS 20056+3350 are presented in Fig. 5.11 with arrows indicating proper motion vectors (*see section 3.4*).

Table 5.4: The general properties of H_2O maser in IRAS 20056+3350 detected with VERA.

Spot ID	$V_{\rm LSR}$ (km s^{-1})	Detected epochs	$\Delta\alpha\cos\delta$ (mas)	$\Delta\delta$ (mas)	π (mas)	$\mu_\alpha\cos\delta$ (mas yr^{-1})	μ_δ (mas yr^{-1})
A	+7.27	1234567	0	0	0.213 ± 0.028	-2.62 ± 0.14	-6.04 ± 0.03
B	+7.27	12345**	-2.03	+0.65	0.212 ± 0.055	-3.33 ± 0.23	-6.00 ± 0.05
C	-2.25	****456*	-521.69	+581.19		-1.92 ± 0.14	-4.91 ± 0.03
D	+0.25	*******7	+804.61	+3.47			
			Group fitting		0.213 ± 0.026		
	Average					-2.62 ± 0.33	-5.65 ± 0.52

Column (3): Epoch numbers assigned in column(1) of Table 1, while asterisk represents non-detection.

5.2.2.2 Annual parallax

Parallax and proper motion fitting was performed simultaneously on the two maser spots which were identifiable in multiple observations, spanning more than one year. Astrometric motions of these spots were deconstructed into linear and sinusoidal components arising from the sky-plane proper motion and annual parallax, respectively. In the fitting procedure, nominal fitting errors in the R.A. and Dec. directions were applied and reduced itteratively until a χ^2 value of unity was reached. These error floors were 0.227 mas in R.A. and 0.050 mas in Dec.

When data were fit using the two most stable and brightest maser spots (Spot ID:A and ID:B) together we derived an annual parallax of $\pi = 0.213 \pm 0.026$ mas (*uncertainty of* 12.4%), corresponding to a distance of $D = 4.69^{+0.65}_{-0.51}$ kpc. Results of the fitting procedure are illustrated in Fig. 5.8. When repeating the fitting procedure for these spots individually we arrived at consistent values for both the distance and error floors

(*see Table 5.4*). It is clearly seen in Fig. 5.8 that the data were fit well in the Dec. direction and poorly in the R.A. direction. The cause of this situation in the context of astrometric accuracy is revisited in the next subsection.

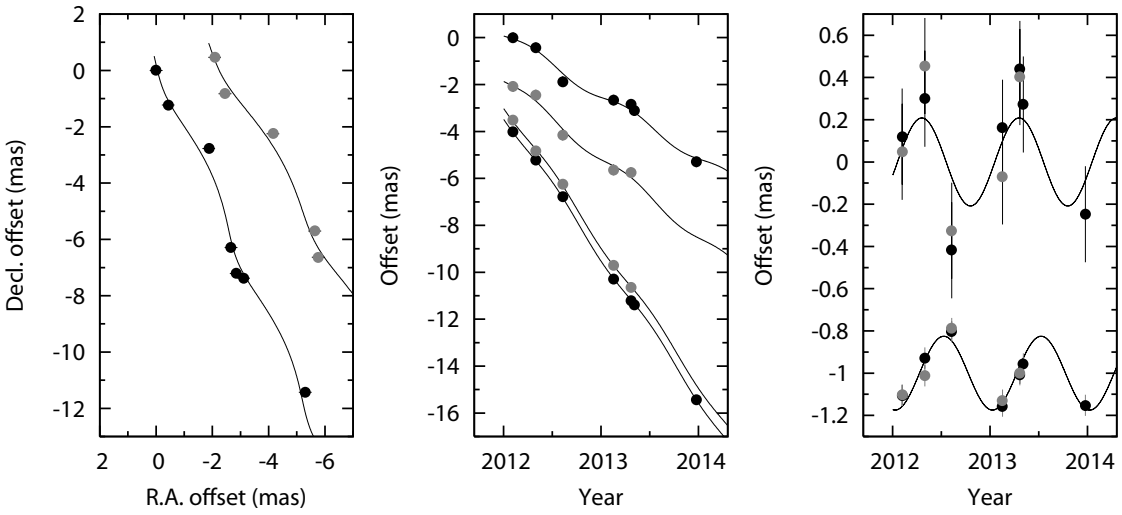

Figure 5.8: Parallax and proper motion fitting for two maser spots in IRAS 20056+3350. Spot ID:A and ID:B are represented by black and grey points respectively. Left: Sky-plane motion of the maser spots. Middle: motion in R.A. (above) and Dec. (below) as a function of time. Right: parallactic motion in R.A. (above) and Dec. (below) after subtraction of the linear proper motion (result for the combined fit).

Molinari et al. (1996) were the first to estimate the kinematic distance to IRAS 20056+3350. Assuming that the source is at the near kinematic distance for Galactic rotation, and using the IAU recommended Galactic constants of $R_0 = 8.5$ kpc and $\Theta_0 = 220$ km s^{-1}, they derived $D = 1.67$ kpc from the radial velocity of of their NH_3 line observations at $v_{LSR} = 9.4$ km s^{-1}. To date, this value has been adopted in all subsequent literature regarding this source. Assuming Galactic constants $R_0 = 8.05$ kpc and $\Theta_0 = 235$ km s^{-1} (at $V_\odot = 15.3$ km s^{-1}; Honma et al. 2012) and the condition of flat Galactic rotation $\Theta = \Theta_0 = 235$ km s^{-1}, we calculate the near and far kinematic distances of IRAS 20056+3350 as $D_{near} = 1.2$ kpc and $D_{far} = 3.9$ kpc respectively. Our distance obtained via trigonometric parallax is close to the far kinematic distance.

5.2.2.3 Analysis of astrometric accuracy

In the parallax fitting results of Fig. 5.8, the astrometric positions in the R.A. direction indicate a notably large degree of dispersion. Upon inspection of the brightness peaks in the emission maps, which we present in Fig. 5.9, emitting regions exhibit structural elongation primarily in the R.A. direction. To investigate the astrometric error contribution from the structure of masers we monitored the spatial separation between the two

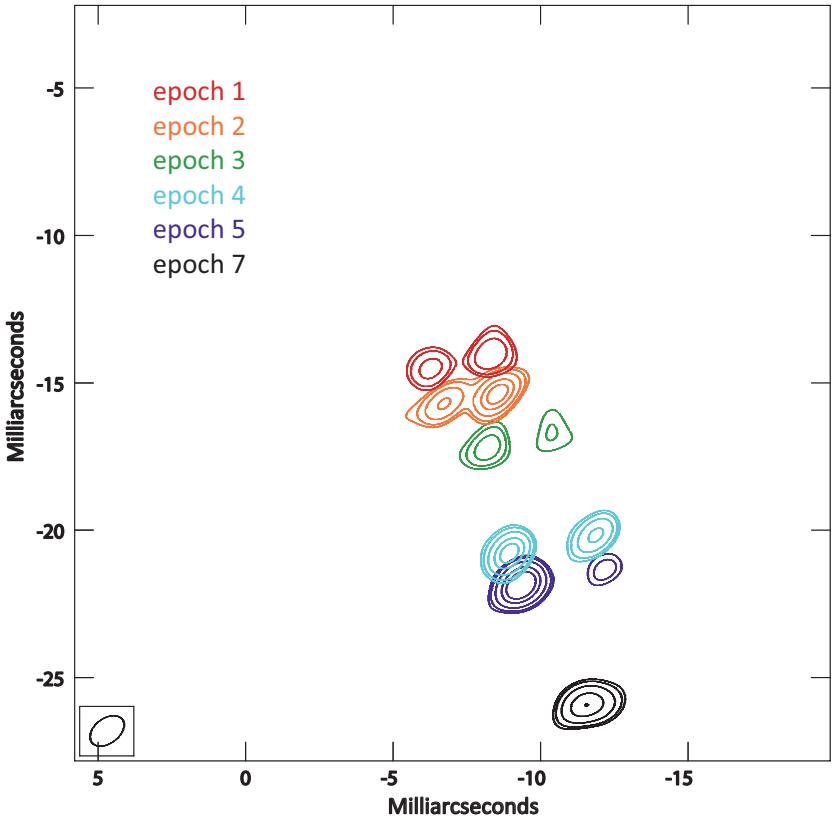

Figure 5.9: Multi-epoch phase-referenced images of the prominent maser spots (*Left* Spot ID:A and *Right* ID:B). The background emission from noise has been removed artificially to highlight the emission of maser spots used in our analysis. Maser spots move from center to south-west, chronologically (epoch numbers 1 to 7 are shown, however epoch 6 was omitted for its proximity to epoch 5 in time, which confused the image - Spot ID:B was not detected in epoch 6). Contours shown are multiples of 3, 5, 10, 20 and 30 of the root mean squared noise for individual maps. The origin of the map is $(\alpha, \delta)_{\rm J2000.0} = (20^{\rm h}07^{\rm m}31^{\rm s}.2593,$ $+33°59'41".491)$, and the first epoch absolute co-ordinates of spot ID:A was $(\alpha, \delta)_{\rm J2000.0} =$ $(20^{\rm h}07^{\rm m}31^{\rm s}.2586,$ $+33°59'41".477)$

bright, persistent maser spots. In the absence of acceleration, relative motions should be linear, thus we can compare the astrometric accuracy in R.A. and Dec. by evaluating the deviation from linear best fit motions in each respective direction. In Fig. 5.10, the large deviations from linearity seen in R.A. reveal an instability in the astrometric accuracy. These deviations are likely caused by the notable elongation of maser structures, which results in an inaccurate determination of emission peaks in the interferrometric images. The perceived elongation may be real structure, or it may be an apparent effect caused by the smearing of the two spots at small separation from each other. Furthermore, the spatial separation of maser spots was often close to the first side-lobe radius in the R.A. direction (about 2.5 mas in our VERA observations). Interaction of the maser emission

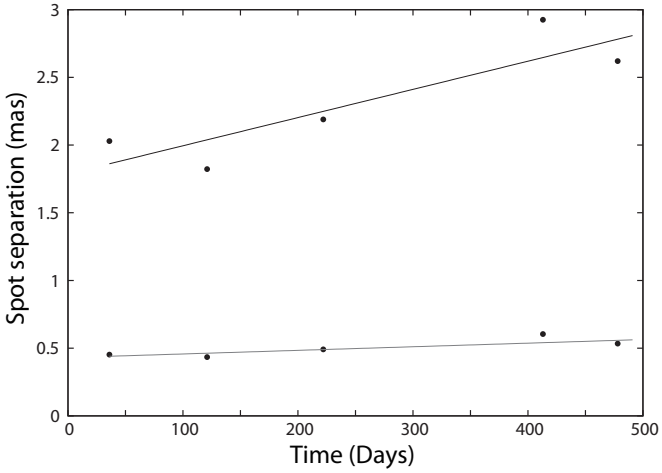

Figure 5.10: Spatial separation of the two prominent maser spots (Spot ID:A and ID:B) in R.A. (above) and Dec. (below) over the first five epochs in which both maser spots were detected. In the absence of acceleration, the relative motions of maser spots should manifest as a linear increase or decrease in spot separation over time. Best fits to the spot separation in R.A. and Dec. are overlain. Standard deviations to the best fits in R.A. and Dec. directions were 0.19 mas and 0.04 mas respectively. The first side-lobe radius, as discussed in the text, appears near 2.5 mas in our data, and thus only affects the R.A. separation.

with side-lobes is likely to have contributed additional smearing of emission peaks in the R.A. direction.

The standard deviation values for the linear fits in R.A. and Dec. were 0.19 and 0.04 respectively. These values are similar to the error floors arrived at in the parallax fitting procedure which were required to reach a χ^2 value of unity. Thus, our analysis suggests that the maser structure contributes a dominant source of astrometric error in these observations. Although this effect is detrimental for fitting the maser parallax in the R.A. direction, the astrometry in the Dec. direction is altogether unaffected, i.e this error is confined to the R.A. direction and thus supports preferential use of the Dec. direction offsets as the most suitable approach to parallax fitting.

5.2.2.4 Proper motion of H_2O masers

We found a third maser spot (spot ID:C) in 3 consecutive epochs of the self-calibrated images. In order to deconvolve parallactic and secular motions a maser via fitting a spot must be detected for around 1 year or longer in the phase-referenced images. However, we were able to estimate the secular motion of this spot via its relative motion to the bright maser spot (spot ID:A) detected in the self-calibrated images by assuming that both spots have a common annual parallax. By combining the relative maser motions with the known motion of the reference maser we obtained the sky-plane proper motion of the third spot, where the error is calculated as the quadrature sum of the standard deviation in the relative motion of masers, and the proper motion error of the reference

maser from parallax fitting. A fourth maser spot (spot ID:D) was detected in the final observation epoch only and thus its motion could not be found. Maser proper motions and their errors are listed in Table 5.4. Absolute maser proper motions are shown in Fig. 5.11 where arrows represent velocity vectors.

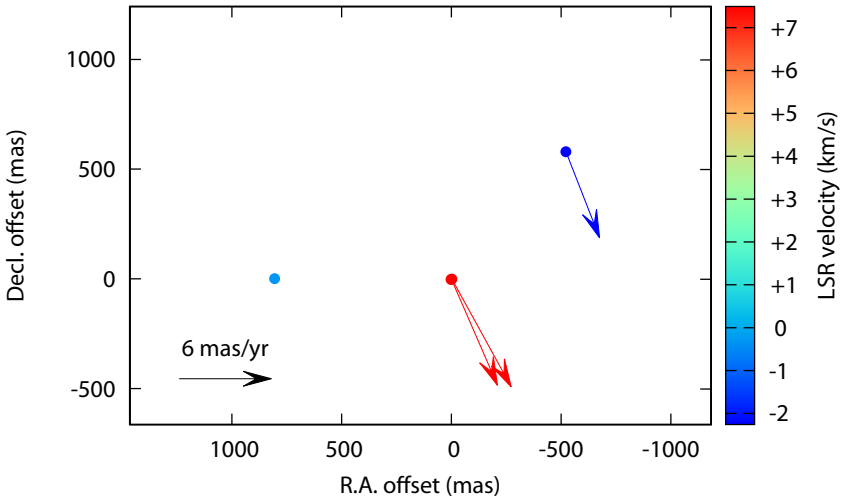

Figure 5.11: Distribution and absolute sky-plane proper motions of H_2O maser spots in IRAS 20056+3350. At $D = 4.69$ kpc typical motions of ~ 6 mas yr^{-1} correspond to velocities of ~ 135 km s^{-1}.

No obvious spatial nor velocity structure can be inferred from our maser vector maps alone. With the small number of maser spots it is unwise to search our images for self-contained geometric structures arising from phenomena such as bipolar outflows and spherical expansions; such analysis is powerful only if the number of maser spots is large enough to reveal structure in the velocity field in regions of star formation (*for example* Imai et al. 2011).

5.2.3 Discussion

5.2.3.1 The secular motion of IRAS 20056+3350

Zhang et al. (2005) presented an on-axis outflow mapped in CO which had a velocity centered at about +9 km s^{-1}, in agreement with other molecular line observations. Their spectra exhibit a triple-peak morphology with emission detected in the range of $0 \sim +20$ km s^{-1}. The peaks correspond to the blue-shifted outflow, the parent cloud and redshifted outflow, in ascending velocity. Since the $V_{\rm LSR}$ of our masers are all consistent with the blue limit of the CO emission we conclude that our observations are likely sampling masers associated with the blueshifted lobe of the outflow, which appears aligned to the line of sight. Although this does not allow direct interpolation of maser motions to a kinematic center, as is demonstrated in Imai et al. (2011), it does allow us to make the reasonable assumption that the sky-plane proper motions of maser spots with respect to the driving source are small, since the largest velocity components can

be expected along the line of sight, in agreement with the direction of the molecular outflow. As such, the average proper motion of maser spots should give a reasonable approximation to the secular motion of the SFR.

We evaluated the group averaged proper motion for all maser spots in IRAS 20056+3350 to be $(\mu_\alpha \cos\delta,\ \mu_\delta) = (-2.62 \pm 0.33,\ -5.65 \pm 0.52)$ mas yr^{-1}. Error values are the standard error of the mean, $\sigma/\sqrt{3}$, where σ is the standard deviation of the proper motion of 3 spots. After subtraction of the average group motion, residual motions reveal the internal kinematics of H_2O masers in IRAS 20056+3350. We present a map of the internal maser motions in Fig. 5.12.

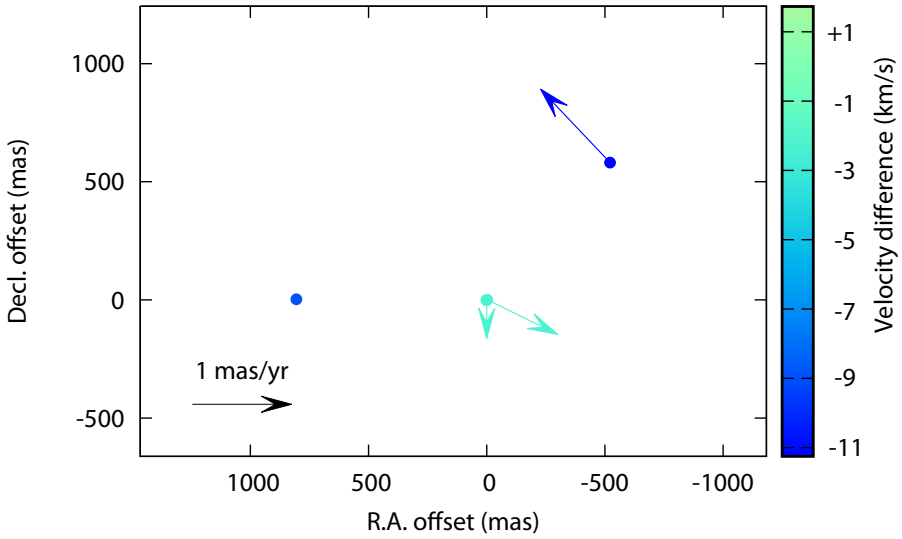

Figure 5.12: Internal motions of H_2O maser spots in IRAS 20056+3350. The systemic motion is assumed to be the average proper motion of all measured maser spots on the sky, and the radial velocity of the ambient molecular gas, 9 km s^{-1}. At $D = 4.69$ kpc typical motions of ~ 1 mas yr^{-1} correspond to ~ 22 km s^{-1}.

The proper motions of SFRs can be used to break the distance ambiguity associated with kinematic distance estimates because sources at near and far kinematic distances are expected to exhibit different proper motions on the sky. For IRAS 20056+3350 the near and far kinematic distances are $D_{\rm near} = 1.2$ kpc and $D_{\rm far} = 3.9$ kpc, respectively. Sources at these locations should show the proper motions of $\mu_l = -5.9$ mas yr^{-1} and $\mu_l = -6.2$ mas yr^{-1} respectively, if they rotate circularly around the Galactic center with $\Theta = 220$ km s^{-1}.

Using our estimate of the systemic proper motion of IRAS 20056+3350, $(\mu_\alpha \cos\delta,\ \mu_\delta)$ $= (-2.62 \pm 0.33,\ -5.65 \pm 0.52)$ mas yr^{-1}, we calculated the sky-plane motion of the source with respect to the Solar LSR in the direction of Galactic longitude as $\mu_l \cos b = -6.39 \pm 0.48$ mas yr^{-1}, using the standard solar motion $(U_\odot, V_\odot, W_\odot) = (+10.3, +15.3, +7.7)$ km s^{-1} (Kerr & Lynden-Bell 1986, *see also* Ando et al. 2011). This proper motion value is consistent with that estimated for a source at the far kinematic distance. Furthermore,

the far kinematic distance, $D_{\rm far} = 3.9$ kpc, is closer to our distance of $D_{\rm tri} = 4.96$ kpc, measured using annual parallax compared to the near distance $D_{\rm near} = 1.2$ kpc

5.2.3.2 The physical nature of IRAS 20056+3350

Since Molinari et al. (1996), all astrophysical works regarding IRAS 20056+3350 adopt the near kinematic distance of 1.67 kpc in analysis of their data. Our trigonometric distance of $D = 4.69^{+0.65}_{-0.51}$ kpc is 2.8 times larger, thus significantly impacting the interpretation of data collected up to now. As such, we briefly revisit these past observations to summarise the nature of IRAS 20056+3350 - re-evaluated using the trigonometric distance and include also relevant distance-independent results to provide a full account of this MSFR.

5.2.3.3 Interpreting archive data and using the revised distance

Wood & Churchwell (1989) developed a diagnostic tool used to identify embedded massive OB type stars using IRAS point source catalogue colour criteria. Using their method IRAS 20056+3350 is a candidate for harbouring at least one embedded massive star.

The infrared luminosity of IRAS 20056+3350 from the total IRAS fluxes was estimated as $\rm L_{IRAS} = 1100 L_\odot$ (Casoli et al., 1986) using an assumed distance of 1.0 kpc. At the new distance, 4.69 kpc, it is revised as $\rm L_{IRAS} = 24000\ L_\odot$. The bolometric luminosity of IRAS 20056+3350 should be close to $\rm L_{IRAS}$, assuming that most of the emission from the embedded central star is absorbed and then re-emitted at infrared wavelengths. Using $M \propto L^{3.6}$ (Allen, 1976), as was done in Casoli et al. (1986), the mass of a central star is revised from $7.0 M_\odot$ to 16.5 $\rm M_\odot$, although the authors did not present the mass of the star. Casoli et al. (1986) also produced a map in ^{13}CO $J(1-0)$ with 4.'4 resolution using the Bordequx 2.5 m telescope and estimated a gas mass of $\rm M_{H2} = 56\ M_\odot$ assuming local thermodynamic equilibrium (LTE), a distance of D = 1 kpc and an abundance ratio of $^{13}\rm CO/H_2$ of 2×10^{-6} from Dickman (1978). The molecular gas mass is revised from 56 $M_\odot$ to $\rm M_{H2} = 1200\ M_\odot$ using the same assumption as that of Casoli et al. (1986) but the revised distance.

Far infrared (FIR) continuum maps of IRAS 20056+3350 at 450 μ and 800 μ from Jenness et al. (1995) clearly show dense cores, indicative of embedded star formation. Their Figures 1 and 2 show that the far infrared emission is associated with both the IRAS point source and water maser source, although the emission peak at $450 \mu m$ is offset from the masers by 5" in the direction of the cluster center. Although radio continuum emission at 8 GHz was marginally detected in their VLA observation, no compact source was identified (Figure 6 in Jenness et al. 1995). This suggests that no $\rm H_{II}$ region is present, although Jenness et al. (1995) do not comment explicitly on this.

To establish the radial velocity of the system we used published thermal molecular line observations since these typically trace ambient molecular gas. The systemic velocities, velocity widths, and telescope beam sizes from single-dish molecular line observations of IRAS 20056+3350 are summarised in Table. 5.5. From these results we nominally conclude the LSR velocity of the system to be $+9.00 \pm 0.25$ km s^{-1}, where the error is the standard deviation of the listed values.

Table 5.5: Systemic velocity, velocity width, and beam size of IRAS 20056+3350 observations.

Transition	$v_{\rm LSR}$ (kms^{-1})	Δv (kms^{-1})	Beam size (arcsec)	*Ref*
CS $J = (2-1)$	+8.8	3.2	39	Bronfman et al. (1996)
CS $J = (5-4)$	+9.0	3.2	21	Jenness et al. (1995)
$C^{18}O$ $J = (2-1)$	+9.0	3.0	21	Jenness et al. (1995)
^{13}CO $J = (1-0)$	+8.56	4.9	55	Wu et al. (2001)
NH_3 $(1,1)$	+9.4	2.29	40	Molinari et al. (1996)
NH_3 $(2,2)$	+9.0	1.82	40	Molinari et al. (1996)

NH_3 (1,1) and (2,2) line observations of IRAS 20056+3350 were carried out by Molinari et al. (1996). The measured line widths were $\Delta v_{(1,1)} = 2.29$ km s^{-1} and $\Delta v_{(2,2)} = 1.83$ km s^{-1}, respectively. The NH_3 $(1,1)$ and $(2,2)$ lines predominantly trace the less dense envelope and the dense core, respectively. The authors argue that such sources, that exhibit lower velocity dispersion in the central core compared to the outer envelope are characteristic of the *lack* of an ultra compact H_{II} (UCHII) region, and possibly precede this stage.

Zhang et al. (2005) mapped IRAS 20056+3350 in CO $J = (2-1)$ using the NRAO 12m telescope and reported a molecular outflow centered at the position of the IRAS source. Lobes of blueshifted and redshifted emission are concentric in the sky-plane indicating that the outflow is orientated to a pole-on geometry. Three velocity components are easily distinguishable in their spectra (panel ID 115 in Fig.2 of Zhang et al. 2005). These components are symmetric about the center in the line profile: the blueshifted component which peaks at +5 km s^{-1}, the parent core at +9 km s^{-1}, and the redshifted component which peaks at +13 km s^{-1}. Emission was detected over the range of 0 to +20 km s^{-1}. From their CO $J = (2-1)$ data, Zhang et al. (2005) estimated the outflow parameters of IRAS 20056+3350 using the diagnostics of Garden et al. (1991). Using the near kinematic distance, they estimated the mass, momentum and energy of the outflow as $M_{outflow} = 2.3$ $M_\odot$, $p_{outflow} = 20.6$ $M_\odot$ km s^{-1} and $E_{outflow} = 2.8 \times 10^{45}$ ergs. Our new distance gives outflow parameters $M_{outflow} = 18$ $M_\odot$, $p_{outflow} = 163$ $M_\odot$ km s^{-1} and $E_{outflow} = 2.2 \times 10^{46}$ ergs.

5.2.3.4 Spectral energy distribution

A practical method for investigating the physical nature and evolutionary stage of an astronomical object is to draw information from its spectral energy distribution (SED). In this effort we constructed the SED of IRAS 20056+3350 using published data.

Infrared fluxes were extracted from point source catalogues using the NASA Infrared Science Archive (IRSA), from the telescope missions of UKIDSS, WISE, AKARI, and IRAS. We also use JCMT fluxes at 450 and 800 μm from Jenness et al. (1995).

Table 5.6: Flux parameters used in the SED fitting of IRAS 20056+3350.

Telescope	Band (name or μm)	Photometry (magnitude or flux)	Aperture size (arcsec)	Source name	Mission reference
UKIDSS	J	18.985 ± 0.105 mag	3	J200731.43+335937.6	Lucas et al. (2008)
	H	15.876 ± 0.012 mag	3	J200731.38+335939.4	
	K_s	12.815 ± 0.002 mag	3		
WISE	3.4	7.961 ± 0.024 mag	8.5	J200731.37+335940.9	Cutri et al. (2014)
	4.6	4.780 ± 0.04 mag	8.5		
	12	3.115 ± 0.016 mag	8.5		
	22	-1.127 ± 0.013 mag	16.5		
AKARI	9	5510 ± 59.2 mJy	6	2007315+335940	Ishihara et al. (2010)
	18	9298 ± 211 mJy	6		
IRAS	60	422 ± 63.3 Jy	120	20056+3350	Beichman et al. (1988)
	100	757 ± 121.12 Jy	120		
JCMT	450	33 ± 6.6 Jy	3	20056+3350	Jenness et al. (1995)
	800	6.2 ± 1.6 Jy	12		

The aperture sizes or angular resolutions of each of the catalogs were different. In Figure. 5.13 we show a three-colour image of IRAS 20056+3350 made using published data from UKIDSS in J, H, K_s bands, and whose catalogue has the the highest angular resolution of any we used. A distinctly redder region is seen in the center-western portion of the cluster. A star forming core with redder colours has more intense radiation at the longer wavelengths which is characteristic of cores which are forming more massive stars. We identify this region as the most likely site of embedded massive stars. Furthermore, a dark lane which is prominent in the K-band (Varricatt et al., 2010) and the association of H_2O masers support that this is a site of embedded star formation. Thus, we required that flux apertures from all point source catalogues be positionally consistent with this region. Details of the fluxes used in SED fitting are given in Table 5.6 and the position and sizes of apertures are overlaid onto Figure. 5.13.

Although the beams of the larger apertures will invariably contain multiple cluster members, we made no corrections for this because our target should be the brightest in the beam; our target is the most massive and the flux from other objects should be negligible, since the luminosity is extremely sensitive to the mass of the object, by the relation $L \propto M^{3.6}$.

To test the reliability of using the IRAS 60 and 100 μ bands in our SED we compared the photometries of IRAS $F_{24\mu}$ and WISE $F_{22\mu}$ and found them to be consistent, supporting the reliability of using the IRAS fluxes. 450 and 800 μ fluxes, measured using the James Clarke Maxwell telescope (JCMT) by Jenness et al. (1995), were evaluated with an aperture equivalent to the extent of the FWHM of the observed emission. Inclusion of these fluxes may leads to an overestimation of the integrated SED flux since hot gas associated with the outflow will be included. However, since the core emission is compact and centered on the maser source, the flux is likely dominated by the embedded massive star. These data provide valuable confines for the longer wavelength portion of the SED.

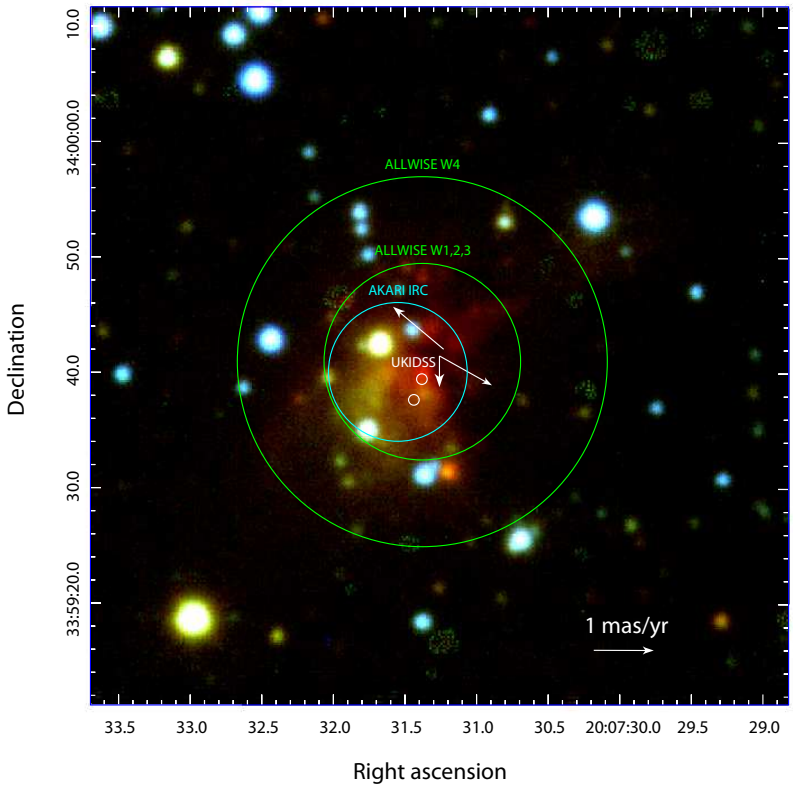

Figure 5.13: Aperture size and positions taken from point source catalogues of various infrared telescope missions. These correspond to photometric measurements used to evaluate the SED of IRAS 20056+3350, as is discussed in the main text. Apertures are plotted over the near-IR composite image from UKIDSS where colours *blue, green* and *red* correspond to bands J, H and K_s. Proper motions of H_2O masers observed with VERA are indicated by white arrow vectors. The IRAS aperture was too large to be displayed in this figure.

To interpret our photometric data we use the fitting tool of Robitaille et al. (2007) which is well documented in the introductory paper referenced here. The SED of IRAS20056+3350, according to the model fitting is shown in Fig. 5.14.

The SED model corresponds to a 18.4 $M_\odot$ central star of age 10^4yrs, embedded in an envelope of mass 3300 $M_\odot$. The total luminosity of the region is $2.45 \times 10^4 L_\odot$. The luminosity and stellar mass derived from the SED model agrees well with the estimates made using the four IRAS bands by of Casoli et al. (1986) re-evaluated using our distance estimate as $L_{\rm IRAS} = 24000 L_\odot$ and $M_* \sim 16.5 M_\odot$. Furthermore, the envelope mass derived from the SED model agrees within a factor of two with the estimate of the molecular hydrogen content made by Casoli et al. (1986) re-evaluated using our distance estimate as $M_{H_2} = 1200 M_\odot$.

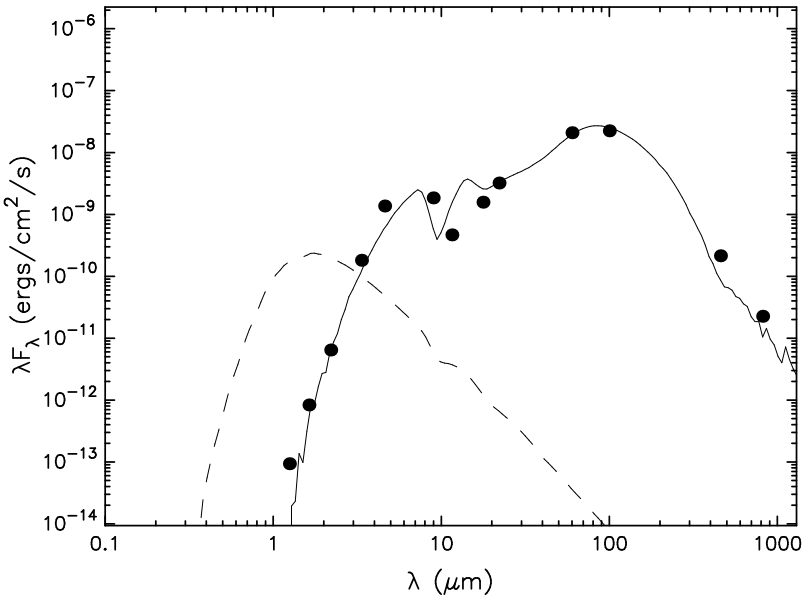

Figure 5.14: SED of IRAS 20056+3350 using data from UKIDSS, AKARI, WISE, IRAS and JCMT.

Interestingly, the inclination angle required to produce the best-fit model is 18° to the line of sight, which agrees with the general orientation inferred from the CO $J = (2-1)$ observations of Zhang et al. (2005). The ability of the SED fitting software to determine the inclination of young stellar object (YSO) systems solely from photometry data has been demonstrated for G34.4+0.23MM in Robitaille (2008) and for IRAS 04368+2557 in Robitaille et al. (2007). In these cases the system inclination had been previously established observationally from the orientation of bipolar outflows and was well matched by the SED fitting tool.

It should be pointed out that the successful fit of the SED model to the photometry data shows only that there exists a theoretical model *consistent* with the data and it is not *proof* that the model results truly reflect the nature of the source. The parameters directly determined from the data are luminosity and temperature of the emitting region, the further details (stellar mass, envelope mass, inclination, etc.) depend on the evolutionary tracks applied to the data, this is cautioned in Robitaille (2008). However, in our case the SED results are consistent with the picture drawn from an abundance of data from past observations re-evaluated at the trigonometric distance. It is this consistency rather than the pleasing appearance of the model fit to the data, that raises confidence in our results. These consistencies, along with the common proposed inclination angle, supports the basis of our argument; that the secular proper motion of IRAS 20056+3350 can be reasonably estimated from the group motions of H_2O masers associated with the line of sight outflow.

We conclude that IRAS 20056+3350 is a distant site of massive star formation at a young stage in evolution. The existence of an embedded, young massive star is strongly

suggested by the IRAS colours, SED, and presence a compact sub-millimeter core. With respect to youth, the evolutionary stage precedes the formation of an ultra compact H_{II} (UCHII) region, this is suggested from the turbulence ratio of the core and envelope seen in NH_3 and is corroborated by the lack of significant centimeter structure at 8GHz. Line spectra of core tracing molecular transitions such as CS reveal substantial turbulence (*see* Table. 5.5) which is suggested by Ao et al. (2004) to be characteristic of young SFRs which have not yet dissipated primordial turbulent motions inherent in the core. An active bipolar molecular outflow, seen in spectral wings and emission map, appears aligned to the line of sight - which we believe to be associated with the H_2O masers we observed with VERA due to the consistency of velocities. The overall picture ascertained from past observations is corroborated by the SED of IRAS20056+3350, which resembles a YSO in the Class I evolutionary phase.

5.2.3.5 Structure of the Local Arm

Full-scale studies of the structures of the spiral arms have recently been made available from analysis of the joint results of VLBI annual parallax measurements of MSFRs. Recent cases are; the Local Arm by Xu et al. (2013), the Perseus Arm by (Zhang et al., 2013; Choi et al., 2014), the Saggitarius Arm by Wu et al. (2014) and the general structure is discussed in Reid et al. (2014). IRAS 20056+3350 is the most distant MSFR in the Local arm for which a trigonometric distance has been determined. Therefore, although we cannot justify a large-scale re-evaluation of the Local arm, we can provide an important contribution to the picture recently provided by the aforementioned authors. The nature of the Local arm is discussed particularly in the work of Xu et al. (2013) where the authors consider the three possible scenarios; *1.* That the Local Arm is a branch of the Perseus Arm. *2.* That the Local Arm may be part of a major arm and connects to the Carina Arm. *3.* That it is an independent arm segment - a 'spur'.

In Fig. 6.1 we show the position of IRAS 20056+3350 in the context of the Galactic spiral structure, which was recently compiled by Reid et al. (2014) (*References for individual SFRs therein*). In drawing logarithmic spiral arms they used the Galactocentric distance of the Sun, $R_0 = 8.34$ kpc.

As seen in Fig. 6.1, the Galactic location of IRAS 20056+3350 diverges somewhat from the logarithmic curve determined for the Local arm by Reid et al. (2014). Deviation is in the direction of the Perseus arm and follows the example of three other MSFRs at the leading tip of the arm; G075.76+00.33 (Xu et al., 2013), G075.78+00.34 (Ando et al., 2011; Xu et al., 2013) and AFGL 2591 (Rygl et al., 2012). The location of IRAS 20056+3350 is generally consistent with what would be expected in the scenario where the Local Arm joins onto the Perseus arm further down into the spiral pattern - scenario *1.* of Xu et al. (2013). However, the alternative scenarios cannot be ruled out until this region of the Galaxy is mapped in more detail.

5.2.3.6 Evaluation of the Ω_0 Galactic constant

From our trigonometric distance we calculated the Galactocentric distance of IRAS 20056+3350 to be $R_* = 7.91$ kpc, when using $R_0 = 8.05$ kpc from Honma et al. (2012).

Since $R_* \simeq R_0$, and from the low value of $v_{\rm LSR} = 9$ km s^{-1}, it is evident that IRAS 20056+3350 resides spatially and kinematically near to the Solar circle.

Nagayama et al. (2011) demonstrated that the angular velocity of Galactic rotation at the Galactocentric distance of the Sun, Ω_0, can be estimated for objects near the Solar circle and tangent points, with relaxed assumptions on the adopted value of R_0. For objects with negligible peculiar motion, the angular velocity of Galactic rotation at the Sun is given by

$$\Omega_0 \quad = \quad -a_0\mu_l + v_r\left(\frac{1}{D\tan l} - \frac{1}{R_0\sin l}\right) \tag{5.2}$$

where D is the distance to the source from the Sun, v_r is the LSR velocity, μ_l is the systemic sky-plane proper motion in the direction of Galactic longitude, and $a_0 = 4.74$ km s^{-1} kpc^{-1} (mas yr^{-1})$^{-1}$ is a unit conversion factor.

In order to make use of Equation (1) we first convert our systematic proper motion estimate into the proper motion with respect to the LSR in the Galactic coordinate system. To correct for the motion of the Sun with respect to the LSR we use the following values: ($U_\odot$,$V_\odot$,$W_\odot$) = (+10.3, +15.3, +7.7) km s^{-1} (Kerr & Lynden-Bell 1986, *see also* Ando et al. 2011). The relevant parameters, determined in this paper, for IRAS 20056+3350 are: $D = 4.69^{+0.65}_{-0.51}$ kpc and $\mu_l = -6.39 \pm 0.48$ mas yr^{-1}. We use $v_r = +9.0 \pm 0.25$ km s^{-1} determined from molecular line observations (*see section 4.2.1*). Applying the above parameters to Equation (1), and using $R_0 = 8.05$ kpc, gives

$$\Omega_0 = 29.76 \pm 0.50 \text{ km s}^{-1} \text{ kpc}^{-1}$$

We demonstrate the invariability of this approach on the adopted value of R_0 for Solar circle objects by recalculating Ω_0 for a range of values of $7 \leq R_0 \leq 9$ kpc. This difference produces only a small deviation of $\Delta\Omega_0 = \pm 0.3$ km s^{-1} kpc^{-1}. The value of Ω_0 is consistent with other Solar circle and tangent point sources as discussed in detail in Burns et al. (2014b). All such objects produce a value that is higher than that obtained from the ratio of the Galactic constants recommended by the IAU of $\Omega_0 = \Theta_0/R_0 = 25.9$ km s^{-1} kpc^{-1} (Kerr & Lynden-Bell, 1986).

5.2.4 Conclusions

We measured the trigonometric distance of IRAS 20056+3350 to be $D = 4.69^{+0.65}_{-0.51}$ kpc, which is 2.8 times larger than the near D_{kin} often adopted in the literature. In measuring the annual parallax the astrometric accuracy in the R.A. and Dec. directions were investigated and the former was found to be significantly influenced by the elongation of maser structure, although the latter was affected negligibly. The astrometric errors evaluated in this analysis were well matched by the error floors required to produce a χ^2 value of unity in the parallax fitting procedure.

We determined the systematic proper motion of the source to be ($\mu_\alpha \cos\delta$, μ_δ) = (-2.62 ± 0.33, -5.65 ± 0.52) mas yr^{-1} under the assumption that the H_2O masers used in our observations are associated with a line of sight bipolar outflow. This assumption is

justified by the spatial and kinematic proximity of masers to the blue lobe of the bipolar outflow as revealed from archive maps, velocity spectra and an SED model compiled using infrared photometry data interpreted using the fitting tool of Robitaille et al. (2007).

From the accumulation, re-evaluation and summary of various archive data we find IRAS 20056+3350 to be a young MSFR which is forming a central object of considerable mass ($>16M_{\odot}$). It is at an evolutionary stage resembling a *Class I* YSO and appears to precede the formation of an UCHII region.

IRAS 20056+3350 is at the leading tip of the Local arm, near the Solar circle, and its position in relation to the spiral arms tentatively supports that the Local arm may be a branch of the Perseus arm.

Using our results obtained with VERA, and the special geometry applicable to Solar circle objects, we evaluated the angular velocity of Galactic rotation at the Sun, $\Omega_0 = 29.75 \pm 2.29$ km s^{-1} kpc^{-1}, which is consistent with other Solar circle and tangent point sources estimated using the same procedure. IRAS 20056+3350 included, all such estimates are higher than the value derived from the ratio of the Galactic constants recommended by the IAU of $\Omega_0 = \Theta_0/R_0 = 25.9$ km s^{-1} kpc^{-1}.

6

Summary

In this thesis we have discussed the topics of massive star formation, and the structure and kinematics of the Milky Way Galaxy. These topics are closely tied since massive stars are born only in the spiral arms of the Galaxy, allowing us to trace out the 3D shape of the Galaxy by determining the distribution of massive star forming regions.

These topics are also, in themselves, interesting when taken individually - and chance findings made throughout the years of this work have lead to unexpected changes in direction, opening up new and very fruitful research avenues;
With regards to massive star formation we have seen, in S255IR-SMA1, strong evidence that massive stars can continue to accrete material well into the production of ionizing radiation - once thought to limit star formation to about 8 Mo. In this same source we also see episodic ejections indicated by our discovery of the first micro-bowshock in a massive star. Episodic ejection alludes to an episodic nature to the aforementioned accretion - lending evidence to the theory that massive stars can be formed in a disk-jet-outflow system, with the added ingredient of bloating the star to reduce the effects of radiation pressure.

Our observations with VERA also lead to the discovery of a rotating water maser jet in S235AB-MIR. This long sought proponent of star formation is seen here for the first time in a massive young stellar object, and also for the first time for any star in 3 dimensions. Its significance lies in providing a mechanism of removing angular momentum from the inner regions of protostellar disk systems, allowing material to approach closer to the central object. Rotation also confirms that the jet in S235AB-MIR, a massive star, must be magnetically launched and collimated - hinting at the presence of a disk-jet-outflow system as is seen in low mass star formation.

Thus one of the overriding conclusion is that, at least in these two massive young stellar objects, its seems that their massive stars are being formed in disk-jet-outflow systems, much like those seen in low mass stars. We also find both jets to exhibit evidence of being magneto-centrifugally launched. The two issues that we address; angular momentum dispersal and radiation pressure, are certainly the two biggest issues hindering a consensus about massive star formation theories. What remains to be seen is if our findings are universal or unique/rare cases - thus we require to repeat the kind of studies presented here for a larger sample of maser bearing massive young stellar objects.

The discoveries and scientific progress mentioned above was made possible by the development of an improved data reduction approach, the inverse phase referencing method for VERA, which produces high dynamic range and astrometrically accurate

maser maps. Without this technique both the data of S255IR-SMA1 and S235AB-MIR would have been trashed. Developing these scripts therefore stands as the most important part of this entire work. The scripts are publicly available (*see* Section 3.2.1).

As part of studying how massive stars form we made effort in measuring their trigonometric distances via annual parallax. This in turn opened up the possibility to study the structure of the Milky Way Galaxy and its kinematics. In total we measured the distance and proper motions of 3 high mass star forming regions and one of intermediate mass. We find that two of them reside in the Local Arm of the Galaxy - IRAS20056+3350 at the leading tip of the Arm and IRAS20143+3634 near to the Sun. These two star forming regions reside on the Solar Circle and at the tangent point, respectively, allowing us to estimate the Galactic angular rotation velocity at the radius of the local standard of rest, $\Omega_0 = 27.3 \pm 1.6$ km s^{-1} kpc^{-1}. Comparing this value to others estimated recently we find consistently that modern values are significantly higher than those recommended by the international astronomical union.

The other two massive star forming regions, S255IR-SMA1 and S235AB-MIR, were found to reside in the Perseus Arm in the Galactic anticenter direction - a region of the Galaxy where radial velocities tend to zero, rendering kinematic distance estimations unusable and highlighting the value of VLBI determined parallax distances for mapping the 3D structure of the Milky Way Galaxy, which is shown in Figure 6.1.

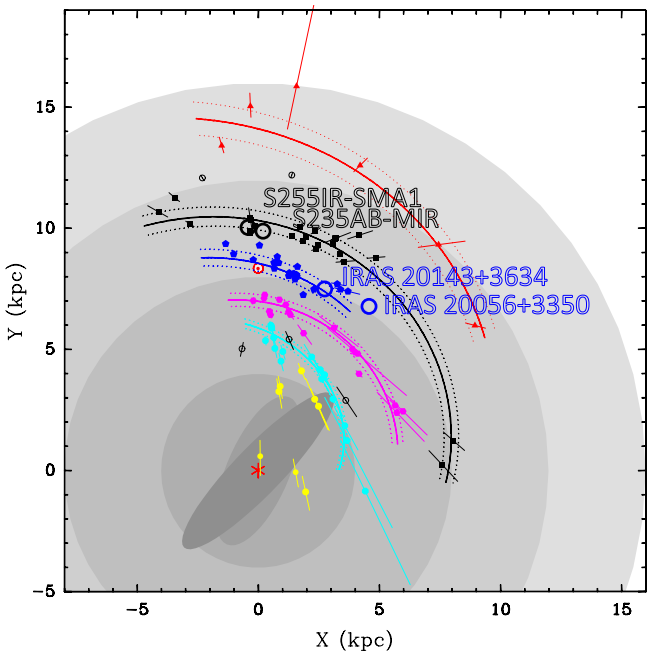

Figure 6.1: Trigonometric distances presented in this thesis; locations of IRAS 20056+3350, IRAS20143+3634, S255IR-SMA1 and S235AB-MIR, in relation to the presently known Galactic spiral structure evaluated using VLBI observations of MSFRs (compiled by Reid et al. 2014, *individual references therein*).

References

Allen, C. W. 1976, in Astrophysical Quantities, 3rd edition (The Athlone Press, University of London)
Ando, K., Nagayama, T., Omodaka, T., et al. 2011, PASJ, 63, 45
Ao, Y., Yang, J., & Sunada, K. 2004, AJ, 128, 1716
Asaki, Y., Sudou, H., Kono, Y., et al. 2007, PASJ, 59, 397
Bacciotti, F., Ray, T. P., Mundt, R., Eislöffel, J., & Solf, J. 2002, ApJ, 576, 222
Bally, J., & Zinnecker, H. 2005, AJ, 129, 2281
Bartkiewicz, A., & van Langevelde, H. J. 2012, in IAU Symposium, Vol. 287, IAU Symposium, ed. R. S. Booth, W. H. T. Vlemmings, & E. M. L. Humphreys, 117–126
Beichman, C. A., Neugebauer, G., Habing, H. J., Clegg, P. E., & Chester, T. J., eds. 1988, Infrared astronomical satellite (IRAS) catalogs and atlases. Volume 1: Explanatory supplement, Vol. 1
Beltrán, M. T., Cesaroni, R., Neri, R., et al. 2004, ApJL, 601, L187
Beuther, H., Schilke, P., Sridharan, T. K., et al. 2002, A&A, 383, 892
Bronfman, L., Nyman, L.-A., & May, J. 1996, A&AS, 115, 81
Burns, R. A., Handa, T., Hirota, T., et al. 2016a, A&A, 586, A34
Burns, R. A., Handa, T., Omodaka, T., Sunada, K., & Nagayama, T. 2016b, MNRAS, submitted
Burns, R. A., Imai, H., Handa, T., et al. 2015, MNRAS, 453, 3163
Burns, R. A., Nagayama, T., Handa, T., et al. 2014a, ApJ, 797, 39
Burns, R. A., Yamaguchi, Y., Handa, T., et al. 2014b, PASJ, 66, 102
Cabrit, S., Raga, A., & Gueth, F. 1997, in IAU Symposium, Vol. 182, Herbig-Haro Flows and the Birth of Stars, ed. B. Reipurth & C. Bertout, 163–180
Caratti o Garatti, A., Stecklum, B., Linz, H., Garcia Lopez, R., & Sanna, A. 2015, A&A, 573, A82
Casoli, F., Combes, F., Dupraz, C., Gerin, M., & Boulanger, F. 1986, A&A, 169, 281
Caswell, J. L., & Phillips, C. J. 2008, MNRAS, 386, 1521
Cerqueira, A. H., Velázquez, P. F., Raga, A. C., Vasconcelos, M. J., & de Colle, F. 2006, A&A, 448, 231
Cesaroni, R., Galli, D., Lodato, G., Walmsley, C. M., & Zhang, Q. 2007, Protostars and Planets V, 197
Chavarría, L. A., Allen, L. E., Hora, J. L., Brunt, C. M., & Fazio, G. G. 2008, ApJ, 682, 445
Chikada, Y., Kawaguchi, N., Inoue, M., et al. 1991, in Frontiers of VLBI, ed. H. Hirabayashi, M. Inoue, & H. Kobayashi, 79
Choi, Y. K., Hachisuka, K., Reid, M. J., et al. 2014, ApJ, 790, 99
Coffey, D., Bacciotti, F., Woitas, J., Ray, T. P., & Eislöffel, J. 2004, ApJ, 604, 758
Corcoran, M., & Ray, T. P. 1998, A&A, 331, 147
Cutri, R. M., et al. 2014, VizieR Online Data Catalog, 2328, 0
Davis, C. J., Varricatt, W. P., Todd, S. P., & Ramsay Howat, S. K. 2004, A&A, 425, 981
De Buizer, J. M. 2006, ApJL, 642, L57
Deguchi, S., & Watson, W. D. 1989, ApJL, 340, L17
Dewangan, L. K., & Anandarao, B. G. 2011, MNRAS, 414, 1526
Dickman, R. L. 1978, ApJS, 37, 407
Felli, M., Massi, F., Navarrini, A., et al. 2004, A&A, 420, 553
Felli, M., Massi, F., Robberto, M., & Cesaroni, R. 2006, A&A, 453, 911
Felli, M., Brand, J., Cesaroni, R., et al. 2007, A&A, 476, 373
Fomalont, E. B., Petrov, L., MacMillan, D. S., Gordon, D., & Ma, C. 2003, AJ, 126, 2562
Furuya, R. S., Kitamura, Y., Wootten, H. A., et al. 2000, ApJL, 542, L135
Garden, R. P., Hayashi, M., Hasegawa, T., Gatley, I., & Kaifu, N. 1991, ApJ, 374, 540

REFERENCES

Goddi, C., Moscadelli, L., Sanna, A., Cesaroni, R., & Minier, V. 2007, A&A, 461, 1027
Goldsmith, P. F., & Langer, W. D. 1999, ApJ, 517, 209
Hachisuka, K., Brunthaler, A., Menten, K. M., et al. 2009, ApJ, 696, 1981
Henkel, C., Haschick, A. D., & Guesten, R. 1986, A&A, 165, 197
Hirota, T., Kim, M. K., Kurono, Y., & Honma, M. 2014, ApJL, 782, L28
Högbom, J. A. 1974, A&AS, 15, 417
Honma, M., Tamura, Y., & Reid, M. J. 2008a, PASJ, 60, 951
Honma, M., Kijima, M., Suda, H., et al. 2008b, PASJ, 60, 935
Honma, M., Nagayama, T., Ando, K., et al. 2012, PASJ, 64, 136
Hosokawa, T., Hirano, S., Kuiper, R., et al. 2015, ArXiv e-prints, arXiv:1510.01407
Hosokawa, T., Yorke, H. W., & Omukai, K. 2010, ApJ, 721, 478
Iguchi, S., Kkurayama, T., Kawaguchi, N., & Kawakami, K. 2005, PASJ, 57, 259
Imai, H., Nakashima, K., Bushimata, T., et al. 2007, PASJ, 59, 1107
Imai, H., Omi, R., Kurayama, T., et al. 2011, PASJ, 63, 1293
Imai, H., Sakai, N., Nakanishi, H., et al. 2012, PASJ, 64, 142
Ishihara, D., Onaka, T., Kataza, H., et al. 2010, A&A, 514, A1
Jenness, T., Scott, P. F., & Padman, R. 1995, MNRAS, 276, 1024
Kawaguchi, N., Sasao, T., & Manabe, S. 2000, in Society of Photo-Optical Instrumentation Engineers (SPIE) Conference Series, Vol. 4015, Radio Telescopes, ed. H. R. Butcher, 544–551
Kerr, F. J., & Lynden-Bell, D. 1986, MNRAS, 221, 1023
Kobayashi, H., Sasao, T., Kawaguchi, N., et al. 2003, in Astronomical Society of the Pacific Conference Series, Vol. 306, New technologies in VLBI, ed. Y. C. Minh, 48P
Konigl, A., & Pudritz, R. E. 2000, Protostars and Planets IV, 759
Kurtz, S., Hofner, P., & Álvarez, C. V. 2004, ApJS, 155, 149
Lee, C.-F., Mundy, L. G., Reipurth, B., Ostriker, E. C., & Stone, J. M. 2000, ApJ, 542, 925
Lucas, P. W., Hoare, M. G., Longmore, A., et al. 2008, MNRAS, 391, 136
Miyamoto, M., & Zhu, Z. 1998, AJ, 115, 1483
Molinari, S., Brand, J., Cesaroni, R., & Palla, F. 1996, A&A, 308, 573
Moscadelli, L., Cesaroni, R., & Rioja, M. J. 2000, A&A, 360, 663
Moscadelli, L., Cesaroni, R., Rioja, M. J., Dodson, R., & Reid, M. J. 2011, A&A, 526, A66
Motogi, K., Sorai, K., Niinuma, K., et al. 2013, MNRAS, 428, 349
Motogi, K., Sorai, K., Honma, M., et al. 2015, PASJ, doi:10.1093/pasj/psu142
Nagayama, T., Nakagawa, A., Imai, H., Omodaka, T., & Sofue, Y. 2008, PASJ, 60, 183
Nagayama, T., Omodaka, T., Nakagawa, A., et al. 2011, PASJ, 63, 23
Nagayama, T., Kobayashi, H., Omodaka, T., et al. 2015, PASJ, 67, 65
Navarete, F., Damineli, A., Barbosa, C. L., & Blum, R. D. 2015, in IAU Symposium, Vol. 307, IAU Symposium, 431–436
Ojha, D. K., Samal, M. R., Pandey, A. K., et al. 2011, ApJ, 738, 156
Oort, J. H. 1927, Bull. Astron. Inst. Netherlands, 3, 275
Palla, F., & Stahler, S. W. 1993, ApJ, 418, 414
Petrov, L. 2012, MNRAS, 419, 1097
Pratap, P., Shute, P. A., Keane, T. C., Battersby, C., & Sterling, S. 2008, AJ, 135, 1718
Reid, M. J., & Brunthaler, A. 2004, ApJ, 616, 872
Reid, M. J., Menten, K. M., Zheng, X. W., et al. 2009, ApJ, 700, 137
Reid, M. J., Menten, K. M., Brunthaler, A., et al. 2014, ApJ, 783, 130
Rengarajan, T. N., & Ho, P. T. P. 1996, ApJ, 465, 363
Robitaille, T. P. 2008, in Astronomical Society of the Pacific Conference Series, Vol. 387, Massive Star Formation: Observations Confront Theory, ed. H. Beuther, H. Linz, & T. Henning, 290
Robitaille, T. P., Whitney, B. A., Indebetouw, R., & Wood, K. 2007, ApJS, 169, 328
Russeil, D. 2003, A&A, 397, 133
Russeil, D., Adami, C., & Georgelin, Y. M. 2007, A&A, 470, 161
Rygl, K. L. J., Brunthaler, A., Reid, M. J., et al. 2010, A&A, 511, A2
Rygl, K. L. J., Brunthaler, A., Sanna, A., et al. 2012, A&A, 539, A79
Saito, H., Saito, M., Sunada, K., & Yonekura, Y. 2007, ApJ, 659, 459
Sakai, N., Honma, M., Nakanishi, H., et al. 2012, PASJ, 64, 108
Sato, M., Reid, M. J., Brunthaler, A., & Menten, K. M. 2010, ApJ, 720, 1055
Shimoikura, T., Kobayashi, H., Omodaka, T., et al. 2005, ApJ, 634, 459
Soker, N. 2005, A&A, 435, 125
Sunada, K., Nakazato, T., Ikeda, N., et al. 2007, PASJ, 59, 1185

Tofani, G., Felli, M., Taylor, G. B., & Hunter, T. R. 1995, A&AS, 112, 299
Torrelles, J. M., Gómez, J. F., Patel, N. A., et al. 2012, in IAU Symposium, Vol. 287, IAU Symposium, ed. R. S. Booth, W. H. T. Vlemmings, & E. M. L. Humphreys, 377–385
Torrelles, J. M., Curiel, S., Estalella, R., et al. 2014, MNRAS, 442, 148
Trinidad, M. A., Curiel, S., Estalella, R., et al. 2013, MNRAS, 430, 1309
Urquhart, J. S., Figura, C. C., Moore, T. J. T., et al. 2014, MNRAS, 437, 1791
Varricatt, W. P., Davis, C. J., Ramsay, S., & Todd, S. P. 2010, MNRAS, 404, 661
Wang, Y., Beuther, H., Bik, A., et al. 2011, A&A, 527, A32
Woitas, J., Bacciotti, F., Ray, T. P., et al. 2005, A&A, 432, 149
Wood, D. O. S., & Churchwell, E. 1989, ApJ, 340, 265
Wu, Y., Wei, Y., Zhao, M., et al. 2004, A&A, 426, 503
Wu, Y., Wu, J., & Wang, J. 2001, A&A, 380, 665
Wu, Y. W., Sato, M., Reid, M. J., et al. 2014, A&A, 566, A17
Xu, Y., Li, J. J., Reid, M. J., et al. 2013, ApJ, 769, 15
Yang, J., Jiang, Z., Wang, M., Ju, B., & Wang, H. 2002, ApJS, 141, 157
Yorke, H. W., & Bodenheimer, P. 2008, in Astronomical Society of the Pacific Conference Series, Vol. 387, Massive Star Formation: Observations Confront Theory, ed. H. Beuther, H. Linz, & T. Henning, 189
Zapata, L. A., Lizano, S., Rodríguez, L. F., et al. 2015, ApJ, 798, 131
Zapata, L. A., Schmid-Burgk, J., Muders, D., et al. 2010, A&A, 510, A2
Zhang, B., Reid, M. J., Menten, K. M., et al. 2013, ApJ, 775, 79
Zhang, Q., Hunter, T. R., Brand, J., et al. 2005, ApJ, 625, 864
Zinchenko, I., Liu, S.-Y., Su, Y.-N., et al. 2015, ApJ, 810, 10
Zinnecker, H., & Yorke, H. W. 2007, ARA&A, 45, 481

Declaration

I herewith declare that I have produced this paper without the prohibited assistance of third parties and without making use of aids other than those specified; notions taken over directly or indirectly from other sources have been identified as such. This paper has not previously been presented in identical or similar form to any other Japanese or foreign examination board.

The thesis work was conducted from 2013 to 2016 under the supervision of Prof. Toshihiro Handa at Kagoshima University.

Kagoshima, Japan